Worcester Polytechnic Institute
Digital WPI

Doctoral Dissertations (All Dissertations, All Years) Electronic Theses and Dissertations

2006-01-09

From nanoscale to macroscale, using the atomic force microscope to quantify the role of few-asperity contacts in adhesion

Erik J. Thoreson
Worcester Polytechnic Institute

Follow this and additional works at: https://digitalcommons.wpi.edu/etd-dissertations

Repository Citation
Thoreson, E. J. (2006). *From nanoscale to macroscale, using the atomic force microscope to quantify the role of few-asperity contacts in adhesion*. Retrieved from https://digitalcommons.wpi.edu/etd-dissertations/13

This dissertation is brought to you for free and open access by Digital WPI. It has been accepted for inclusion in Doctoral Dissertations (All Dissertations, All Years) by an authorized administrator of Digital WPI. For more information, please contact wpi-etd@wpi.edu.

Doctoral Dissertation

From nanoscale to macroscale, using the atomic force microscope to quantify the role of few-asperity contacts in adhesion

by

Erik Jan Thoreson

A Dissertation

Submitted to the Faculty

of the

WORCESTER POLYTECHNIC INSTITUTE

in partial fulfillment of the requirements for the

Degree of Doctor of Philosophy

in

Physics

February 2006

APPROVED:

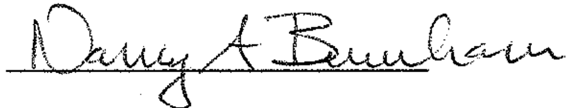

Dr. Nancy A. Burnham, Advisor

Dr. Terri A. Camesano

Dr. Declan G. DePaor

Dr. Rafael Garcia

Dr. Jack Martin

Abstract

The surface roughness of a few asperities and their influence on the work of adhesion is of scientific interest. Macroscale and nanoscale adhesion data have given seemingly inconsistent results. Despite the importance of bridging the gap between the two regimes, little experimental work has been done, presumably due to the difficulty of the experiment needed to determine how small amounts of surface roughness might influence adhesion data lying in between the two scales. To investigate the role of few-asperity contacts in adhesion, the pull-off force was measured between different sized AFM (Atomic-Force Microscope) tips that had different roughnesses and sample surfaces that had well-controlled material properties. The spring constant of the cantilever, the deflection of the cantilever, and the radius of the cantilever tip were measured before each experiment. There were seventeen tips of four different types, with radii from 200 nm to 60 μm. The samples were unpatterned amorphous silicon dioxide die with two types of surface conditions: untreated and treated with a few angstroms of vapor deposited diphenylsiloxane. We observed that the pull-off force was independent of the radius of the AFM tip, which was contrary to all continuum-mechanics model predictions. To explain this behavior, we assumed that the interactions between the AFM tip and sample were additive, material properties were constant, and that the AFM tip, asperities, and sample surfaces were of uniform density. Based on these assumptions, we calculated a simple correction due to the measured Root Mean Square (RMS) surface roughness of the AFM tips. The simple correction for the RMS surface roughness resulted in the expected dependence of the pull-off force on radius, but the magnitudes were higher than expected. Commercial and heat-treated AFM tips had minimal surface roughness and result in magnitudes that were more reliable. The relative uncertainty for the pull-off force was estimated to be 10% and the work of adhesion was estimated to be 15%. In this thesis, we derive how the cantilever and tip parameters contribute to the measured pull-off force, show how the corrected results compare with theory, and demonstrate how the AFM probes were calibrated. Although much work is still needed, the work presented here should expand the understanding of adhesion between the nanoscale and macroscale.

Acknowledgements

Above all, I would like to thank God for my success with this chapter of my life. Lord willing, I will continue to be directed by his path for many years to come.

I would like to thank my wife for her undying love and support. Jamie has been instrumental in helping me achieve this step in my life.

My parents and my wife's parents for their love and support.

I would like to thank Analog Devices, Inc. for their financial support through their research fellowship.

I would like to thank my advisor (Dr. N. A. Burnham) who through her expertise made this possible.

I would like to acknowledge those individuals who have enriched and challenged me with their thoughts and discussions:

Dr. W. Arnold (Fraunhofer-Institute for Nondestructive Testing)
Dr. S. Barjami (Physics)
T. H. Brooks
E. Cagin WPI ECE '03
J. Ferraro (Chemical Engineering)
Dr. R. Garcia (Physics)
Dr. D. G. Gibson (Biology)
Dr. G. Iannacchione (Physics)
Dr. T. H. Keil (Physics)
J. Malone (Physics)
Dr. J. Martin (Analog Devices, Inc.)
G. Matei (Wayne State University)
J. McDonald
Dr. D. Newell (NIST)
Dr. G. D. J. Phillies (Physics)
Dr. J. Pratt (NIST)
Dr. R. J. Pryputniewicz (Mechanical Engineering)
Dr. R. Quimby (Physics)
Dr. A. Roshi (Physics)
Dr. P. A. Tompkins (for the inspiration to go to graduate school)
A. Klempner and the ME crew (Mechanical Engineering)
Footpounders
Noontime Basketball crew

Definitions

Stiction	Two surfaces that permanently adhere to each other.
k	Spring constant of the AFM cantilever.
$\vec{p}$	Momentum (units: Newton*meter(Nm)).
$\vec{F}$	Force (units: Newtons (N)).
V	Potential (units: Joule (J)).
z	Displacement in the x direction (units: Meters (m)).
b	Damping coefficient. (units Kilogram per sec (Kg/s)).
ν	Frequency (Hz).
F_t	Total force on a cantilever (N).
F_s	Restoring force of a spring (N).
F_d	Force applied by a dashpot (a resistive element; N)
m	Mass (units: Kg).
$\ddot{z}$	Acceleration (units: Meters per second squared (m/s^2).
$\dot{z}$	Velocity (units: Meters per second (m/s)).
γ_A	Surface tension of material A (units: milijoules per meter squared (mJ/m^2)).
γ_B	Surface tension of material B (units: milijoules per meter squared (mJ/m^2)).
γ_{AB}	Surface tension between materials A and B (units: milijoules per meter squared (mJ/m^2)).
$\varpi_{adhesion}$	Work of adhesion (units: milijoules per meter squared (mJ/m^2)).

R_{tip}	Radius of the AFM tip (units: Micron (μm)).
R_{sample}	Radius of curvature of the sample (units: Micron (μm)).
Δx	Minimum displacement in x (m).
Δp	Minimum change in momentum (kgm/s).
$\hbar$	Planck's constant divided by 2π (1.055×10^{-34} Joule*seconds (Js)).
θ	Adhesion Parameter (unitless).
E	Young's modulus (Units: Newtons per meter squared (N/m^2))
σ	Theoretical stress (N/m^2)
R	Effective radius of curvature (μm)
$\Delta\gamma$	Work of adhesion (units: milijoules per meter squared (mJ/m^2)).
GPa	Gigapascals (1×10^9 N/m^2).
mJ	Milijoules (1×10^{-3} J).
μm	Microns (1×10^{-6} m).
δ	Deformation (units: nanometers (nm)).
a	Contact radius (units: nanometers (nm)).
P(x)	Pressure distribution (units: N/m^2).
K	Reduced elastic modulus (units: GPa).
F_H	Hertzian-type force (units: N).
F_{JKR}	JKR-type force (units: N).
ϖ	Work of adhesion (units: milijoules per meter squared (mJ/m^2)).

$\varpi_{repose_corrected}$	Work of adhesion corrected for angle of repose (units: milijoules per meter squared (mJ/m^2)).
$F_{repose_corrected}$	Pull-off force corrected for angle of repose (units: milijoules per meter squared (mJ/m^2)).
λ	Tabor parameter (dimensionless).
z_0	Interatomic spacing between atoms or molecules (nm).
μ	Maugis parameter (dimensionless).
F_{DMT}	DMT-type force (units: N).
C	Interaction strength (units: J/m^6).
ρ	Density (units: Kg/m^3).
h	Separation (units: nm).
A	Hamaker constant (units: J).
F_{total}	Total interaction force (units: N).
$F_{corrected}$	Force corrected for surface roughness and angle of repose (units: N).
$F_{repose_corrected}$	Force corrected for angle of repose only (units: N).
M(x)	Moment or magnitude of the torque (units: Nm).
I	Area moment of inertia.
$\lvert\tau\rvert$	Magnitude of the torque.
$\vec{r}$	Position vector.
$r_\perp$	Perpendicular distance to lever arm.
F	Force (N).
L	Length of the cantilever.
ϕ	Angle of repose (units: degree).

commensurate	The roughnesses of two surfaces are shaped so that they interlock perfectly.
incommensurate	The roughnesses of two surfaces are shaped so that they do not interlock perfectly.

Contents

LIST OF FIGURES ... X

1. INTRODUCTION ... 1-1
   - 1.1. ADHESION ... 1-6
   - 1.2. IMPORTANCE OF ADHESION ... 1-8
2. BACKGROUND ... 2-1
   - 2.1. AFM REVIEWED ... 2-2
   - 2.2. THEORETICAL BACKGROUND ... 2-7
     - 2.2.1. ANGLE OF REPOSE REVIEWED ... 2-7
     - 2.2.2. SURFACE ROUGHNESS ... 2-12
       - 2.2.2.1. SURFACE ROUGHNESS LITERATURE REVIEW ... 2-12
       - 2.2.2.2. SURFACE ROUGHNESS THEORY ... 2-16
   - 2.3. CONTACT MECHANICS ... 2-21
     - 2.3.1. HERTZ ... 2-21
     - 2.3.2. JKR ... 2-22
     - 2.3.3. DMT ... 2-23
     - 2.3.4. MAUGIS ... 2-24
     - 2.3.5. TABOR PARAMETER ... 2-25
   - 2.4. EXPERIMENTAL BACKGROUND ... 2-27
     - 2.4.1. MEMS STICTION LITERATURE REVIEW ... 2-27
     - 2.4.2. REVIEW OF MEMS MANUFACTURING AND PACKAGING ... 2-31
     - 2.4.3. REVIEW OF METHODS TO MEASURE STICTION ... 2-32
3. EXPERIMENTAL METHODS AND MATERIALS ... 3-1
   - 3.1. EXPERIMENTAL ... 3-2
   - 3.2. CALIBRATION ... 3-4
     - 3.2.1. SPRING CONSTANT CALIBRATION ... 3-4
     - 3.2.2. THERMAL VERSUS LOADING METHODS: A COMPARISON WITH A NIST CALIBRATED PIEZOLEVER ... 3-12
     - 3.2.3. TIP RADIUS CALIBRATION ... 3-19
     - 3.2.4. SURFACE ROUGHNESS CALIBRATION ... 3-23
   - 3.3. SAMPLE PREPARATION / TYPE OF SAMPLES ... 3-23
4. RESULTS AND DISCUSSION ... 4-1
   - 4.1. RESULTS ... 4-3
     - 4.1.1. ADHESIVE FORCE [NN] VERSUS LOAD [NN] ... 4-3
     - 4.1.2. ADHESIVE FORCE [NN] VERSUS APPROACH/RETRACTION RATE [HZ] RESULTS ... 4-4
       - 4.1.2.1. ADHESIVE FORCE [NN] VERSUS RELATIVE HUMIDITY [%] RESULTS ... 4-5
     - 4.1.3. RMS ROUGHNESS [NM] VERSUS RADIUS [µM] RESULTS ... 4-6
     - 4.1.4. UND ADHESIVE FORCE [NN] VERSUS RADIUS [µM] RESULTS ... 4-7
     - 4.1.5. TND ADHESIVE FORCE [NN] VERSUS RADIUS [µM] RESULTS ... 4-8
   - 4.2. DISCUSSION ... 4-9
     - 4.2.1. SURFACE ROUGHNESS ... 4-11
       - 4.2.1.1. CORRECTED UND ADHESIVE FORCE [NN] VERSUS RADIUS [µM] RESULTS ... 4-14
       - 4.2.1.2. CORRECTED TND ADHESIVE FORCE [NN] VERSUS RADIUS [µM] RESULTS ... 4-15
       - 4.2.1.3. UNCORRECTED AND CORRECTED UND WORK OF ADHESION [MJ/M^2] VERSUS RADIUS [µM] RESULTS ... 4-16
       - 4.2.1.4. UNCORRECTED AND CORRECTED TND WORK OF ADHESION [MJ/M^2] VERSUS RADIUS [µM] RESULTS ... 4-17
     - 4.2.2. THE PHYSICS OF CONTACT ... 4-18
   - 4.3. WHAT MIGHT BE THE IMPACT ON OTHER FIELDS OF SCIENCE? ... 4-23
5. CONCLUSIONS ... 5-1
6. FUTURE WORK ... 6-1

6.1. MEASURING THE ROUGHNESS 6-1
6.2. OPTIMIZED SURFACE ROUGHNESS 6-2
6.3. MATERIAL PROPERTIES 6-2
6.4. AFM PROBE PARAMETERS 6-2
6.5. BIOMATERIALS 6-3
6.6. EXPERIMENTS IN LIQUID 6-3
6.7. HEAT-TREATED AFM TIPS 6-3
6.8. NIST TRACEABLE MEASUREMENTS 6-4
6.9. DEVICE PERFORMANCE 6-4
6.10. LONG TERM-SURFACE STABILITY 6-4
6.11. MATERIAL STANDARDS 6-5
6.12. THE FUTURE OF MEMS AND NEMS 6-5

Appendices

A. IMAGE OPTIMIZATION A-1

B. MEASURING THE AFM LASER WAVELENGTH B-1

C. CALIBRATING THE Z-SCANNER C-1

D. CALIBRATING THE SPRING CONSTANT OF THE CANTILEVER D-1

E. NIST LOADING METHOD E-1

F. CALIBRATING THE RADIUS OF A COMMERCIAL AFM TIP F-1

G. MAKING LARGE AFM TIPS G-1

H. MEASURING THE TIP ROUGHNESS H-1

I. REPORT ON THE WORK OF ADHESION BETWEEN SIX-INCH WAFERS AND AN AFM TIP I-1

J. REPORT ON THE WORKS OF ADHESION BETWEEN NO DIE-ATTACH SAMPLES (UNTREATED AND TREATED) AND AN AFM TIP BEFORE AND AFTER APPLICATION OF UV LIGHT, HEAT, AND A POSITIVELY CHARGED SOURCE (STATICMASTER™ BRUSH) J-1

K. RECOMMENDATIONS FOR THE USE OF AN AFM AS AN IN-FAB STICTION MONITOR K-1

L. BIBLIOGRAPHY L-1

M. RELATED PRESENTATIONS AND PUBLICATIONS M-1

List of Figures

FIGURE 1-1 A) STICTION CAN BE MEASURED USING AN AFM AND MODELED AS A SPHERICAL TIP AND FLAT SURFACE. B) TO A FIRST APPROXIMATION, THE FORCES FOR AN AFM TIP AND SAMPLE COMBINATION ARE MODELED AS A SPRING AND DASHPOT IN PARALLEL. 1-5
FIGURE 2.1-1 AFM SCHEMATIC FOR ACQUIRING CONSTANT-FORCE IMAGES. THE USER MUST SET AND OPTIMIZE THE SCAN RATE, IMAGE SIZE, GAIN, AND SET-POINT... 2-5
FIGURE 2.1-2 SAMPLE FORCE CURVE. THE MINIMUM IN THE RETRACTION CURVE (RELATIVE TO EQUILIBRIUM) IS THE PULL-OFF OR ADHESIVE FORCE, WHICH IS QUANTITY OF INTEREST FOR THIS WORK. TO CONVERT TO AN ACTUAL FORCE CURVE, ONE MUST CONVERT THE FORCE VS. SCANNER POSITION CURVE TO FORCE VS. DISTANCE (OR SEPARATION) CURVE BY INCLUDING THE DEFLECTION OF THE CANTILEVER. 2-6
FIGURE 2.2.1-1. FREE-BODY DIAGRAM OF THE FORCES ACTING ON AN ELEMENT OF THE CANTILEVER AT PULL-OFF. L IS THE LENGTH OF THE CANTILEVER (90 μM), ϕ IS THE ANGLE OF REPOSE OF THE AFM CANTILEVER (10.739 °), AND H_T IS THE HEIGHT OF THE AFM TIP. THE ELEMENT RESIDES AT POSITION X ALONG THE CANTILEVER. THE OFFSET END LOAD IS A DISTANCE H_T SINϕ FROM THE END OF THE CANTILEVER FOR A COMMERCIAL AFM TIP. 2-9
FIGURE 2.2.1-2. FREE-BODY DIAGRAM OF THE FORCES ACTING ON AN ELEMENT OF THE CANTILEVER AT PULL-OFF FOR A BEAD ATTACHED TO A TIPLESS CANTILEVER. L IS THE LENGTH OF THE CANTILEVER (90 μM), ϕ IS THE ANGLE OF REPOSE OF THE AFM CANTILEVER (10.739 °), AND R IS THE RADIUS OF THE BEAD (AFM TIP). THE ELEMENT RESIDES AT POSITION X ALONG THE CANTILEVER. NOW THE OFFSET END LOAD IS A DISTANCE R SINϕ FROM THE END OF THE CANTILEVER FOR A BEAD ATTACHED TO A TIPLESS CANTILEVER (THE FORCE F ACTS THROUGH THE CENTER OF MASS, WHICH IS ASSUMED TO COINCIDE WITH THE GEOMETRIC CENTER OF THE BEAD). 2-10
FIGURE 2.2.2.2-1. SCHEMATIC OF A HEMISPHERICAL AFM TIP AND AN AVERAGE HEMISPHERICAL ASPERITY. THE HEMISPHERICAL ASPERITY IS APPROXIMATED BY THE RMS SURFACE ROUGHNESS AS MEASURED BY THE AFM. THE GRAY SLICES REPRESENT DIFFERENT LAYERS OF ATOMS OR MOLECULES WITHIN DISC-SHAPED SLICES OF THE AFM TIP AND ASPERITY. THE TOTAL INTERACTION FORCE IS A SUM OF THE INTERACTION BETWEEN THE SAMPLE AND ALL THE SLICES WITHIN THE TIP AND ASPERITY. 2-18
FIGURE 2.3.5-1-1. MAUGIS AND TABOR PARAMETER AS A FUNCTION OF THE WORK OF ADHESION. A) R = 300 NM, K = 127 GPA, AND Z_0 = 0.235 NM. BOTH MAUGIS AND TABOR PARAMETER ARE LESS THAN ONE INDICATING THAT DMT IS THE MOST APPROPRIATE DESCRIPTION FOR THE SYSTEM. B) R = 2 μM, K = 127 GPA, AND Z_0 = 0.235 NM.. 2-26
FIGURE 3.2.1-1. SCHEMATIC DIAGRAM FOR ACQUIRING THE A-B SIGNAL AND SAMPLE THERMAL SPECTRUM DATA. THE A-B SIGNAL OF THE CANTILEVER HANGING FREELY IN AIR IS ACQUIRED, A THERMAL SPECTRUM IS BUILT, AND THE RESULT IS FIT TO EQUATION (3.8).. 3-11
FIGURE 3.2.2-1 DIAGRAM OF A TIPLESS AFM CANTILEVER IN CONTACT WITH A PIEZORESISTIVE CANTILEVER CALIBRATED AT NIST. THE UNKNOWN TIPLESS CANTILEVER IS PUSHED AGAINST THE CANTILEVER CALIBRATED AT NIST (PIEZOLEVER) AND THE UNKNOWN SPRING CONSTANT WAS CALCULATED (SEE EQUATION (3.10)). ψ = 0 DEGREES, AS PICTURED IN THE FIGURE... 3-14
FIGURE 3.2.2-2. SAMPLE RESISTANCE DATA FROM AN AGILENT 3301A MULTIMETER. THE TOTAL CHANGE IS ΔR. 3-15
FIGURE 3.2.2-3. SAMPLE DATA ACQUIRED FROM THE OSCILLOSCOPE (THE AFM A-B OR DEFLECTION SIGNAL). THE TOTAL CHANGE IS ΔV_{NIST} (THE DEFLECTION OF THE CANTILEVER WHILE ON THE PIEZORESISTIVE CANTILEVER). 3-16
FIGURE 3.2.2-4. SAMPLE DATA ACQUIRED BY THE AFM. A-B AS A FUNCTION OF SCANNER POSITION. THE INVERSE OF THE SLOPE IS THE CONVERSION FACTOR ($(\delta Z/\Delta V)_{MICA}$; (THE DEFLECTION OF THE CANTILEVER WHILE ON MICA)... 3-17
FIGURE 3.2.3-1. A) SCHEMATIC CROSS-SECTIONAL VIEW OF A SINGLE SPHERE AND A STEP FUNCTION. B) THE EXPECTED CROSS-SECTIONAL DATA, AFTER AVERAGING ALL SCAN LINES OF THE TOPOGRAPHY IMAGE, AND THEIR RELATION TO THE RADIUS AND CENTER OF A CIRCLE. 3-20
FIGURE 3.2.3-2. A) A TYPICAL GRAPH OF A 48 μM SPHERE WITH ALL LINE SCANS AVERAGED FROM A 256 BY 256 PIXEL TOPOGRAPHY IMAGE THAT WAS 10 BY 10 μM^2. B) THE SCALE ON THE RIGHT CORRESPONDS TO THE PERCENT DIFFERENCE BETWEEN THE FIT AND THE DATA. THE BEST CHOICE FOR THE DATA

RANGE WAS ONE IN WHICH THE PERCENT DIFFERENCE WAS LESS THAN OR EQUAL TO ± 5%. THE SCALE ON THE LEFT CORRESPONDS TO THE HEIGHT OF THE AVERAGE CROSS-SECTIONAL DATA AND THE CIRCULAR FITTED RESULTS. NOTE THAT IT IS DIFFICULT TO DISTINGUISH BETWEEN THE FITTED DATA AND THE ACTUAL DATA. 3-22

FIGURE 4.1.1-1. PULL-OFF FORCE AS A FUNCTION OF INCREASING MAXIMUM LOAD ON THE CANTILEVER. THE PULL-OFF FORCE IS CONSTANT AS THE LOAD ON THE CANTILEVER INCREASES. THE SAMPLE WAS THE UNTREATED NO DIE-ATTACH DIE (UND) AND THE AFM TIP WAS AN ATTACHED SiO_2 BEAD, WITH A RADIUS OF APPROXIMATELY 15 μM. 4-3

FIGURE 4.1.2-1. PULL-OFF FORCE AS A FUNCTION OF INCREASING RATE OF FORCE CURVE ACQUISITION. THE PULL-OFF FORCE IS ROUGHLY CONSTANT AS THE RATE OF FORCE CURVE ACQUISITION INCREASES. THE SAMPLE WAS THE UNTREATED NO DIE-ATTACH DIE (UND) AND THE AFM TIP WAS AN ATTACHED SiO_2 BEAD, WITH A RADIUS OF APPROXIMATELY 15 μM. 4-4

FIGURE 4.1.2.1-1. PULL-OFF FORCE AS A FUNCTION OF RELATIVE HUMIDITY (RH). THE PULL-OFF FORCE APPEARS APPROXIMATELY CONSTANT WITHIN THE RANGE OF ABOUT 30-80%, WHICH WAS AS CLOSE AS POSSIBLE TO FAB CONDITIONS. THE SAMPLE SURFACE WAS THE UNTREATED NO DIE-ATTACH (UND) AND THE TIP WAS A COMMERCIAL AFM TIP. 4-5

FIGURE 4.1.3-1. AFM TIP RMS ROUGHNESS AS A FUNCTION OF TIP RADIUS. THE RMS ROUGHNESSES OF THE AFM TIPS WERE MEASURED WITH DIFFERENT TECHNIQUES, EXPLAINED IN THE TEXT (SECTION 3.2.4). 4-6

FIGURE 4.1.4-1. PULL-OFF FORCE AS A FUNCTION OF RADIUS COMPARED TO DMT THEORY FOR THE UNTREATED NO DIE-ATTACH SAMPLE THEORETICALLY WE ESTIMATED, USING EQUATION (2.15), THE WORK OF ADHESION TO BE 100 mJ/m^2, WHICH WAS FOR TREATED SILICON DIOXIDE ($A = 1 \times 10^{-19}$ J). THE PULL-OFF FORCE WAS CORRECTED FOR EFFECTS DUE TO THE ANGLE OF REPOSE. 4-7

FIGURE 4.1.5-1. PULL-OFF FORCE AS A FUNCTION OF RADIUS COMPARED TO DMT THEORY FOR THE TREATED NO DIE-ATTACH SAMPLE THEORETICALLY WE ESTIMATED, USING EQUATION (2.15), THE WORK OF ADHESION TO BE 70 mJ/m^2, WHICH WAS FOR TREATED SILICON DIOXIDE ($A = 0.7 \times 10^{-19}$ J). THE PULL-OFF FORCE WAS CORRECTED FOR EFFECTS DUE TO THE ANGLE OF REPOSE. 4-8

FIGURE 4.2.1.1-1. PULL-OFF FORCE AS A FUNCTION OF RADIUS COMPARED TO DMT THEORY FOR THE UNTREATED NO DIE-ATTACH SAMPLE. THE PULL-OFF FORCE WAS CORRECTED FOR EFFECTS DUE TO THE ANGLE OF REPOSE AND SURFACE ROUGHNESS; THE LATTER CAUSES THE PULL-OFF FORCE TO BECOME ROUGHLY LINEARLY DEPENDENT ON R. 4-14

FIGURE 4.2.1.2-1. PULL-OFF FORCE AS A FUNCTION OF RADIUS COMPARED TO DMT THEORY FOR THE TREATED NO DIE-ATTACH SAMPLE. THE PULL-OFF FORCE WAS CORRECTED FOR EFFECTS DUE TO THE ANGLE OF REPOSE AND SURFACE ROUGHNESS; THE LATER CAUSES THE PULL-OFF FORCE TO BECOME ROUGHLY LINEARLY DEPENDENT ON R. 4-15

FIGURE 4.2.1.3-1. WORK OF ADHESION VERSUS RADIUS FOR THE UNTREATED NO DIE-ATTACH SAMPLE (UND). A)THE DATA WERE CORRECTED FOR ANGLE OF REPOSE AND SURFACE ROUGHNESS. B) THE DATA WERE CORRECTED FOR EFFECTS DUE TO THE ANGLE OF REPOSE ONLY AND THE WORK OF ADHESION DECREASES BY FOUR ORDERS OF MAGNITUDE. $\varpi = 70 \pm 30$ mJ/m^2, FOR COMMERCIAL AND HEAT-TREATED TIPS ONLY. THE EXPECTED WORK OF ADHESION FOR TWO FLAT PLATES OF SILICON WAS $\varpi = 100$ mJ/m^2. 4-16

FIGURE 4.2.1.4-1. WORK OF ADHESION VERSUS RADIUS FOR THE TREATED NO DIE-ATTACH SAMPLE (TND). A)THE DATA WERE CORRECTED FOR ANGLE OF REPOSE AND SURFACE ROUGHNESS. B) THE DATA WERE CORRECTED FOR EFFECTS DUE TO THE ANGLE OF REPOSE ONLY AND THE WORK OF ADHESION DECREASES BY FOUR ORDERS OF MAGNITUDE. $\varpi = 45 \pm 16$ mJ/m^2, FOR COMMERCIAL AND HEAT-TREATED TIPS ONLY. 4-17

FIGURE 4.2.2-1. THE INTERACTION FORCE AS A FUNCTION OF RMS ROUGHNESS. THE VALUE FOR THE NUMBER OF THEORETICAL ASPERITIES WAS VARIED (SEE EQUATION (4.2) AS N=10, 100, AND 1000. R WAS 2 μM, $\varpi = 100$ mJ/m^2, AND H = 0.165 NM. THE MINIMUM IN THE FORCE OF INTERACTION IS SHIFTED UPWARD AND TO THE LEFT AS THE NUMBER OF ASPERITIES INCREASES. 4-21

FIGURE 4.2.2-2. . THE THEORETICAL INTERACTION FORCE AS A FUNCTION OF RMS ROUGHNESS. THE VALUE FOR THE RADIUS OF THE TIP WAS VARIED (SEE EQUATION (4.2)) AS R = 0.02 μM, 0.2 μM, AND 2.0 μM. N=1000, $\varpi = 100$ mJ/m^2, AND H = 0.165 NM. THE MINIMUM IN THE FORCE OF INTERACTION IS SHIFTED UPWARD AND TO THE RIGHT AS THE SIZE OF CONTACT INCREASES. 4-22

List of Tables

TABLE 2.2.2.1-1. TYPICAL VALUES FOR THE DIMENSIONLESS ADHESION PARAMETER. E = 190 GPA FOR SILICON AND $\Delta\gamma = 100$ MJ/M^2. 2-15
TABLE 6.11-1. THE LONG-TERM STABILITY OF THE UND SAMPLE. THE WORK OF ADHESION WAS MEASURED WITH A COMMERCIAL AFM TIP. 6-5

CHAPTER 1

1. Introduction

Richard Feynman is usually credited for starting the field now known as nanotechnology. "There's plenty of room at the bottom," his famous talk, given December 29, 1959 at the annual meeting for the American Physical Society suggested that single atom manipulation was physically possible. Since his talk, miniaturized devices have become important to science and industry, allowing the environment to be measured and monitored in unique ways. A popular example of a futuristic device that would have practical applications is a microscopic autonomous robot, which moves through the bloodstream and can be programmed wirelessly from outside the body to provide diagnosis or treatment. An individual at risk for a myocardial infarction might have a collection of these robots monitoring heart tissue passively, sensing changes to heart rate and rhythm. If a problem is detected, the robots will be activated to provide the necessary repair function, such as tissue repair, distribution of medication, or in extreme circumstances electrical stimulation[1, 2, 3]. To be viable, these devices would need to be very small (total device size < 7 μm) to move freely through the body, and would need small actuators, motors, sensing elements, and propulsion systems. Miniaturized devices that have dimensions in the range of 0.1-100 μm are known as MEMS (MicroElectroMechanical Systems), and in the range of 0.1-100 nm are known as NEMS (NanoElectroMechanical Systems).

The construction of MEMS has paralleled integrated circuit construction[4, 5, 6] and is rapidly becoming practical for everyday use. However, the ability to build MEMS/NEMS

seems to be growing faster than is our knowledge about their behavior[7,8], which is instrumental to their commercial application. MEMS offer advantages over their larger counterparts because they are less expensive to manufacture, dissipate less energy, and allow the measurement of smaller displacements[9]. A common problem to manufacturing smaller devices is that surface area to volume ratios increase, causing surface interactions to dominate the operation of these devices.

One of the most common surface effect problems with MEMS / NEMS devices is something known as stiction[10]. Stiction occurs when two surfaces permanently adhere to each other and can influence yield and reliability of MEMS / NEMS. The surfaces that adhere within the MEMS / NEMS devices are modeled as an AFM cantilever tip-sample interaction. The cantilever sample system can be thought of as a spring and dashpot in parallel (see Figure 1-1)[11].

The classical behavior of a spring, dashpot, and sample surface is governed by Newton's laws. Newton's 1st law states that an object at rest tends to stay at rest unless acted on by an external force. Newton's 2nd law states that the force on an object is proportional to its mass times the rate at which its velocity is changing. The most general form of this law is (for constant mass)

$$\vec{F} = \frac{d\vec{p}}{dt} = m\frac{d\vec{v}}{dt} + \vec{v}\frac{dm}{dt} = m\frac{d\vec{v}}{dt}, \tag{1.1}$$

where

$$\vec{p} = m\vec{v}, \tag{1.2}$$

(momentum = mass times velocity). Newton's 3rd law states that every action has an equal and opposite reaction.

For a force to be derivable from a potential,

$$F = -\frac{dV}{dz}, \tag{1.3}$$

it must be conservative. A force is conservative when

$$\vec{\nabla} \times \vec{F} = 0, \tag{1.4}$$

where the curl of the force must be equal to zero. The potential for a harmonic oscillator (spring) is

$$V = \frac{1}{2} kz^2, \tag{1.5}$$

where k is the spring constant, and z is the displacement from equilibrium. Then its restoring force is

$$F_s = -\frac{dV}{dz} = -kz. \tag{1.6}$$

The force due to the dashpot is

$$F_d = -b\frac{dz}{dt} = -b\dot{z} = -bv. \tag{1.7}$$

The total force on the cantilever tip is a balance between the forces due to the cantilever and the forces due to the sample surface (see Figure 1-1)[11]

$$m\ddot{z}_1 + b_1\dot{z}_1 + k_1 z_1 = k_2\left(z_2 - z_1\right) + b_2\left(\dot{z}_2 - \dot{z}_1\right), \tag{1.8}$$

where k_1 is the spring constant of the cantilever, b_1 is the damping constant of the cantilever, z_1 is the displacement of the cantilever, k_2 is the interaction stiffness, b_2 is the damping constant of the sample, and z_2 is the displacement of the sample. If k_2 is approximately zero (the cantilever is very far from the sample surface),

$$\ddot{z}_1 + \frac{k_1}{m} z_1 = 0. \tag{1.9}$$

Solving Equation (1.9), the displacement [z(t)] of the oscillator as a function of time is found and is equivalent to the equation for a simple harmonic oscillator. In general, the

motion of the cantilever is not that simple while in contact with the sample surface.

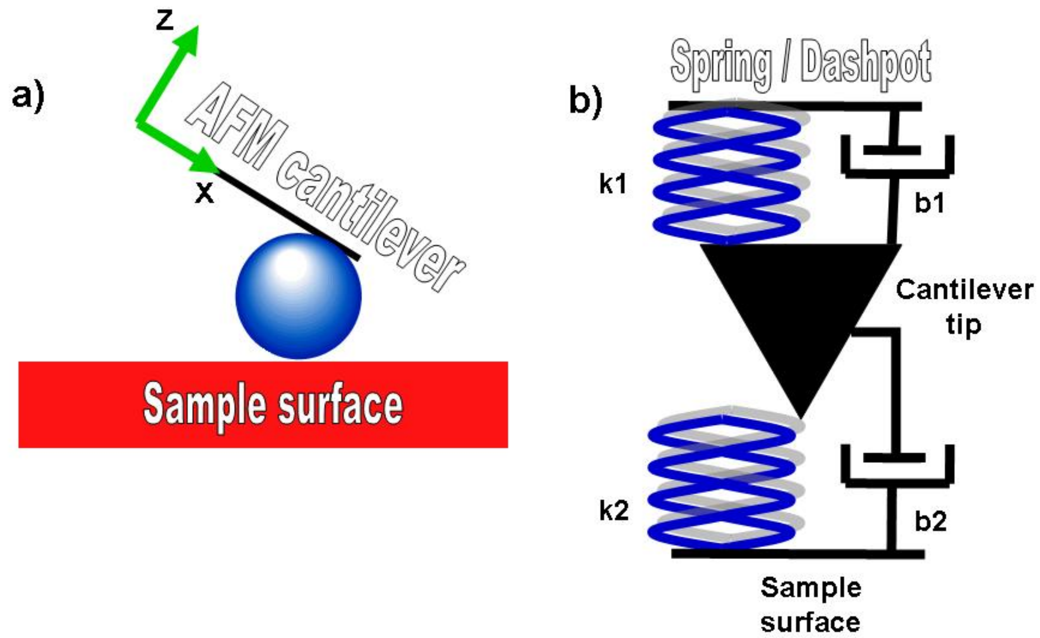

Figure 1-1 a) Stiction can be measured using an AFM and modeled as a spherical tip and flat surface. b) To a first approximation, the forces for an AFM tip and sample combination are modeled as a spring and dashpot in parallel.

Surface forces need to be included, which can be attractive or repulsive.

1.1. Adhesion

The dictionary definition of adhesion is the molecular attraction or repulsion exerted between the surfaces of bodies in contact[12]. Both long-range and short-range interactions can occur when two bodies (or surfaces) are brought into and out of contact with each other. Many names exist for the different types of interactions between the two surfaces, but they all are different manifestations of the four fundamental forces: gravitational, electromagnetic, strong nuclear, and weak nuclear. Each one of these forces has an associated particle with it: graviton (gravity), photon (electromagnetic), gluon (strong), and boson (weak). The gravitational interaction between surfaces in NEMS or MEMS devices is extremely small and zeroed by the AFM (Atomic Force Microscope) laser alignment. The strong and weak forces are intranuclear interactions making them inappropriate to consider for MEMS devices, so the dominant interaction between surfaces is the electromagnetic force (intermolecular forces are electromagnetic[13]).

There are two main types of electromagnetic interactions: chemical[14] and physical[15]. Chemical interaction forces are categorized by three types of bonding (covalent, ionic, and metallic). There are many different types of physical interaction forces.

One type of physical bonding is the van der Waals interaction, which has three components (orientation [Keesom], induction [Debye], and dispersion [London]). Other physical interactions are hydrogen bonding, hydrophobic, specific, steric, depletion, bridge, patch charges, double layer, and coulombic. In general, the strength of the patch charges interaction is much less than the double layer interaction, and the double layer

interaction is much less than van der Waals interaction (for a comprehensive review see references 14 and 15).

The amount of force required to separate two surfaces is the adhesive force or adhesion. If the two surfaces are made of different material constituents, the amount of reversible work done or the free energy change in separating two surfaces per unit area from contact to infinity is the work of adhesion. If the surfaces are the same material consistency, the amount of reversible work is called the work of cohesion[13]. Many contacting surfaces will have defects or adsorbed particles, so typically the work of adhesion is the most appropriate term. Surface energy is the free energy change when the surface area of a sample is increased by a unit area, which is also known as surface tension. The work of adhesion for two materials A and B is related to the surface tension by

$$\varpi_{adhesion} = \gamma_A + \gamma_B - \gamma_{AB}, \tag{1.10}$$

where, γ_A and γ_B are the surface tensions of material A and material B. If the surface tension of A equals B, the work of adhesion is $2\gamma_A$. The work of adhesion is related to the amount of adhesive force ($F_{pull\text{-}off}$) through DMT (Derjaguin, Muller, and Toporov) contact mechanics. DMT assumes that the forces are long-range attractive between the tip and sample, and the tip-sample geometry is Hertzian[11]. DMT mechanics is most appropriate for rigid systems, with low work of adhesion and small radii of curvature. The adhesive force is related to the work of adhesion by

$$\left|F_{pull-off}\right| = 2\pi\left(\frac{R_{tip}R_{sample}}{R_{tip} + R_{sample}}\right)\varpi_{adhesion}, \tag{1.11}$$

where R_{tip} and R_{sample} represent the radius of curvature of the tip and sample. Typically for a flat sample, $R_{tip} << R_{sample}$, so Equation (1.11) reduces to

$$\left|F_{pull-off}\right| = 2\pi R_{tip}\varpi_{adhesion} . \tag{1.12}$$

Eqn. (1.12) indicates that the pull-off or adhesion force should vary linearly with the radius of the AFM tip. Normalizing the adhesion force by the radius of the tip will result in the work of adhesion. The work of adhesion should be constant as the radius or size of the AFM tip increases making it ideal for gauging the adhesion between the tip and sample. Three things that can influence the work of adhesion are the angle of repose, material properties, and surface roughness of the sample or tip. Chapter 2 describes corrections to the adhesive force due to the angle of repose and surface roughness.

1.2. Importance of adhesion

Adhesion is important to understand fundamentally and practically. From a practical standpoint, many MEMS devices have a cantilever that bends or twists during operation. During the manufacture of MEMS, one mode of failure is release stiction where the chemicals coat the surface of the cantilever and through capillary action, the cantilever tip can become adhered to a substrate or surface. In some cases, they are reversibly adhered, while in others, they are irreversibly adhered (stiction)[14]. Another mode of failure is "in-use" stiction, which happens when surfaces get too close. For a spinning gear[16], if the edge of the gear contacts another surface, there can be material transfer between the gear and the surface. This transfer of mass degrades the stability of both materials, which could cause cracks to form in either, and increase adhesion. When the adhesion is high, the gear could break or irreversibly adhere to the contacting surface. Despite the

importance of stiction, few instruments exist that measure the reliability of MEMS devices.

Current MEMS devices are passive devices, lying dormant, waiting to notify the correct control system (sensors) to act when stimulated. The most successful deployment of MEMS are accelerometers, which are used in airbag systems to sense the acceleration of a vehicle. When the acceleration becomes too high, the accelerometers initiate the deployment of the airbag.

Air bags have increased crash survivability and reduced injury to motor vehicle occupants. The National Center for Statistics and Analysis (NCSA) reported in the year 2000 the major cause of deaths, for ages 4-34, was due to motor vehicle crashes. In 2002, it was estimated that more than 133 million vehicles were equipped with air bags, of with 111 million having dual air bags. It was also estimated that 11, 663 lives were saved for the period from 1987 to 2002 because of air bags. Clearly, air bags have an influence on passenger and driver safety.

Other sensors currently found in automobiles that would find economic and efficiency benefits from being miniaturized are fuel injectors, throttle positions, idle speed air bypass valves, exhaust gas recirculation valve positions, air charge temperatures, crankshaft positions, thick film ignitions, manifold absolute pressures, canister purge valves, engine coolant temperatures, heated exhaust gas oxygen, vehicle speed, and exhaust gas recirculation vacuum regulators[17].

The successful continued development of MEMS and NEMS devices requires a fundamental understanding of the interaction between molecules, atoms, and other macroscopic objects[18]. As device size decreases, the surface to volume ratio increases,

and eventually the interaction between surfaces dominates (van der Waals, capillary, etc.). In 1972 Israelachvili and Tabor[19] and in 1978 (eight years prior to the development of the atomic-force microscope (AFM))[20] Coakley and Tabor[21] measured the non-retarded van der Waals forces between macroscopic bodies in air using a Surface Forces Apparatus (SFA). Unlike SFA, the AFM does not measure the separation between surfaces directly. The advantages of the AFM are that any type of conducting or non-conducting surface can be imaged in air, liquid, or vacuum, and high lateral resolution images can be taken, making it ideal for understanding the interaction between surfaces of MEMS and NEMS size.

The difficulty with AFM is that little has been done to calibrate many instruments making it difficult to reliably compare data. We are now able to calibrate the AFM probes before each experiment by measuring the cantilever's spring constant and the radius of the AFM tip, allowing us to perform quantitative studies. The length of the cantilever, angle of repose, and height of the AFM tip also need to be measured[22, 23]. Despite all of this, the AFM is becoming a valuable quantitative tool[24, 25, 26, 27, 28].

In Chapter 2 we review research that has been done in the field of MEMS stiction, surface roughness and its role in adhesion, review contact mechanics, derive the influence of the angle of repose and surface roughness in adhesion, look at the manufacturing and packaging of MEMS devices, and list ways to measure surface forces and stiction. In Chapter 3 we describe how the AFM works, examine how the AFM was calibrated, list the types of samples that were measured, and describe the experimental setup. In chapter 4 we show and discuss the results. Chapter 5 we conclude and in Chapter 6 we suggest future work.

CHAPTER 2

2. Background

Adhesion has been important to mankind since the beginning of their existence. Pitch, the first known form of a man-made (Neandertal) adhesive, was used to adhere the haft to a flint stone knife as early as 80,000 B.C. (middle Paleolithic age)[29].The pitch used was a birch tar heated to somewhere between 340°C and 400°C. The earliest known settlement, Jericho, was founded and developed during the Neolithic age (~ 7000 B.C.) on the Jordan River[30]. As man turned from hunting and gathering to agriculture, a greater need arose for adhesives. In one form or another, adhesives were needed for the development of writing, shelter, buildings, farming tools, clothes, pottery, etc.

The science or natural philosophy of the world developed around 600 B.C.[31] Although Greek science has made a huge impact on modern-day thought, the development of science has been accredited to the first known scientist, Thales of Milteus[31], who was from the coast of Ionia (now Turkey). At about 445 B.C. Empedocles suggested that there were four primary elements (earth, air, fire, and water) and two forces (Love and Strife). However, it was not until the beginning of the seventeenth century that empirical and theoretical descriptions of nature started to appear. Galileo, Hooke, Boyle, and Newton were a few of the 17th century contributors. Newton's second law,

$$\vec{F} = \frac{d\vec{p}}{dt}, \tag{2.1}$$

published in 1687 A.D. was (and still is) one of the most important general quantitative descriptions of the forces acting on a body, which resulted in the birth of classical

mechanics. Ut tension sic vis (extension is proportional to force, $F = -k\delta z$) is one of the best-known contributions by Robert Hooke[32]. The realization that many physical systems near equilibrium can be described as a single or combination of harmonic oscillators was another fundamentally important development. This insight allows one to approximate the quantitative behavior of many types of systems.

The purpose of this chapter is to provide the background information needed to understand the body of work that is described in subsequent chapters. First, AFM techniques are reviewed. Second, the most current work relating to adhesion and the influence of surface roughness is described. Third, pertinent contact mechanics is displayed. Fourth, three components that can influence quantitative measurements for the works of adhesion are discussed: surface roughness, material properties, and effects due to the angle of repose. Fifth, the manufacturing and packaging of MEMS is reviewed, along with ways to measure intermolecular and surface forces and ways to measure stiction.

2.1. AFM reviewed

AFM, MFM (Magnetic-Force Microscopy), NSOM (Near-field Scanning Optical Microscopy), EFM (Electrostatic-Force Microscopy), and STM (Scanning Tunneling Microscopy) are some of the many forms of scanning probe microscopy instruments readily available today. The AFM is a tool for measuring surface topography and interaction forces between a very small probe (AFM tip) and a sample surface (conducting or non-conducting) at very small length scales.

There are three primary modes for our AFM, but only the first mode is used for this work; the other modes are given for reference only. The first is contact mode (see Figure 2.1-1). For contact mode, as the cantilever is scanned over a square of the sample surface, the photodiode records a voltage. The resulting image is a grid of data points; the number of points depends upon the pixel size. Each point is the value for the height at a given x and y location, allowing a three-dimensional profile of the sample surface. The largest topography image that our instrument can image is about 100-micron by 100-micron, with a maximum size of 512 pixels by 512 pixels (see ***A Practical Guide to Scanning Probe Microscopy*** for common imaging artifacts and more information[33]). Intermittent contact mode is a primary AFM mode where the cantilever tip (100-200 nm in diameter) is brought into contact with the sample surface periodically. The AFM cantilever tip is then rastered over the sample in the x and y direction. The cantilever tip (100-200 nm in diameter) is oscillated just above the sample in the non-contact or third primary mode. The cantilever is sensitive to changes in the force gradient, which is registered as a change in the resonant frequency of the vibrating AFM cantilever. The AFM cantilever tip is then rastered over the sample in the x and y direction.

In addition to measuring the surface topography, the AFM can be used to measure very small forces, interaction forces that act between an AFM cantilever tip and sample surface as they are brought into and out of contact, resulting in force curves. Force curves give information on the nature of the forces that are interacting, and measuring the minimum in the retraction curve results in the adhesive (pull-off) force (Figure 2.1-2).

As an initial procedure to data acquisition (Figure 2.1-1), the laser beam is centered on the photodiode (gravitational effects are zeroed) and changes in the voltage are

recorded when the reflected laser beam deflects into the various quadrants of the photodiode (see Appendix A). The A-B signal (the voltage on the top two quadrants minus the voltage on the bottom two quadrants) is the deflection, and the C-D signal (the voltage on the left two quadrants minus the voltage on the right two quadrants) is the angular deflection of the cantilever. The differential amplifier compares the set-point (for constant deflection or normal force in contact mode) to the A-B signal. The output from the differential amplifier is the error signal and the feedback loop controls the movement of the z-scanner. The output from the feedback loop goes to the z-scanner and computer controller. The feedback loop determines what the z-scanner voltage should be and the computer adjusts the voltage for the high voltage amplifier to the correct level.

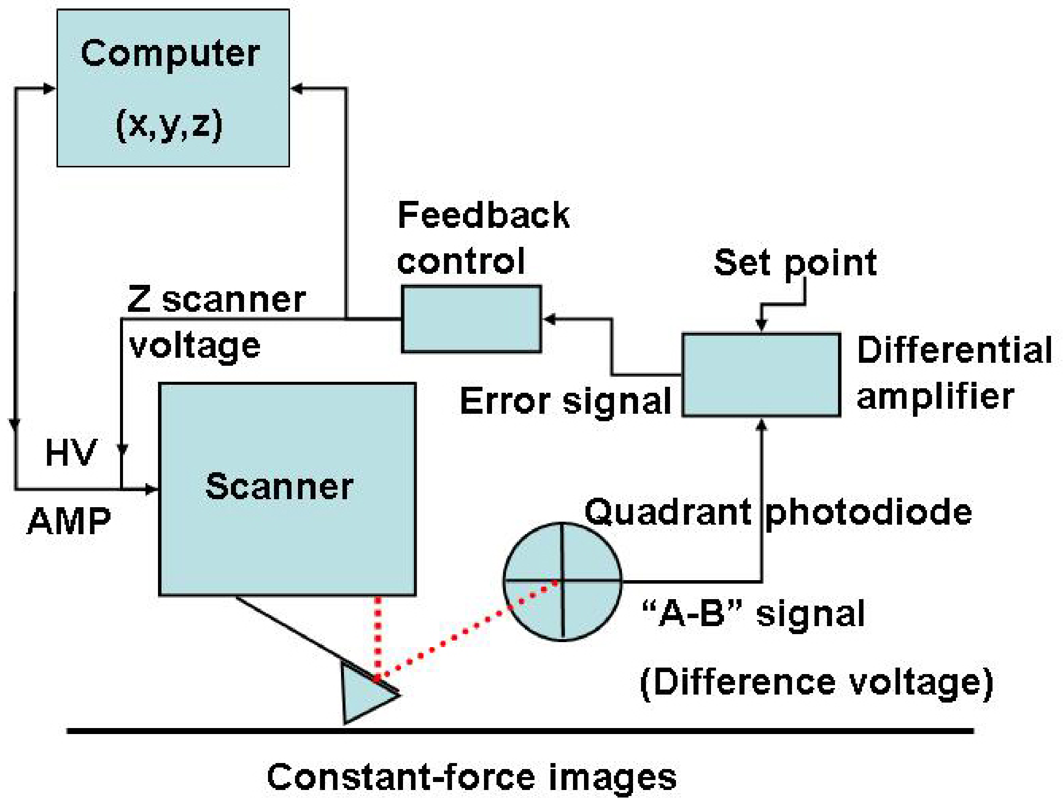

Figure 2.1-1 AFM schematic for acquiring constant-force images. The user must set and optimize the scan rate, image size, gain, and set-point.

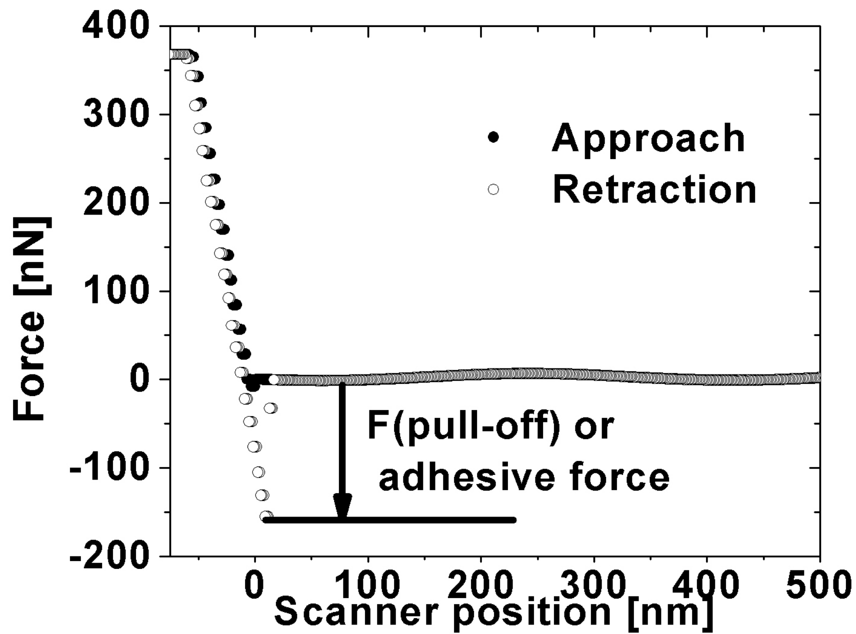

Figure 2.1-2 Sample force curve. The minimum in the retraction curve (relative to equilibrium) is the pull-off or adhesive force, which is quantity of interest for this work. To convert to an actual force curve, one must convert the force vs. scanner position curve to force vs. distance (or separation) curve by including the deflection of the cantilever.

2.2. Theoretical Background

The angle of repose of the cantilever, the surface roughness, and the material properties of the cantilever tip and sample surface might influence the measured adhesion. The following theoretical background sections describe corrections to the adhesive force and work of adhesion that are due to the angle of repose and surface roughness (a method developed by us to handle unexpected data).

2.2.1. Angle of repose reviewed

The cantilever is hung at an angle (within the AFM), known as the angle of repose, relative to the sample surface. The purpose is to keep the base of the cantilever from crashing into the sample surface. The resulting data from the AFM must be corrected to account for the angle of repose, which causes two types of corrections to the measured force data. One type of correction was from the tip-sample interface being offset from the end of the cantilever, and the other was a result of considering the torque on the cantilever during pull-off. There was always a torque on the cantilever; however, there is no correction when the angle of repose is equal to zero. The AFM tip-sample interface can be offset from the end of the cantilever (offset end load), which influences the measured mean-squared amplitude[23]. The offset end load correction does not account for the tip being offset from the center of the cantilever, only the end of the cantilever. For commercial AFM tips, these corrections were negligible, but for large attached beads, the correction could be important.

Reviewing the method described by J. L. Hutter[23], the force on the cantilever was found by calculating the deflection of the cantilever (see Figure 2.2.1-1). The free body diagram is located in Figure 2.2.1-1. To determine the deflection of the cantilever, we equated the curvature of the cantilever at loading to the magnitude of the torque (bending moment) divided by the elastic modulus times the area moment of inertia for the beam (Equation (2.2)).

The radius of curvature for the cantilever is related to the magnitude of the torque on the cantilever by

$$\frac{\frac{d^2y(x)}{dx^2}}{\left[1+\left(\frac{dy(x)}{dx}\right)^2\right]^{3/2}} = \frac{M(x)}{EI} = \frac{|\tau|}{EI}, \tag{2.2}$$

where E is the elastic modulus, I is the area moment of inertia, M(x) is the bending moment, and $|\tau|$ is the magnitude of the torque on the cantilever.

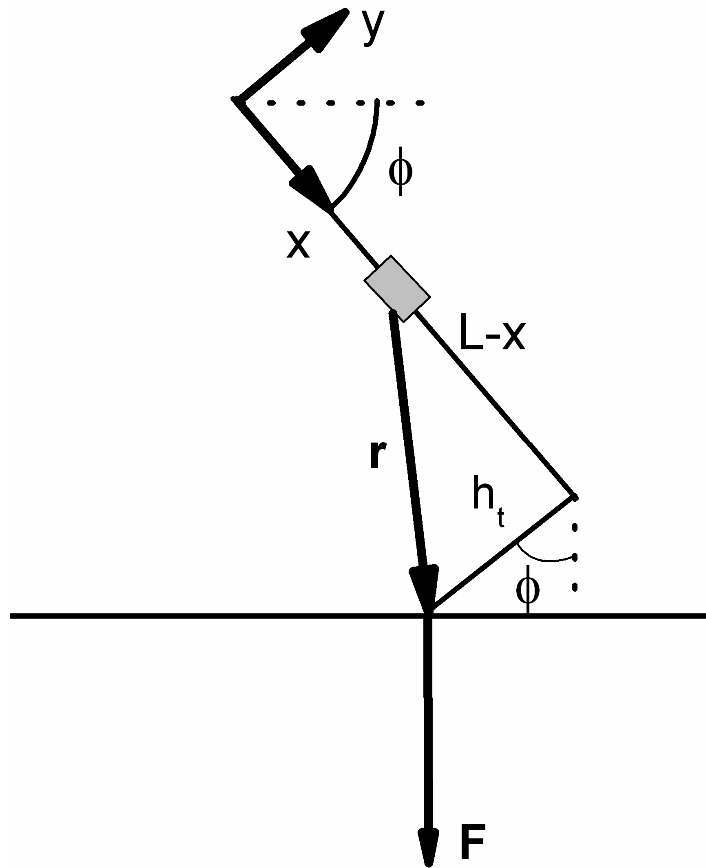

Figure 2.2.1-1. Free-body diagram of the forces acting on an element of the cantilever at pull-off. L is the length of the cantilever (90 μm), ϕ is the angle of repose of the AFM cantilever (10.739 º), and h_t is the height of the AFM tip. The element resides at position x along the cantilever. The offset end load is a distance h_t sinϕ from the end of the cantilever for a commercial AFM tip.

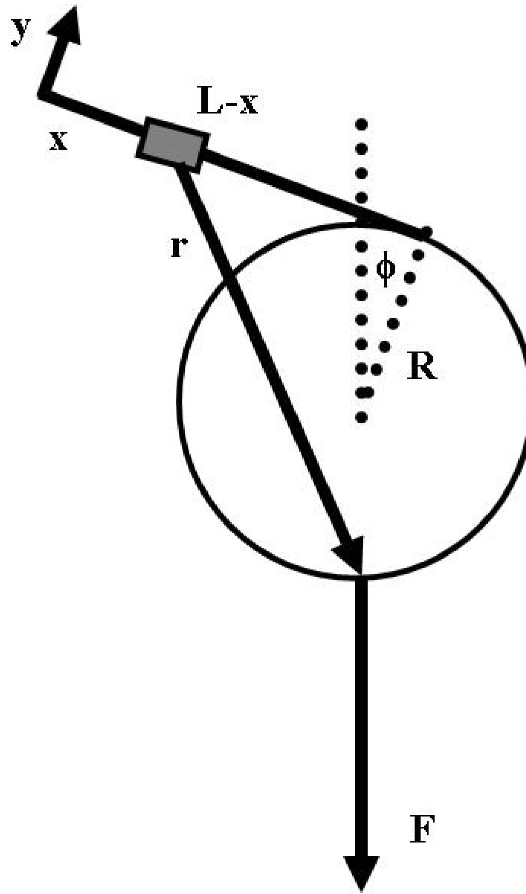

Figure 2.2.1-2. Free-body diagram of the forces acting on an element of the cantilever at pull-off for a bead attached to a tipless cantilever. L is the length of the cantilever (90 μm), ϕ is the angle of repose of the AFM cantilever (10.739 º), and R is the radius of the bead (AFM tip). The element resides at position x along the cantilever. Now the offset end load is a distance R sinϕ from the end of the cantilever for a bead attached to a tipless cantilever (the force F acts through the center of mass, which is assumed to coincide with the geometric center of the bead).

The torque on the cantilever can be found from

$$\tau = \vec{r} \times \vec{F} \rightarrow |\tau| = r_{\perp} F \, , \tag{2.3}$$

where $r_{\perp}$ is the perpendicular distance between the lever arm and the line of action (F). From (Figure 2.2.1-1), the torque has two components,

$$|\tau| = (L - x) F \cos(\phi) - h_t F \sin(\phi) \, . \tag{2.4}$$

F is the attractive force on the cantilever, L is the length of the cantilever, h_t is the height of the tip, and ϕ is the angle of repose of the cantilever. The initial slope of the cantilever at the base is assumed small (dy(x = 0)/dx ~ 0), and inserting Equation (2.4) into Equation (2.2), and simplifying ($h_t = R$),

$$\frac{d^2 y(x)}{dx^2} = \frac{F}{EI}\left[(L - x)\cos(\phi) - R\sin(\phi)\right] . \tag{2.5},$$

Integrating Equation (2.5) (under the condition y(x = 0) = 0), the deflection of the cantilever is

$$y(x) = \frac{F}{EI}\left[\left(\frac{Lx^2}{2} - \frac{x^3}{6}\right)\cos(\phi) - \frac{Rx^2}{2}\sin(\phi)\right] . \tag{2.6}$$

Rearranging Equation (2.6),

$$F_{\text{repose_corrected}} = \frac{F}{\cos(\phi)\left[1 - \frac{3R}{2L}\tan(\phi)\right]} . \tag{2.7}$$

R is the measured radius of the AFM tip, L is the length of the cantilever, $F_{repose_corrected}$ is the corrected force on the cantilever for effects due to the angle of repose only, and ϕ is the measured angle of repose. The correction to the work of adhesion, due to the angle of repose, is

$$\varpi_{corrected_repose} = \frac{F}{2\pi R\left[1-\frac{3R}{2L}\tan\phi\right]\cos\phi}. \quad (2.8)$$

2.2.2. Surface roughness

2.2.2.1. Surface roughness literature review

In 1966 Greenwood and Williamson[34] studied the contact of rough surfaces. They found that whether two surfaces contact each other plastically or elastically was governed by two parameters, the reduced elastic modulus and the hardness. The surface density of the asperities, the standard deviation of their height distribution, and their mean radii were found to influence the contact of surfaces. Their standard deviation was about 1.37 μm, which was much larger than the standard deviation for our experiment. The peak radii for their experiment were 10 – 20 μm, which was much larger than the length scales for the smallest sized tips of our experiment. They suggested that while many surfaces will display a Gaussian type distribution for asperity heights, some will not.

In 1975 Fuller and Tabor[35] studied the influence of sample surface roughness on adhesion. The contacting solids were a rubber sphere (radii were mm) and flat sample of Perspex. Using JKR (Johnson, Kendall, Roberts) contact mechanics, they calculated a dimensionless parameter that was intended to indicate when adhesion would be reduced because of surface roughness.

$$\theta = \frac{E\sigma^{3/2}}{R^{1/2}\Delta\gamma}, \quad (2.9)$$

where E was the elastic modulus of the sample, σ the surface roughness, R the radius of the contacting sphere and Δγ the work of adhesion. Their work suggested that θ greater

than 10 would result in a reduction of adhesion. Typical values for the adhesion parameter are found in Table 2.2.2.1-1, which clearly indicate that even commercial AFM tips can experience a reduction in the adhesion. The downside is that the work of adhesion must be known prior to calculating the adhesion parameter. They describe the adhesion parameter as being a statistical average of the competition between the higher asperities trying to separate the surfaces and the attraction of the smaller asperities to the sample surface.

In 1994 S. K. Das et al.[36] studied the influence of surface roughness on the hydrodynamic detachment of colloidal particles (particle sizes were 10 μm). The theoretical method they developed used linear elasticity theory via Green's function to determine the shape of the deformation of the particle and substrate within the contact area. They found that the hydrodynamic adhesion was not large enough to explain the detachment of colloidal particles and that surface roughness played a significant role in the detachment of colloidal particles. S. K. Das et al. mention that work should focus on characterizing the distribution of asperities and their wavelength. Additionally, they mention the rougher of the two surfaces (particles or substrates) determines the detachment.

In 1996 Suresh and Walz[37] studied the influence of surface roughness between colloidal particles (sizes ranged from 10-25 μm) and a flat plate. The asperities on the colloidal particles were modeled as fixed hemispheres. They use a pairwise summation technique to sum all the interactions between the particle and sample using the van der Waals interaction. They found that the surface roughness lowers the height of the repulsive energy barrier. They also mention that Elimelech et al.[38] report that the

deposition rates of colloidal particles onto surfaces are several orders of magnitude larger than predicted by theory when repulsive double-layer forces exist. The large discrepancy was attributed to surface roughness or the anisotropy of the surface charge density.

θ	σ (nm)	R [μm]
88	0.8	0.2365
128	1.7	1.0800
1124	26.9	55.6365

Table 2.2.2.1-1. Typical values for the dimensionless adhesion parameter. E = 190 GPa for silicon and $\Delta\gamma$ = 100 mJ/m^2.

In 2000 Y. I. Rabinovich[39] studied the adhesion of surfaces with RMS roughnesses ranging from 0.17 – 10.5 nm (particle radii were 50 nm and 10 μm) using the AFM. The particle radii and the spring constant were not measured. They described an adhesion model that utilizes the RMS surface roughness and a longer wavelength variation in the roughness. They found that RMS roughnesses of about two nanometers would decrease the adhesion by a factor of five, which led to their conclusion that the radii of the asperities were important to adhesion.

In 2002 B. N. J. Persson et al. [40] studied the adhesion between two randomly rough surfaces. They developed a theoretical model using fractal analysis that described how the load on one surface is dependent on the contact area. They found that for small loads the area of contact linearly increased with load. They noted that their method only approximated the behavior of the standard model put forth by Greenwood and Williamson[34].

In 2005 [41] B. Luan and M. O. Robbins studied the influence of roughness on adhesion and friction for SPM (Scanning Probe Microscopy) tips. They used molecular simulations to show that the surface roughness causes deviations from continuum contact mechanical theories. The percent difference between experiment and theory could be as large as 100% for small loads on the SPM cantilever. The radii for the SPM tips that they studied ranged from 30 - 300 nm.

2.2.2.2. Surface roughness theory

Traditional continuum contact models overestimate the contact of rough surfaces, since the actual contact area is less than the predicted contact area[34, 35]. If the surfaces were smooth, Equation (2.29) would hold, but in reality the surface of the AFM tip is

rough. Much work exists that addresses single point contacts (asperity) and many point contacts (asperities) with a sample surface. Little work exists that addresses the range in between single point contact and many point contact. Thus, we modified Equation (2.29) to account for surface roughness[69,42].

The sample surfaces are relatively flat (smooth) so we can consider the system as a rough tip in contact with a smooth surface. The model for our AFM tip interacting with a sample surface was a hemispherical AFM tip with hemispherical asperities that were interacting with a smooth sample surface quasi-statically (see Figure 2.2.2.2-1). We calculated the interaction force between an infinite half space, the AFM tip, and the asperities, assuming that the interactions between molecules were additive, the material properties were constant, the cantilever beam was far enough away that its interaction with the infinite half space was negligible, and the tip, asperities, and infinite half space (sample) were all continuous.

The interaction force between a molecule and a sample (or infinite half space) has been shown to be[13]

$$F(z) = \frac{-2\pi C\rho}{(n-2)\,z^{n-2}} = -\frac{A}{2\pi\rho z^4}, \tag{2.10}$$

where C is the interaction strength, ρ is the number density of atoms, z is the separation, A is the Hamaker constant ($A = \rho^2\pi^2 C$), and n = 6 for a van der Waals-type interaction. Since it is not currently practical to measure the number, size, and shape of the asperities within the contact region, we assume that the asperities on the AFM tip can be described by a single average asperity, which is numerically represented by the RMS roughness. To determine the total interaction force between the tip, asperity, and sample, the single molecule interaction must be summed over the volume of the hemispherical asperity and

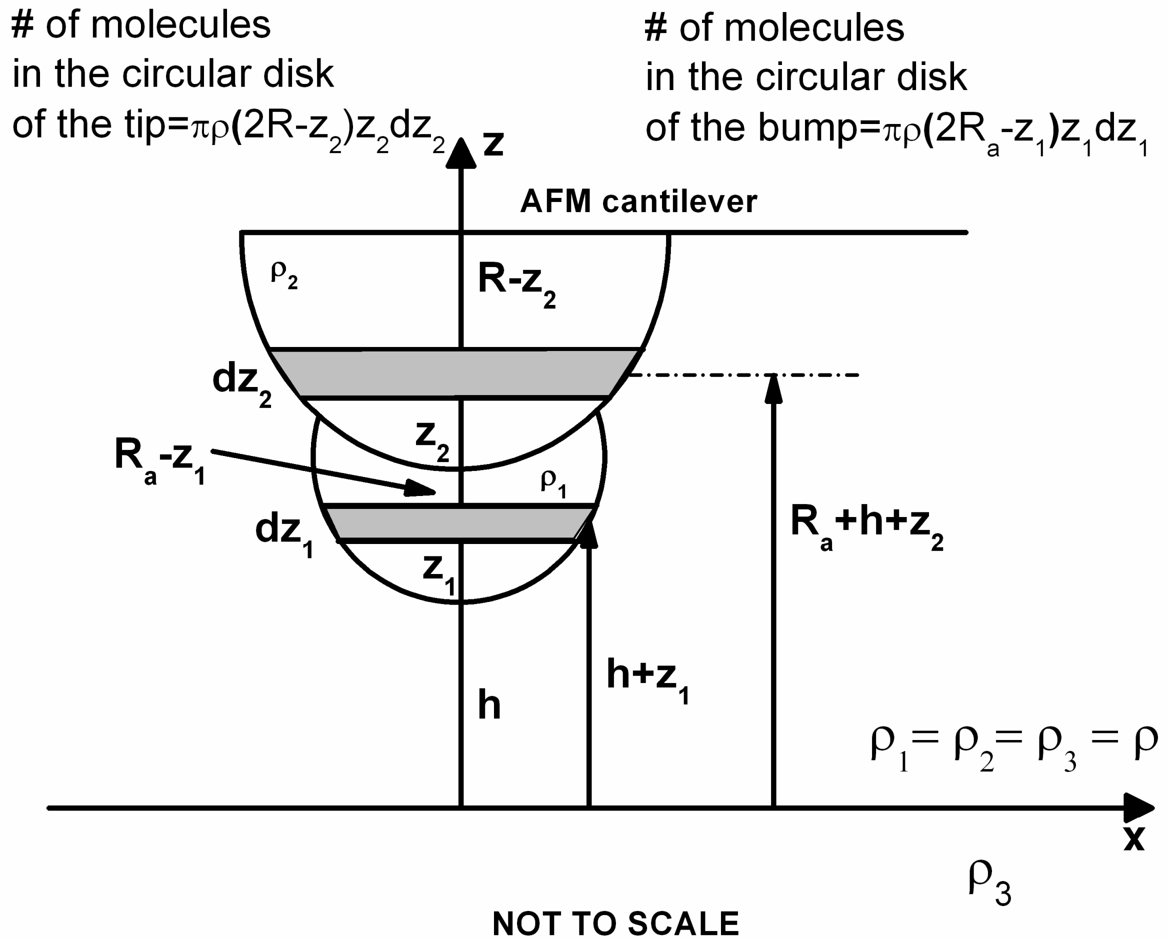

Figure 2.2.2.2-1. Schematic of a hemispherical AFM tip and an average hemispherical asperity. The hemispherical asperity is approximated by the RMS surface roughness as measured by the AFM. The gray slices represent different layers of atoms or molecules within disc-shaped slices of the AFM tip and asperity. The total interaction force is a sum of the interaction between the sample and all the slices within the tip and asperity.

hemispherical tip, requiring two integrals (one for the tip and one for the asperity). In general, the total interaction force is (see Figure 2.2.2.2-1)

$$F_{total}(z) = \frac{-A}{2}\left(\int_0^{R_a} \frac{\left(2R_a - z_1\right) z_1 dz_1}{\left(h+z_1\right)^{n-2}} + \int_0^{R} \frac{\left(2R - z_2\right) z_2 dz_2}{\left(R_a + h + z_2\right)^{n-2}} \right), \tag{2.11}$$

where R_a is the RMS roughness of the tip, h is the tip-sample separation and R is the radius of the AFM tip. When the radius of the tip is much larger than the separation the total force (DMT approximation, R>>h)[45] is

$$F_{total}(z) = \frac{-A}{2}\left(\int_0^{R_a} \frac{\left(2R_a - z_1\right) z_1 dz_1}{\left(h+z_1\right)^{4}} + \int_0^{\infty} \frac{\left(2R\right) z_2 dz_2}{\left(R_a + h + z_2\right)^{4}} \right). \tag{2.12}$$

The asperity contribution is the first term on the right hand side of Equation (2.12); the tip's contribution is the second term. After integrating and simplifying, Equation (2.12) becomes

$$F_{total}(R, R_a) = \frac{-A}{6h}\left[\frac{\left(h+2R_a\right)h^2}{\left(h+R_a\right)^3} - 1 + \frac{R_a}{h} + \frac{Rh}{\left(h+R_a\right)^2} \right]. \tag{2.13}$$

If the roughness goes to zero ($R_a = 0$), then the total interaction force (Equation (2.13)) becomes equal to the interaction force for a sphere-flat in contact

$$F_{total}(R, 0) = \frac{-AR}{6h_c^{\,2}}, \tag{2.14}$$

where h_c is the separation at contact (assumed to be 0.165 nm; the universal cut-off distance[13]).

The work of adhesion is related to the Hamaker constant (A) by[13]

$$\varpi = \frac{A}{12\pi h_c^{\,2}}. \tag{2.15}$$

Substituting for A into Equation (2.13) and simplifying, the total interaction force at contact is

$$\left|F_{total}(R, R_a)\right| = 2\pi R\varpi \left[\frac{(h_c + 2R_a)h_c^3}{R(h_c + R_a)^3} - \frac{h_c}{R} + \frac{R_a}{R} + \frac{h_c^2}{(h_c + R_a)^2} \right]. \tag{2.16}$$

If the RMS roughness goes to zero (R_a goes to zero),

$$\left|F_{total}(R, 0)\right| = 2\pi R\varpi \ . \tag{2.17}$$

DMT contact mechanics is recovered when both the tip and surface are smooth. According to experimental values for the roughnesses and radii, the dominating term in Equation (2.16) is $\frac{R_a}{R}$ (when the roughness is large, $\frac{R_a}{R} \gg$ than other terms), resulting in

$$\left|F_{total}(R, R_a)\right| = 2\pi R\varpi \left[\frac{R_a}{R} \right] = 2\pi R_a \varpi \ , \tag{2.18}$$

which is independent of the radius of the tip.

Equation (2.16) is corrected for the surface roughness only, but the measured pull-off force from the AFM must be corrected for both surface roughness and effects from the angle of repose for the cantilever, which results in

$$F_{corrected}(R, R_a) = \frac{\left|F_{measured}\right|}{\left[\frac{(h_c + 2R_a)h_c^3}{R(h_c + R_a)^3} - \frac{h_c}{R} + \frac{R_a}{R} + \frac{h_c^2}{(h_c + R_a)^2} \right] \left\{ \left[1 - \frac{3R}{2L} \tan\phi \right] \cos\phi \right\}} , \tag{2.19}$$

where L is the length of the cantilever, $F_{total} = F_{measured}$, and $F_{corrected} = 2\pi R\varpi$. The terms that are in the curly brackets are due to the angle for repose of the cantilever. See reference 23 for a discussion on the correction due to the effects of the angle of repose.

2.3. Contact mechanics

Contact mechanics is the study of how two surfaces deform when they touch. Many contact mechanical models can be used to describe the surface forces experienced between a spherical tip on an AFM cantilever and a sample surface. Hertz[43], JKR (Johnson, Kendall, Roberts)[44], DMT (Derjaguin, Muller, and Toporov)[45], and Maugis[46], are some of the different types of contact mechanics. The main differences between the different models are due to the assumptions made about how two surfaces deform when they contact each other. This section is designed to provide information to the reader on the common contact models and is not meant as an exhaustive review. The interested reader should seek other sources for in-depth studies of contact mechanics[47].

2.3.1. Hertz

Hertz theory assumes that the spherical AFM tip is elastic, the sample surface is rigid, and there are neither adhesive nor surface forces. The model is ideal for systems that have high loads, low surface forces, smooth surfaces, and make elastic contact. The deformation of the AFM tip is defined as[15]

$$\delta = \frac{a^2}{R}, \tag{2.20}$$

where a is the contact radius and R is the radius of the sphere. The contact force is

$$F_H = \frac{Ka^3}{R}, \tag{2.21}$$

where F_H is the contact force described by Hertz theory and K is the reduced elastic modulus. The reduced elastic modulus is

$$\frac{1}{K}=\frac{3}{4}\left(\frac{1-\nu_s}{E_s}+\frac{1-\nu_t}{E_t}\right), \tag{2.22}$$

where ν_s and ν_t are Poisson's ratio, E_s and E_t are Young's modulus for the sample and tip, respectively. Under many realistic conditions surface adhesive forces exist, but Hertz theory assumes that there are no adhesive forces, so the model does not describe the AFM tip and surface interaction.

2.3.2. JKR

JKR theory assumes a modified Hertzian contact profile, which includes surface forces. The surface forces are short-ranged and act only inside the contact area, where the tip can deform. The model is ideal for systems that have high adhesive forces, large tip radii, and are compliant.

The maximum adhesive force for a spherical tip contacting a sample surface (or infinite half-space) is [44]

$$\left|F_{JKR}\right|=\frac{3}{2}\pi R\varpi \ , \tag{2.23}$$

where F_{JKR} is the pull-off (adhesive) force measured by an AFM, R is the radius of curvature, and ϖ is the work of adhesion. The contact radius is

$$a=\sqrt[3]{\frac{R}{K}\left[F+3\pi R\varpi+\sqrt{6\pi R\varpi+\left(3\pi R\varpi\right)^2}\right]}, \tag{2.24}$$

where ϖ is the work of adhesion. The contact deformation is

$$\delta=\frac{a^2}{R}-\frac{2}{3}\sqrt{\frac{6\pi\varpi a}{K}}\ . \tag{2.25}$$

The contact force is defined as

$$F_{JKR} = \frac{Ka^3}{R} - \sqrt{6\pi\varpi Ka^3} \ . \tag{2.26}$$

To find the maximum adhesive force, Equation (2.26) is minimized with respect to the contact radius.

$$\frac{\partial F_{JKR}}{\partial a} = \frac{3Ka^2}{R} - \frac{3}{2}\sqrt{6\pi\varpi Ka} = 0 . \tag{2.27}$$

Solving Equation (2.27) for the contact radius and substituting back into Equation (2.26), the maximum adhesive force is found [Equation (2.23)]. The adhesive force at loss of contact can be found by minimizing Equation (2.25) with respect to the contact radius. Solving the subsequent equation for the contact radius and substituting back into Equation (2.26), the adhesive force at loss of contact is

$$\left|F_{JKR_Max}\right| = \frac{5}{6}\pi R\varpi \ . \tag{2.28}$$

The maximum adhesive force and the adhesive force at loss of contact do not coincide. Our system was expected to have a low work of adhesion and to be stiff. We performed tests to determine which mechanics were most appropriate for our system, and they indicate that JKR mechanics was not appropriate.

2.3.3. DMT

DMT theory assumes a Hertzian contact profile with surface forces that are long-ranged. This model is ideal for systems that have low adhesive forces and small tip radii. The contact deformation is the same as Hertz (see Eqn. (2.20)). The maximum adhesive force for a spherical tip contacting a sample surface (or infinite half-space) is[45,]

$$\left|F_{DMT_pulloff}\right| = 2\pi R\varpi \ , \tag{2.29}$$

where $F_{DMT_pulloff}$ is the pull-off (adhesive) force measured by an AFM, R is the radius of curvature, and ϖ is the work of adhesion.

The contact force is defined as

$$F_{DMT} = \frac{Ka^3}{R} - 2\pi R\varpi \quad (2.30)$$

The maximum adhesive force occurs at zero contact radius, which is the same as the adhesive force at loss of contact. For DMT, the maximum adhesive force and the adhesive force at loss of contact do coincide.

Our system was expected to have low work of adhesion and to be stiff. We performed tests to determine which mechanics was most appropriate for our system, and they indicate that DMT mechanics seems to be appropriate (see Figure 2.3.5-1).

2.3.4. Maugis

Maugis theory is the most complete theory in that it applies to all systems[46]. For the limiting case of compliant materials with large radii and high adhesive forces, Maugis mechanics is identical to JKR mechanics [Equation (2.23)] and in the opposite limit (small radii of curvature and low surface adhesive forces) Maugis mechanics is identical to DMT mechanics. The advantage of Maugis mechanics is that little needs to be assumed about the nature of the contact, but the disadvantage is that complicated numerical analyses are required to determine the forces of contact. Maugis defines a dimensionless parameter that can be used to determine which regime (DMT or JKR) is most appropriate[48].

$$\lambda = \frac{2.06}{z_0}\left(\frac{R\varpi}{\pi K^2}\right)^{1/3} \quad (2.31)$$

where z_0 is the interatomic spacing of the material (0.235 nm for silicon).

2.3.5. Tabor parameter

Tabor also introduced the elasticity parameter (μ), a dimensionless parameter to describe the most appropriate regime for a system. The parameter is the ratio between the elastic displacement and the range of interaction[49, 50].

$$\mu = \left(\frac{R\varpi^2}{K^2 z_0^3} \right)^{1/3} \tag{2.32}$$

Both μ (Tabor) and λ (Maugis) are effective at estimating whether DMT ($\mu, \lambda < 1$) or JKR ($\mu, \lambda > 1$) mechanics apply. The main disadvantage is that the work of adhesion must be known prior to the experiment in order to determine which regime is most appropriate (JKR or DMT).

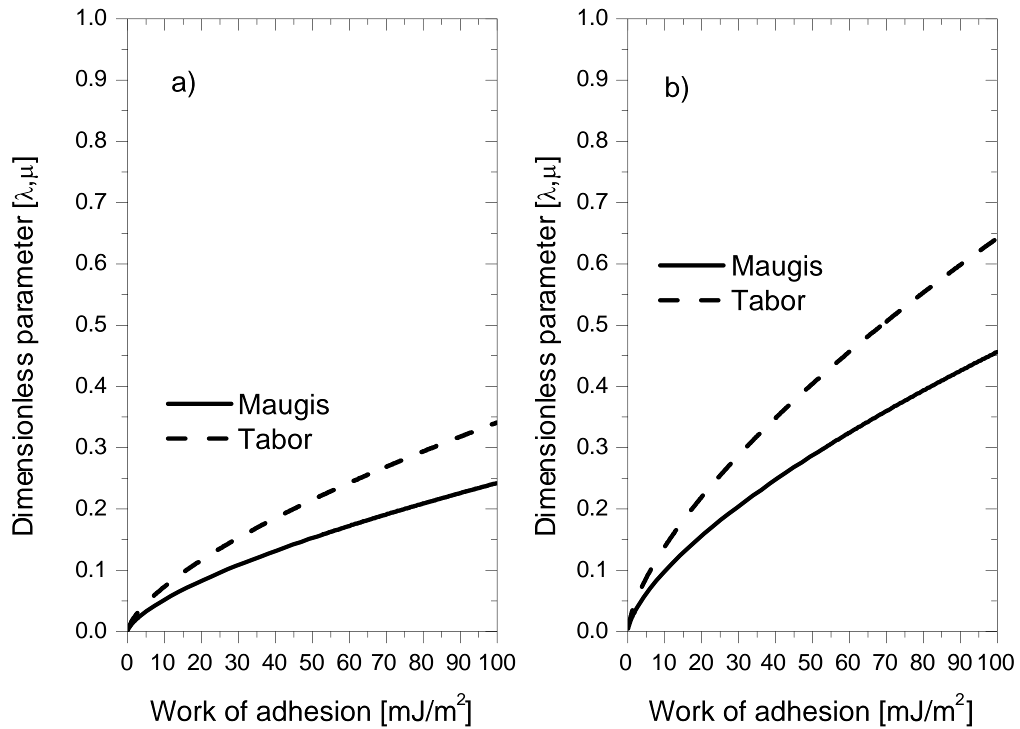

Figure 2.3.5-1-1. Maugis and Tabor parameter as a function of the work of adhesion. a) R = 300 nm, K = 127 GPa, and z_0 = 0.235 nm. Both Maugis and Tabor parameter are less than one indicating that DMT is the most appropriate description for the system. b) R = 2 μm, K = 127 GPa, and z_0 = 0.235 nm.

2.4. Experimental background

2.4.1. MEMS stiction literature review

Much literature exists for the review of adhesion (stiction or surface forces)[14, 15, 18, 51, 52, 53, 54, 55, 56, 57] and for techniques to measure adhesion[13, 58, 59, 60, 61]. A brief overview of the most current work related to stiction will be given here.

In 1993 Burnham et al.[51] indicated that it was important to know both the magnitude of the adhesive force and the shape of the force curve to obtain information about the type of operative surface forces that act between the tip and sample. They described a patch charges model, which initially had a better fit than the van der Waals interaction. The reason van der Waals did not fit as well was attributed to adsorbed particles on the surface.

In 1996 Tas, et al.[62] reviewed four major components to adhesion-capillary forces, hydrogen bonding, electrostatic forces, and van der Waals forces. When reviewing van der Waals forces for surfaces in contact, they suggested that a cut-off distance should be used which is slightly smaller than the interatomic spacing (0.165 nm, a universal cut-off distance). They also suggested that hydrophobic surfaces might be more sensitive to surface roughness because smoothing caused by condensed water is absent.

In 1999 M. P. de Boer et al.[63] referred to autoadhesion (or stiction) as spontaneous sticking between MEMS structures. They stated it was a limiting factor to the optimal yield of silicon-based surface micromachined MEMS. The method they developed to measure stiction required observing the shape of a cantilever adhering to a surface. When a cantilever beam adhered to the surface, it formed either an arc-like or an s-like shape.

The distance over which the beam is not adhered is referred to as the crack length (measuring the crack length requires an interferometer). The thickness of the cantilever must also be measured, which can be difficult.

In 2002 W. Merlijn van Spengen[8] developed a quantitative model where they calculated the interaction energy between two surfaces accounting for both capillary and van der Waals interactions. Next, they modified their calculation to account for rough surfaces. It is important to remember that both the tip and sample roughness can contribute to the measured roughness, since imaging with an AFM is a nonlinear process (dilation between the sample surface and inverted surface of the tip[64]). They also stated that stiction is the limiting factor in the reliable operation of MEMS devices, stiction phenomenon is not predictable quantitatively, and atmospheric pressure is the main cause for capillary stiction. One can measure the dew point, which should indicate when capillary forces due to condensation might be expected. They stated that one must account for both capillary and van der Waals interactions to obtain the true surface interaction. They knew of very little literature that addressed the humidity and temperature dependence of the measured capillary force.

In 2003 B. Bhushan[14] reviewed the mechanisms for adhesion (stiction), various measurement techniques, and the methods used to reduce stiction in magnetic storage devices and MEMS / NEMS. Bhushan stated that roughness could cause asperities to contact at discrete points and summing the area of all asperities that make contact results in the true area of contact, which is smaller than the apparent area. The word stiction was coined at IBM around 1980 when they noticed that a head slider would adhere to the disk surface while resting at a high humidity. A high lateral force was applied to initiate

sliding to overcome the high static friction. Stiction for MEMS / NEMS has a broader definition in that it refers to the high adhesion between two surfaces, which is usually an irreversible process. Covalent bonds, metallic bonds, hydrogen bonding, van der Waals bonding, and the theory of free surface energy are reviewed. Lastly, instruments used to measure intermolecular surface forces, such as AFM (Atomic-Force Microscope), SFA (Surface Forces Apparatus), CBA (Cantilevered Beam Array), and Microtriboapparatus, are described.

In 2003 A.D. Romig, Jr[18] reviewed the material issues, fabrication, and commercialization of MEMS. Romig suggested that greater understanding of the physics related to performance and reliability for MEMS was needed.

In 2004 Sung-Chang Lee and Polycarpou[65] used a quasi-dynamic continuum mechanics model to calculate the intermolecular adhesion forces of low flying (less than 10 nm) heads for magnetic storage disks. They found that when the flying height was less than or equal to five nanometers the adhesion forces were significantly higher; when the flying height was greater or equal to five nanometers the adhesion was significantly lower, and smooth surfaces displayed higher adhesion than rough surfaces.

In 2004 Maboudian and Carraro[66] reviewed challenges with the tribology of MEMS devices. They suggested that experimental evidence did not correlate with predictions from single-asperity contact theories. To measure stiction they suggested that SFA and AFM can be used. SFA requires two flat surfaces, but AFM can measure flat or rough surfaces. Neither SFA nor AFM have contact sizes representative of the contact size found for MEMS devices (heat-treated AFM tips of the right size can be made[67]). The most common technique was listed as CBA (Cantilevered Beam Array), but the

technique requires the fabrication of many cantilevers of different lengths. They also measured a large range of values for the work of adhesion (from 1 - 100 mJ/m^2). They reviewed some of the current adhesion theories and two important points were 1) most adhesion theories use Gaussian height distributions (which might not be valid in the limit of single to a few asperity contacts), and 2) fractal analysis was used to describe the multi-scale behavior of adhesion, while they were not aware of any systematic experimental tests of the predictions made by the fractal model.

In 2004 Drelich et al.[57] determined the solid surface tension from particle-substrate pull-off forces measured with the AFM. Many engineered surfaces cannot be melted, dissolved, or fractured, so the interfacial surface energy cannot be measured by conventional means. Either measuring contact angles or measuring the interfacial surface energy of solids, using an AFM, would solve the problem. They suggested that AFM measurements have not been widely accepted because of their irreproducible nature. Surface roughnesses, material properties, and variations in the load were all reasons listed for the irreproducible nature. They suggested that there must be strict control over all the interacting surfaces. Important points raised in their paper were 1) spring constants for cantilevers can only be measured for small stiffnesses (we have shown that stiffnesses as high as 103 N/m can be measured)[26], 2) much literature lacks the complete characterization of probes and substrates, [SEM (Scanning Electron Microscopy), TEM (Transmission Electron Microscopy), XPS (X-ray Photoelectron Spectroscopy), SIMS (Secondary Ion Mass Spectrometry), and SFA should be performed], 3) selection of a particular contact model was not justified in the literature, 4) larger sized probes can be

imaged with another smaller size probe, 5) plastic deformation can occur and 6) research must be conducted under strict experimental conditions.

2.4.2. Review of MEMS manufacturing and packaging

Although MEMS devices are readily produced, the process is very complex and requires a well-controlled environment. There are more than 500 steps involved in the manufacturing and packaging of MEMS devices and each step must be precisely controlled. RIE (Reactive Ion Etching), Lithographie Glavanoformung Abformung (LIGA), bulk micromachining, micromachining, and photolithography are many different types of processes used during the different steps. Photolithography, the most common process, begins by producing a wafer that is electrically neutral. The resulting MEMS devices are built by depositing layers of structural, electrical, and sacrificial oxides using the different process techniques.

In general, the process of creating a MEMS device begins by depositing a mask on the wafer. The mask is a two-dimensional outline of the MEMS device and those areas that are not covered by the mask are eroded during the etch process (three types of etching are chemical, dry, and photosensitive). To create a MEMS device, these steps (depositing a mask and then etching) are repeated to create the three-dimensional electrical and mechanical structure, which results a wafer containing many MEMS devices. The keys to the success for the commercial viability of MEMS are the ability of the manufacturer to scale its processes, repeat its processes, and produce a yield that is cost effective. Defects can occur even when there are tight controls on processing. A few

examples that can cause defects are changes in the supplier of raw materials, chemical contamination, wafer cleaning processes, and changes in packaging [18].

The packaging process is the most expensive step in manufacturing MEMS devices for commercial use. Device performance is not known until after packaging, which drives the cost of producing commercial MEMS devices. If stiction could be correlated to device performance, the cost of packaging might be reduced. To create the final MEMS device, the wafer is diced into individual sensors. Those sensors are glued (die-attached) into a ceramic box. The devices are then wire bonded to the outside world and the ceramic box is hermetically sealed with a lid. Contamination that can affect device operability can occur at many points during the process, such as when the wafer is diced into a sensor, (the MEMS device can be contaminated from particulates created during dicing), the sensor is glued into the box (the glue can contaminate the surface of the MEMS device), the sensor is wire bonded (the surface of the MEMS device can be contaminated), and the sensor is sealed within the ceramic package. Since contamination is important to the operation of MEMS devices, a way to monitor contamination during the manufacturing process would be useful. Measuring the surface forces or adhesion during manufacture would provide insight into how contaminates influence the operation of MEMS devices.

2.4.3. Review of methods to measure stiction

The following is a quick overview of methods employed to measure stiction.

The Cantilever Beam Array (CBA)[53] technique is an array of cantilever beams that have different lengths all on a single wafer. When the cantilevers are brought into

contact with the surface, the applied force is removed and the cantilevers begin to peel back. Whether a beam sticks or not depends on its length. By measuring the length of the first beam that sticks, one can determine the detachment length and from the detachment length, one can calculate the adhesion. The method depends on measuring the dimensions and detachment length accurately.

The doubly clamped cantilever beam array[53] method is similar to CBA, except the cantilever is clamped at both ends, and the capillary force of water is used to pull down the beam. After beams dry, the detachment lengths of the beams that adhered are measured.

Interferometry[16] measures the deformation of moving parts on MEMS in real-time using Optoelectronic Laser Interferometric Microscopy (OELIM). OELIM measures the deformation of an object as a function of time. The accelerations are then determined via Newton's second law and the forces are calculated. The advantage of this method is that it can non-invasively look at the deformation of a MEMS device that is approximately 200 μm by 200 μm in a single shot. The disadvantage is that forces are not directly measured, but indirectly calculated using a numerical approximation (i.e. Finite Element Method).

Pull-off force measurements with AFM uses a cantilever with a probe tip to measure the force as a function of distance between the tip and a sample (force curves). From Eqn. (1.12), the pull-off force is proportional to the radius of the tip times the work of adhesion. At a minimum, one must measure the spring constant of the cantilever and the radius of the tip in order to obtain quantitative data. Many researchers accept the manufacturer's values for the tip radius and spring constant, use the same tip throughout

an experiment, or normalize data relative to some standard. While this provides good qualitative insight, it does not lead to quantitative analysis. The AFM must be calibrated to obtain accurate and precise values for works of adhesion or pull-off forces.

CHAPTER 3

3. Experimental methods and materials

In chapter two background and historical information was described relating to the adhesion. This section describes the purpose and the experimental procedures we performed for our study.

Calibration, adhesion between two surfaces, and the development of an in-fab stiction monitor are the three key areas of our study. Calibration is important because it provides researchers a standard of measurement that can be used to reliably compare data. The goal of complete characterization is achieved when material properties and instrument parameters have been calibrated. Very often, as noted by Drelich et. al., little has been done to characterize the material properties of the two surfaces that make contact. This can be difficult because the techniques used to characterize the material properties could change the experimental observations. Adhesion studies for single and multiple asperity contacts are also important to understand. Despite this, there is little work that addresses how adhesion behaves in between single and multiple asperity contacts, presumably due to the difficulty of the experiment needed. Much work has been done to reduce adhesion (or stiction) between surfaces, but few have been able to measure adhesion in near real-time of the wafer during manufacturing. The AFM, a common tool found within a wafer fabrication facility, is ideally suited to provide near real-time analysis of adhesion.

The first purpose of this thesis was to apply calibration techniques to reliably compare our adhesion measurements, and to compare the theoretical and experimental adhesion values. The second purpose of this thesis was to study how adhesion changes with the size of contact (or radius of the AFM tip) and to compare the experimental

measurements to the theoretical predictions. The third purpose of this thesis was to provide and describe our method for using the AFM as an in-fab stiction monitor to measure adhesion on the manufacturing line (Appendix K). The purpose for this chapter is to describe our experimental methodology and calibration techniques.

3.1. Experimental

The spring constant of the cantilever, the radius of the tip, and the surface roughness of the samples were measured before force curve aquisition[24, 26, 27]. Two different methods were used to measure the radii of the attached tips, a delta function (TGT01) grating and a step function, which are described elsewhere (both methods are a special case of the Blind Reconstruction method)[68].

For measuring the pull-off force, a new LCC package was opened (first UND and then TND) and a two-micron by two-micron image (with 256 pixels of resolution in each direction) was acquired before force curve acquisition. After stopping the scanner, force curves were obtained at sixteen different locations and each location was an average of sixteen curves. The pull-off forces (minimum in the retraction curve) were found at each of the sixteen locations. The average cantilever deflection and the standard deviation of the cantilever deflection were found for the sixteen data points. Those data points that were more than two standard deviations away from the average were rejected. No more than three data points were rejected in each data set. The load on the cantilever was not kept constant, but the pull-off force was independent of the load on the cantilever (see Figure 4.1.1-1)[69].

All measurements were made at a relative humidity of 31 ± 10% and a temperature of 22.2 ± 0.4 °C. The average sample roughness for the 17 data points was 0.4 ± 0.5 nm. The relative uncertainty for the pull-off force was estimated to be 10% and the precision was 5%. The relative uncertainty for the work of adhesion was estimated to be 15%.

Since the introduction of the AFM in 1986 by Binning et al.[20] many fields of experimental science have benefited from its use. The AFM is extremely useful in obtaining qualitative force data and visualizing the topography of surfaces over very small ranges. However, quantitative analysis of AFM data has been lacking. The measurement of the cantilever probe parameters (angle of repose, radius of the tip, length of the cantilever, and spring constant of the cantilever) can be difficult to measure before each experiment, which could explain the lack in quantitative data. The next section describes how our instrument and AFM probes were calibrated. The final section of this chapter describes the sample preparation.

3.2. Calibration

Qualitative analyses have been useful to increasing scientific knowledge, but little has been done to obtain quantitative AFM data. Caution must be maintained when analyzing reported quantitative data acquired with the AFM, in order to produce quantitative data, the AFM cantilever probes must be calibrated. For force measurements, this requires measuring the spring constant of the cantilever, z-scanner displacement, length of the tip, height of the tip (or radius of the tip), angle of repose, surface roughness, and material properties. Many techniques exist that can determine the constitution of the materials for the tip and sample, but many modify the surface chemistry or require a significant amount of time to complete, making the complete characterization of the surfaces before and after an experiment impractical. Ideally, all measurements should be traceable to a primary standard. Progress is being made towards calibration standards, but currently, no primary standards exist that allows the AFM to be calibrated efficiently before each experiment. The purpose of this section is to convey how our AFM instrument was calibrated.

3.2.1. Spring Constant Calibration

Manufacturer's tolerances for force calibration cantilevers are often very broad, varying by a factor of two or more, making it necessary to measure the cantilever spring constant in-situ. The three different classes of experimental methods developed to measure the spring constant of an AFM cantilever are geometric, loading, and thermal. For a comparison between the different methods, see Burnham et al.'s work[28]. The

geometric method is based upon knowledge of the cantilever's dimensions and can be measured with an SEM (Scanning Electron Microscope) or calibrated optical microscope. Using the SEM before each AFM experiment is not practical, because it requires considerable amount of time and access to one. Non-conducting surfaces also need to be coated with a conducting material, which changes the surface chemistry of the cantilever tip.

There are two types of loading methods. For the first method, a mass is hung from the cantilever and the deflection of the AFM cantilever is measured allowing the spring constant to be calculated. Hanging a mass from a cantilever is time consuming and potentially destructive, making it not viable for in-situ use. Using the second method, a cantilever with an unknown spring constant is pushed against a cantilever (force calibration cantilever) with a known spring constant. This is also time consuming, which is its biggest drawback for in-situ use. The loading method, however, is attractive for artifact transfer[24].

The method that is most viable for in-situ characterization is the thermal method (independent of material properties of the AFM cantilever), requiring knowledge of instrument parameters and the mean-square amplitude vibrations of the cantilever as a function of frequency only, which can be efficiently and quickly measured before each experiment.

When a cantilever is hanging freely in air there is a small external force transferred to the cantilever due to the air molecules colliding with the cantilever. The air molecules and cantilever are assumed to be in thermal equilibrium, so the average

external force on the cantilever is zero, but the fluctuations about the average are not zero.

The total potential energy can be approximated as being equal to the interaction potential, since the average external force is zero. Assuming the interaction potential is just a function of position, the negative slope of the potential is the external force.

$$\langle F_{external} \rangle = -\left\langle \frac{dV_{interaction}}{dR} \right\rangle \sim 0; \tag{3.1}$$

Taylor expanding the interaction potential, the first order derivative goes to zero, derivatives greater than two are dropped, and the zero-point energy [V (r_0)] can be chosen to be zero.

$$V(r) = V(r_0) + \frac{dV(r)}{dr}(r - r0) + \frac{1}{2!}\left(r - r0\right)^2 \frac{d^2V(r)}{dr^2} + \ldots.. \tag{3.2}$$

This allows for us to make the harmonic approximation.

$$\frac{dV(r)}{dr} \sim 0 = -F_{external} + \left(r - r0\right)\frac{d^2V(r)}{dr^2} \rightarrow F_{external} = -\delta r \frac{d^2V(r)}{dr^2} = -k\delta r \tag{3.3}$$

The external force is linear with the displacement from equilibrium, differing only by a constant slope, which is determined by the curvature of the potential ($\frac{d^2V(r)}{dr^2}$). For very small displacements about equilibrium, the harmonic approximation is viable[70].

Now that we know that the harmonic approximation is viable, we can relate the harmonic potential for a spring to the average kinetic energy. The equipartition theorem states that for each degree of freedom the average kinetic energy is equal to $1/2k_bT$. We assume that motion of the cantilever in the x and y direction are either constrained or decoupled from the normal direction (z-direction). So, the total thermal energy in the z-

direction is $1/2k_bT$. Equating the potential energy of the spring and the thermal energy, the spring constant is calculated by normalizing the thermal energy by the mean-square fluctuation of the cantilever ($k = k_bT/\langle z^2 \rangle$)[28, 71]. The AFM measures the angular changes (virtual deflections) rather than the deflection directly, so it is necessary to correct the mean-square amplitude of the cantilever vibration to account for those angular changes. The fundamental mode (natural resonance) is the only mode that is considered, not the entire thermal spectrum. The total energy must be repartitioned into the first mode (fundamental mode) to account for the cantilever deflection, since we only measure the first mode.

A few items need to be measured with the AFM before measuring the spring constant of the cantilever. The first is the movement of the laser beam on the photodiode in units of nanometers to voltage ($\delta z/\delta v$). Typically, this can be measured by taking a force curve on a sample that is much stiffer than the cantilever. If the sample is very stiff, the observed deflection is due entirely to the cantilever. The slope of the force curve versus scanner position will be the conversion factor, $\delta z/\delta v$, in units of nm/V. Second, the actual amount of scanner motion must be determined using interferometric techniques [the term with λ in Equation (3.7)]. Third, one must account for the angle of repose of the cantilever (ϕ). Different cantilever holders might have different angles of repose (10.739° for unmounted cantilever holders). Fourth, the height of the tip and length of the cantilever need to be measured. The length of the cantilever and height of the AFM tip can be measured with an SEM or calibrated optical microscope.

The virtual mean-square amplitude for each mode of oscillation is[23, 71]

$$\left\langle z_i^{*2} \right\rangle = \frac{16 k_b T}{3 k \alpha_i^2} \left(\frac{\sin(\alpha_i)\sinh(\alpha_i)}{\sin(\alpha_i)+\sinh(\alpha_i)} \right)^2 . \tag{3.4}$$

The real mean-square amplitude for each oscillation mode is

$$\left\langle z_i^2 \right\rangle = 12 \frac{k_b T}{\alpha_i^4 k} . \tag{3.5}$$

Dividing Equation (3.5) by (3.4), the conversion from virtual deflection to real deflection is

$$\left\langle z_i^2 \right\rangle = \frac{9}{4} \left(\frac{\operatorname{csch}(\alpha_i)+\csc(\alpha_i)}{\alpha_i} \right)^2 \left\langle z_i^{*2} \right\rangle . \tag{3.6}$$

To measure the spring constant of the cantilever with the thermal method, we acquire the A-B signal (difference voltage) as a function of time while the cantilever is hanging freely in air. That signal is Fourier transformed and a power spectrum is made. The resulting power spectrum has voltage squared along the y-axis and frequency along the x-axis. Before meaningful quantitative data can be obtained, the power spectrum y-axis must be converted to nanometers squared. Taking into account references 22, 23, 28, and 71, the conversion from mean-square voltage to mean-square nanometers for the first vibrational mode is

$$\left\langle z_1^2(\nu) \right\rangle = \frac{9}{4} \left(\frac{\operatorname{csch}(\alpha_1)+\csc(\alpha_1)}{\alpha_1} \right)^2 \left[\frac{1}{\cos(\theta)} \right]^2 \left[\frac{\lambda}{\Delta z_p (1+\cos(2\theta))} \right]^2 \left[\frac{1-\frac{2h_t}{L}\sin(\theta)}{1-\frac{3h_t}{2L}\sin(\theta)} \right]^2 \left[\frac{\delta z}{\delta V} \right]^2 \left\langle \Delta V^2(\nu) \right\rangle , \tag{3.7}$$

where $\alpha_1 = 1.88$, ϕ is the angle of repose (10.739 °), L is the length of the cantilever, h_t is the height of the tip, λ is the wavelength of the AFM laser (664.83 nm), Δz_p the distance between peaks on the interferogram (344.37 nm), and $\delta z/\delta V$ is the conversion factor from volts to nm. The first two terms on the right side of Equation (3.7) are constant. The third

term on the right side of Equation (3.7) depends on the type of cantilever holder. The fourth term on the right side of Equation (3.7) is negligible for commercial AFM tips, but is important for large beads attached to tipless AFM cantilevers. The fifth term on the right side of Equation (3.7) is dependent on the AFM alignment laser wavelength and scanner calibration. The last two terms on the right side of Equation (3.7) are measured during each calibration (see Appendix B, C, and D).

Now that the power spectrum has been converted to mean-square nanometers, we can fit the first fundamental to an equation that has five parameters. Three (the quality factor, kinetic resonance, and the mean-square amplitude at kinetic resonance) of the five parameters are used to calculate the spring constant.

$$\left\langle z^2(\nu)\right\rangle = \frac{A}{\nu} + B + \left(\frac{\left\langle z^2(\nu_k)\right\rangle}{Q^2}\right)\left(\frac{1}{\left\{\left[1-\left(\frac{\nu}{\nu_k}\right)^2\right]^2 + \left[\frac{\nu}{\nu_k Q}\right]^2\right\}}\right), \tag{3.8}$$

where ν is the x-axis (frequency), A is the coefficient for the 1/f noise, B is the white noise, Q is the quality factor of the oscillator, $\langle z^2(\nu_k)\rangle$ is the mean-square amplitude at kinetic resonance, and ν_k is the kinetic resonance.(See reference 28 for details.) Once Equation (3.8) is fit to the experimental data, three fit parameters are used to calculate the spring constant (Q, ν_k, and $\langle z^2(\nu_k)\rangle$)

$$k = 0.9707\frac{Q k_b T \Delta\nu}{\pi\left\langle z^2\left(\nu_k\right)\right\rangle \nu_k}, \tag{3.9}$$

where k_b is Boltzman's constant, T the temperature in Kelvin, and $\Delta\nu$ is the frequency resolution of the data acquisition device.

As an example for the method (Figure 3.2.1-1), the spring constant for an NSC21 A cantilever was measured. The conversion from nanometers to voltage ($\delta z/\delta V$) on mica was 87.6 nm/V and on the x-y stage was 91.0 nm/V. The difference between the conversion factors using mica and the x-y stage was not statistically significant. $A = -0.965\ nm^2 Hz$, $B = 1.43 \times 10^{-5}\ nm^2$, $Q = 52.4$, $\langle z^2(\nu_k) \rangle = 6.29 \times 10^{-3} nm^2$, $\nu_k = 12.9$ kHz, $k_{thermal} = 0.04$ N/m (see Equation (3.8) and (3.9)). The manufacturer reported the nominal spring constant as 1 N/m.

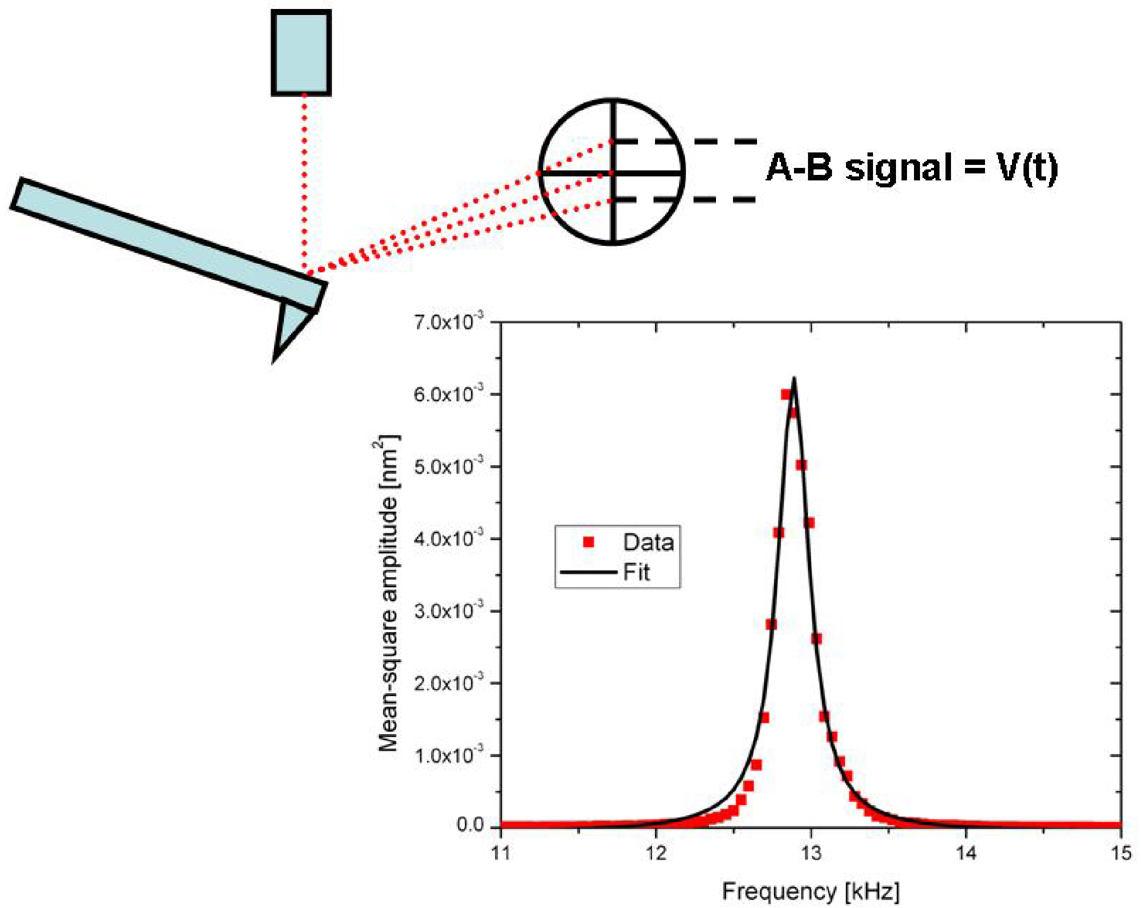

Figure 3.2.1-1. Schematic diagram for acquiring the A-B signal and sample thermal spectrum data. The A-B signal of the cantilever hanging freely in air is acquired, a thermal spectrum is built, and the result is fit to equation (3.8).

3.2.2. Thermal versus loading methods: A comparison with a NIST calibrated piezolever

Cantilevers with spring constants traceable to the SI (System International) fundamental unit are currently not available. In this sub-section we describe the measurement of the spring constant for an unknown AFM cantilever using piezoresistive cantilevers that were calibrated at NIST (National Institute of Standards and Technology) using the Electrostatic Force Balance (EFB)[24]. A piezoresistive cantilever is one that changes resistance under an applied force. The change in resistance and the applied force on the cantilever can be measured accurately, which could lead to a spring constant that is traceable to fundamental SI units. The spring constant of the unknown cantilever can be calculated, by pushing, with the unknown cantilever against a traceable cantilever, since they experience the same applied force. The piezoresistive cantilevers were calibrated at NIST, but have not been confirmed traceable to fundamental SI units. The piezoresistive cantilevers from NIST are the most accurately calibrated cantilever's available and are part of an ongoing research program to produce a traceable standard. The rest of this section will describe how to calculate an unknown cantilever spring constant and some issues with the method (see Appendix E).

From reference 26, the spring constant for an unknown tipless cantilever pushing against the piezolever is

$$k_1 = \frac{S_r}{S_v}\frac{\Delta R}{\Delta V}\cos(\psi)\frac{\left(1 - \frac{3h_{tp}}{2L}\tan(\psi)\right)}{\left(1 + \frac{3h_{tp}}{2L}\tan(\phi)\right)}. \qquad (3.10)$$

For NIST cantilever #1, S_r = 260.7 nN/ohm (measured sensitivity), S_v is the slope of a force curve taken on a stiff sample for the unknown lever, L = 280 μm (measured length of piezoresistive cantilever), ϕ = 10.739 ° (angle of repose of the unknown cantilever), ψ = 11 ° (the angle between the piezolever and the base of the AFM stage), and h_{tp} = 4.5 μm (assumed height of the tip for the piezoresistive cantilever).

A method needed to be developed which would simultaneously acquire the change in resistance of the NIST cantilever and the A-B (deflection) signal of the unknown cantilever, and after much tweaking, that method was found. The unknown AFM cantilever was ramped into and out of contact (20 sec/cycle) in the xy trace mode with the piezoresistive cantilever. The resistance was measured with an Agilent 3301A multimeter (meter was assumed accurate). HP VEE (software for data acquisition) acquired the resistance data from the multimeter and placed the data points (1200 points in 20 seconds) into a text file. The maximum resistance, minimum resistance, and the corresponding total change in resistance (ΔR; see Figure 3.2.2-2) were calculated with a common spreadsheet.

The A-B signal and the deflection of the cantilever were acquired simultaneously using an Agilent 5461D oscilloscope. The oscilloscope was not calibrated, but was compared for consistency to a signal generated from a function generator. The total change in the A-B signal (ΔV_{NIST}; see Figure 3.2.2-3) as the scanner was ramped was the total deflection of the cantilever in units of volt, which must be converted to units of nanometer. The conversion was performed by ramping the same unknown cantilever into and out of contact with a stiff surface (mica is a very stiff and flat surface relative to the AFM cantilever), so that the deflection was due to the unknown cantilever alone. The

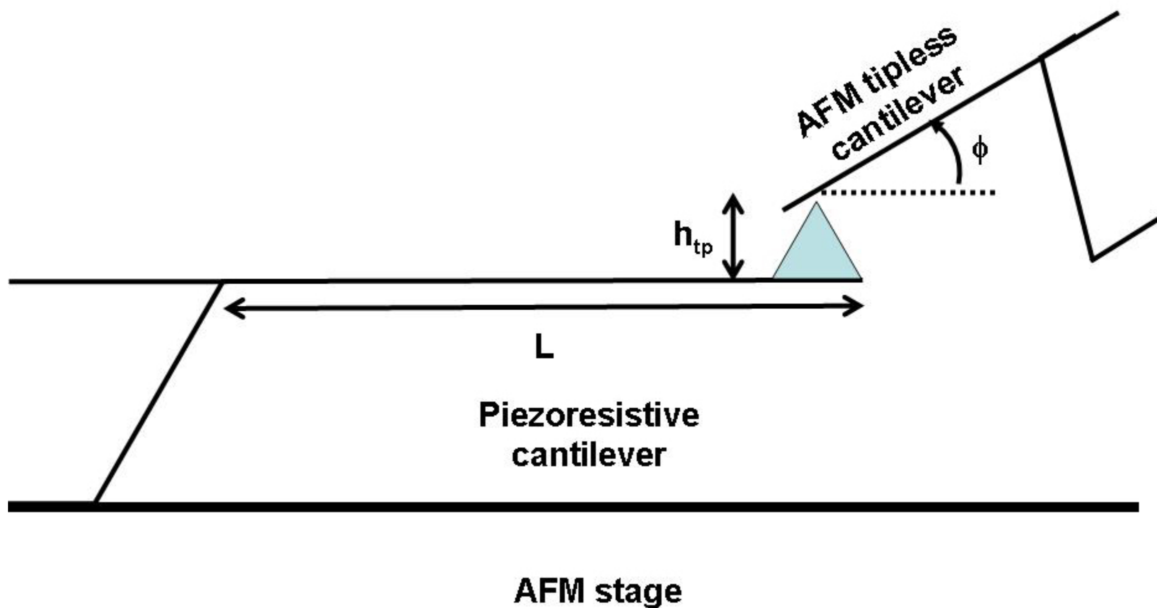

Figure 3.2.2-1 Diagram of a tipless AFM cantilever in contact with a piezoresistive cantilever calibrated at NIST. The unknown tipless cantilever is pushed against the cantilever calibrated at NIST (piezolever) and the unknown spring constant was calculated (see Equation (3.10)). ψ = 0 degrees, as pictured in the figure.

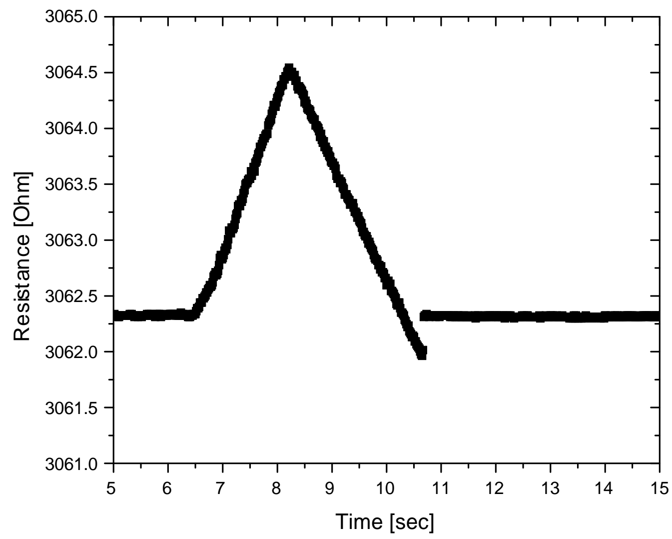

Figure 3.2.2-2. Sample resistance data from an Agilent 3301A multimeter. The total change is ΔR.

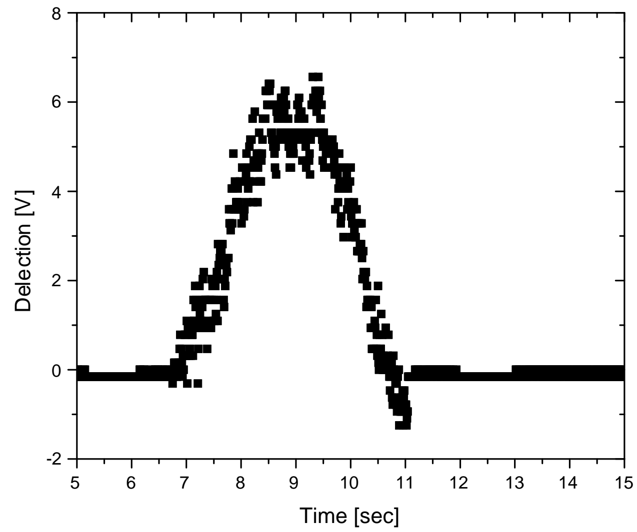

Figure 3.2.2-3. Sample data acquired from the oscilloscope (the AFM A-B or deflection signal). The total change is ΔV_{NIST} (The deflection of the cantilever while on the piezoresistive cantilever).

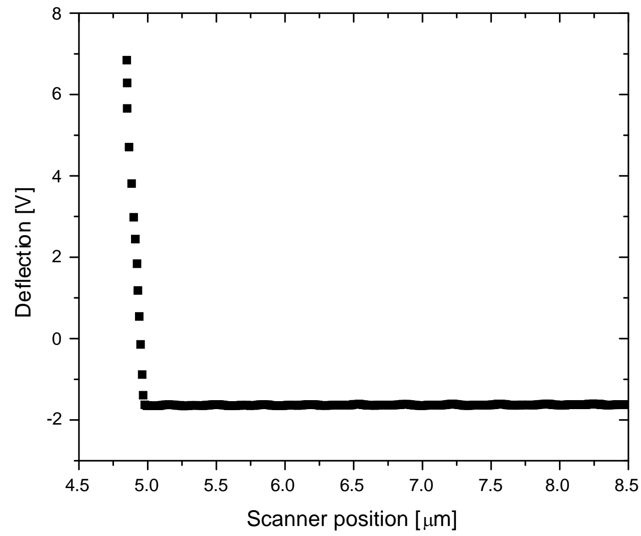

Figure 3.2.2-4. Sample data acquired by the AFM. A-B as a function of scanner position. The inverse of the slope is the conversion factor (($\delta Z/\Delta V)_{mica}$; (the deflection of the cantilever while on mica).

inverse slope of that curve gives the conversion factor (in units of nm/V; $(\delta Z/\Delta V)$; see Figure 3.2.2-4) for converting the deflection of the AFM cantilever (total A-B change) from units of volts to units of nanometers.

The spring constant as measured with the NIST method was compared to the thermal method[26], and they were found to agree within 10% of each other. The calculated uncertainty in the spring constant for the thermal method was estimated by the method of quadtrutures by

$$\delta k = \sqrt{\left(\frac{\partial k}{\partial \Delta R} d\Delta R\right)^2 + \left(\frac{\partial k}{\partial s} ds\right)^2 + \left(\frac{\partial k}{\partial L} L\right)^2 + \left(\frac{\partial k}{\partial h} dh\right)^2 + \left(\frac{\partial k}{\partial \phi} d\phi\right)^2 + \left(\frac{\partial k}{\partial \delta 1} d\delta 1\right)^2 + \left(\frac{\partial k}{\partial \delta z} d\delta z\right)^2} \quad (3.11)$$

where $s = \delta z/\delta v$.

The calculated thermal spring constant was for a 1-shot spectra which seems to be suitable for coated cantilevers that are more compliant. Spectra for stiff and uncoated cantilevers are noisier and have resonance peaks just above the noise. One must be careful while fitting single spectra for stiff and uncoated cantilevers, since there may be spurious data points. The NIST cantilevers were calibrated by measuring the sensitivity (s) at a known loading point (at the piezoresistive cantilever tip). The unknown cantilever must make contact at the same loading point. For unknown cantilevers without a tip, making contact with the piezoresistive cantilever tip is relatively straightforward. For unknown cantilevers with a tip, contact must be made at a location other than the tip of the piezoresistive cantilever, which brings into question the accuracy of the sensitivity factor. When checking the calibration with the piezoresistive cantilevers it is best to use unknown tipless cantilevers. Compliant AFM cantilevers in contact with the piezoresistive cantilevers can saturate at pull-off. One must be careful to obtain good ΔV_{NIST} values. Stiffer AFM cantilevers seem to have the fewest complications. The

height of the cantilever tip (h_t) was assumed to be 4.5 microns and made a small contribution to the overall uncertainty. The length of the cantilever (L) was measured with the AFM microscope. However, L made a small contribution to the overall uncertainty (assumed uncertainty ± 1micron). Reasonable attempts were made to keep both cantilevers parallel to each other. Since the spring constant as measured by the NIST method and the thermal method were so close, this issue was assumed small.

3.2.3. Tip radius calibration

The topography image is a dilation of the sample surface and the inverted image of the AFM tip surface[64]. When the surface features are much smaller than the tip size, the shape of the tip dominates the topography image. To calibrate a commercial AFM cantilever tip (a cantilever with conical or spherical tip attached by the manufacturer), a delta function grating can be imaged to determine the tip size. The delta function grating is a series of spikes that are assumed to have dimensions much less than the tip size. By imaging this grating, one can obtain an inverted image of the tip[72]. If the radius of the tip becomes too large (similar to the spacing between spikes), the delta function will not trace out the entire radius of the tip, so a step is used instead (Appendix F and G)[27].

The resulting topography image from imaging a step with a larger AFM tip is an inverted image of the tip. When the step turns upward, the slope of the step is much larger than the slope of the tip, which is what causes an inverted image of the tip to be imaged (Figure 3.2.3-1 and Figure 3.2.3-2). To measure the radius of the larger AFM tip, the radius at each point along the inverted image is assumed constant. Each point along

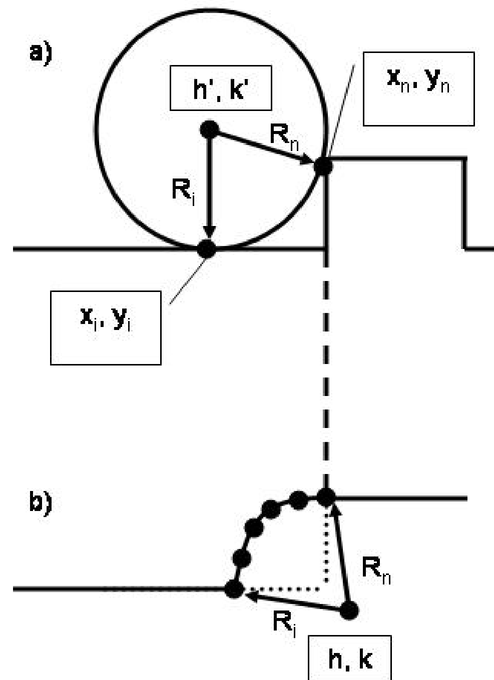

Figure 3.2.3-1. a) Schematic cross-sectional view of a single sphere and a step function. b) The expected cross-sectional data, after averaging all scan lines of the topography image, and their relation to the radius and center of a circle.

the inverted image is fit to a circular arc

$$R = \sqrt{(z-h)^2 + (x-k)^2}, \tag{3.12}$$

where z is the height, x is the distance in the fast-scan direction of the AFM cantilever, and h and k are the center of the circle.

The parameters h and k (the center of a circle whose radius is R) are changed repeatedly, using a solving function in a commonly used spreadsheet (Excel solver feature) until the standard deviation for the radius for each of the points along the inverted image of the tip is minimized according to (Appendix F)

$$\delta R = \sqrt{\frac{N\sum_i^N R_i^2 - \left(\sum_i^N R_i\right)^2}{N(N-1)}} \sim 0. \tag{3.13}$$

The average value for all radii was the reported value for the radius of the larger AFM tip. The accuracy for the measurement was estimated to be 9% and the precision 4%. For details about this method, see reference 27.

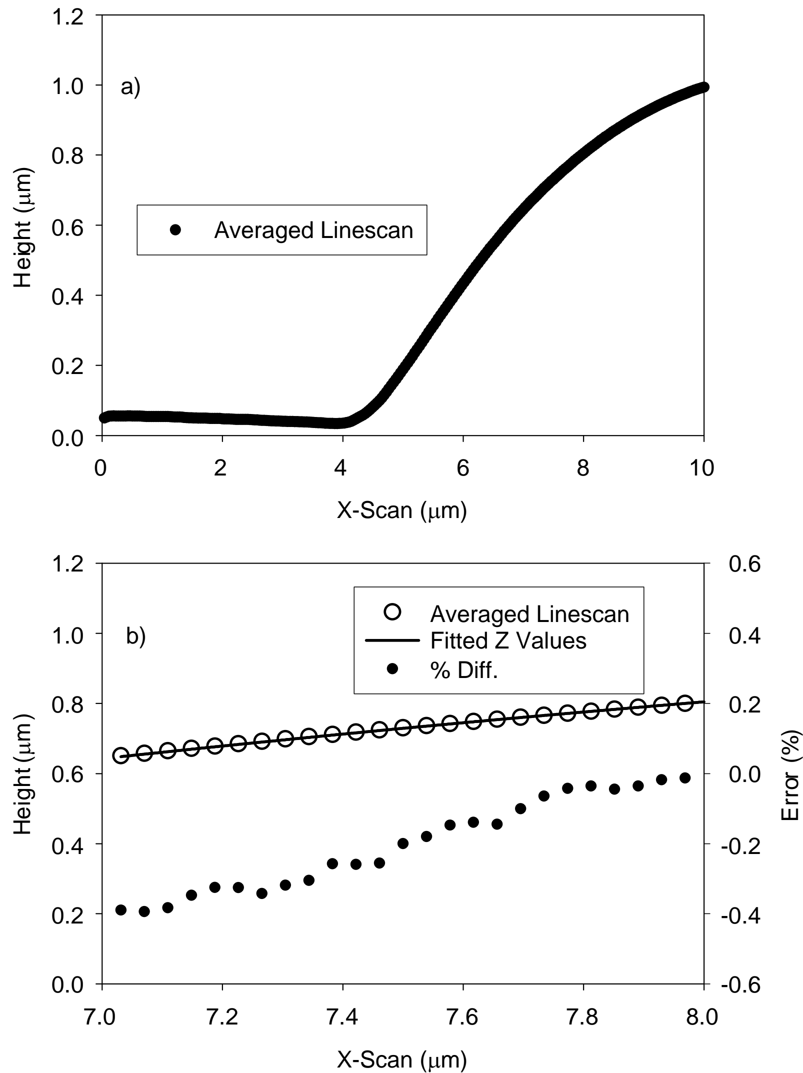

Figure 3.2.3-2. a) A typical graph of a 48 μm sphere with all line scans averaged from a 256 by 256 pixel topography image that was 10 by 10 μm^2. b) The scale on the right corresponds to the percent difference between the fit and the data. The best choice for the data range was one in which the percent difference was less than or equal to ± 5%. The scale on the left corresponds to the height of the average cross-sectional data and the circular fitted results. Note that it is difficult to distinguish between the fitted data and the actual data.

3.2.4. Surface Roughness Calibration

After an experiment, the surface roughnesses of the AFM tips were measured using two different approaches (See Appendix H for other methods). The surface roughnesses of some of the tips were measured with a delta function grating by imaging a small portion of the tip. The surface roughnesses of the other tips were measured by flipping a very stiff (~ 40 N/m) cantilever upside down, attaching it to a substrate, and imaging the tip over a small portion of the flipped-over tip (FOT). The FOT method was required to measure the RMS roughness for attached beads. The AFM tip is much smaller than the attached beads so the topography image acquired represented the surface of the attached bead. A single method to measure the surface roughness is preferred, but the spacing of the delta-function grating is too small to use for larger sized beads, and the FOT method is only valid for tip sizes that are much larger than the flipped-over tip. Imaging the beads via the FOT method does not guarantee that the actual contact area was imaged. To determine the surface roughness of the tips, the scan range was fixed (for the topography image) at approximately 0.5 μm.

3.3. Sample preparation / type of samples

The samples for this study were unpatterned single crystal silicon die (2.5 mm by 2.5 mm) that had been solder-sealed into 5 mm x 5 mm LCC (Leadless Ceramic Chip Carrier) packages during manufacturing in order to minimize surface contamination. Preliminary studies showed that commercial die attach products often emit vapors when

they are cured. These vapors can affect the surface so only die that had been placed loosely in the package (no die attach) were used in the work reported here. The samples were removed from the LCC packages in the laboratory, and placed onto the AFM stage immediately before measurement.

Two surface conditions were evaluated. One was the silicon dioxide surface formed on wafers after a standard silicon clean, referred to as Untreated No Die-attach (UND). The second was this same material after treatment with organic groups (a few angstroms of vapor deposited diphenylsiloxane), referred to as Treated No Die-attach (TND). Although deposited as an aromatic silicon oxide at high temperature, some of the organic groups react at the surface. The result is a silicon oxide surface that is infused with both aromatic and saturated organic groups.

The packaged silicon die were singulated using a 56 mil diameter (1400 microns) punch. The wafers were diced upside down with the punched tape to preserve surface quality, and it was assumed that the tape did not cover the center of the die. The die on the wafers were inspected for visual evidence of trace residue from the tape. There was no trace on one wafer, but the other wafer had a slight trace of residue on the two die on opposite sides of the wafer.

The first wafer, Wafer 25, was a freshly cleaned, uncoated silicon wafer. Oxide thickness measurements were made using a Prometrix 1280 ellipsometer. The mean thickness was 10.95 angstroms and it varied by 0.75 angstroms across the wafer. The change in surface film thickness due to the die attach and solder seal were measured using a manual ellipsometer with microspot optics. This ellipsometer gave slightly different thickness measurements (11.3 angstroms with microspot optics).

The other wafer, Wafer 14, was similar to Wafer 25, but treated with a few angstroms of diphenylsiloxane in Analog Devices, Inc.'s production Chemical Vapor Deposition (CVD) system. Film (oxide plus diphenylsiloxane) thickness measurements were made with the Prometrix 1280 ellipsometer. The mean thickness was 20.42 angstroms and it varied by 0.87 angstroms across the wafer. The change in surface film thickness due to the die attach and solder seal were measured using a manual ellipsometer with microspot optics. This ellipsometer gave slightly different thickness measurements (19.1 angstroms with microspot optics).

Four different types of tips and many different sizes of radii were employed in this study. The first type of tip was referred to as the commercial AFM tips, since they were silicon cantilevers that had pre-existing tips on them when purchased from the manufacturer. The second type of tip was silicon dioxide ($Si0_2$) beads attached to tipless AFM cantilevers[27]. The third type of tip also had attached $Si0_2$ beads, except they were coated with a monolayer of vapor deposited diphenylsiloxane. The fourth type of tip was heat-treated in a tube furnace at roughly 900°C for different lengths of time (the length of time was related to the size of the tip; Appendix F and G)[67].

CHAPTER 4

4. Results and discussion

The following ten subsections will graphically display the principal results for this work and the last section will discuss those results. For other work, please see Appendices I and J.

The material properties can influence the adhesive force between the cantilever and sample surface. To be consistent among all adhesion experiments, a few tests must be performed to determine if there is an influence due to different conditions. First, the adhesive force might vary with the maximum load on the cantilever. When the load is high enough, plastic deformation might happen, which would influence the adhesion force. Figure 4.1.1-1 displays the influence of the maximum load on the cantilever to the adhesive force.

Second, the rate at which the tip and sample are brought together might influence the adhesive force. Even at the fastest rate of acquisition the speed of approach and retraction is extremely slow, but the adhesive force as a function of rate should be tested to be certain that the acquisition rate setting does not influence the adhesion data (Figure 4.1.2-1).

Third, for adhesion experiments in air, it is generally accepted that water is expected to be always present on the sample surface, so the influence of relative humidity on the adhesion force must be tested (Figure 4.1.2.1-1).

In addition to the material properties, surface roughness of the AFM tips might influence the adhesion and work of adhesion data. Figure 4.1.3-1 indicates how the

surface roughness of the AFM tips varies with the radius of the tip. Figure 4.1.4-1 through Figure 4.2.1.4-1 indicate the principal results for this study, which include data that has and has not been corrected for surface roughness for the untreated (UND) and treated no die (TND) attach sample.

4.1. Results

4.1.1. Adhesive force [nN] versus load [nN]

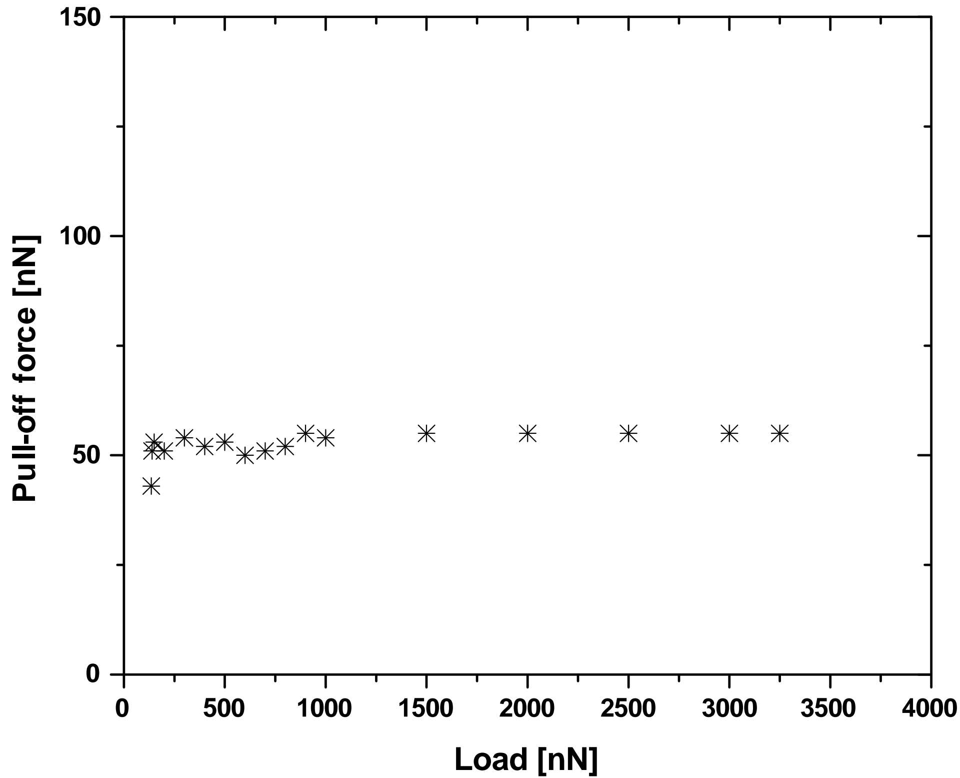

Figure 4.1.1-1. Pull-off force as a function of increasing maximum load on the cantilever. The pull-off force is constant as the load on the cantilever increases. The sample was the untreated no die-attach die (UND) and the AFM tip was an attached SiO_2 bead, with a radius of approximately 15 μm.

4.1.2. Adhesive force [nN] versus approach /retraction rate [Hz] results

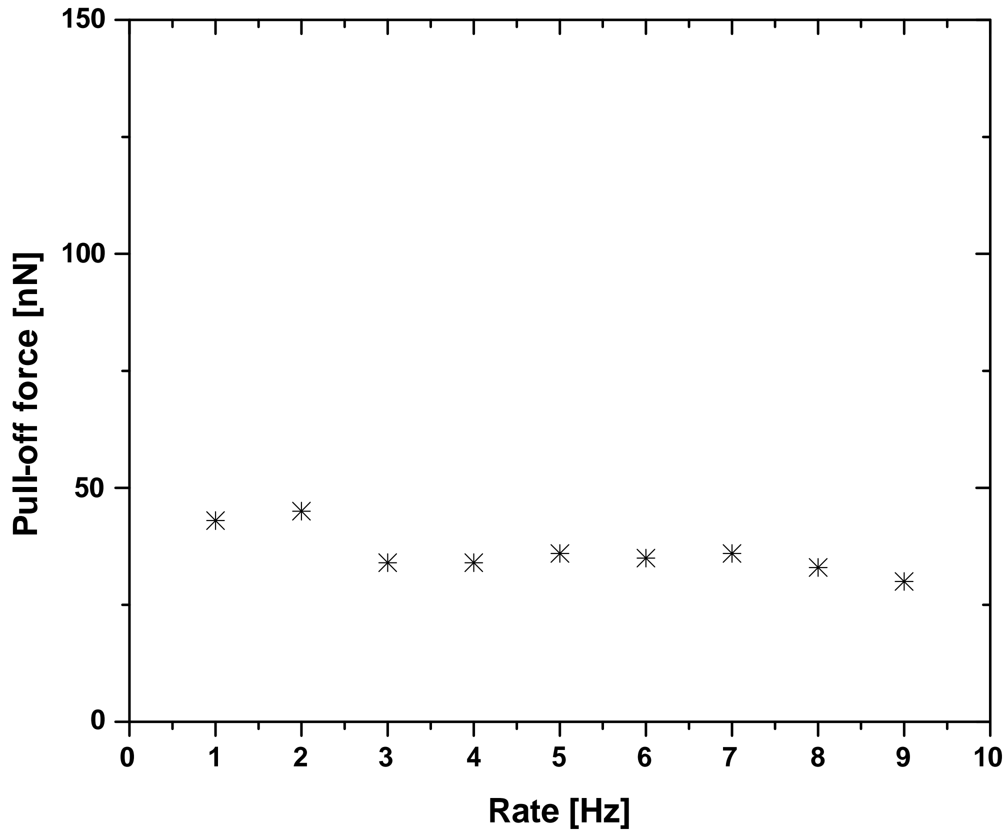

Figure 4.1.2-1. Pull-off force as a function of increasing rate of force curve acquisition. The pull-off force is roughly constant as the rate of force curve acquisition increases. The sample was the untreated no die-attach die (UND) and the AFM tip was an attached SiO_2 bead, with a radius of approximately 15 μm.

4.1.2.1. Adhesive force [nN] versus relative humidity [%] results

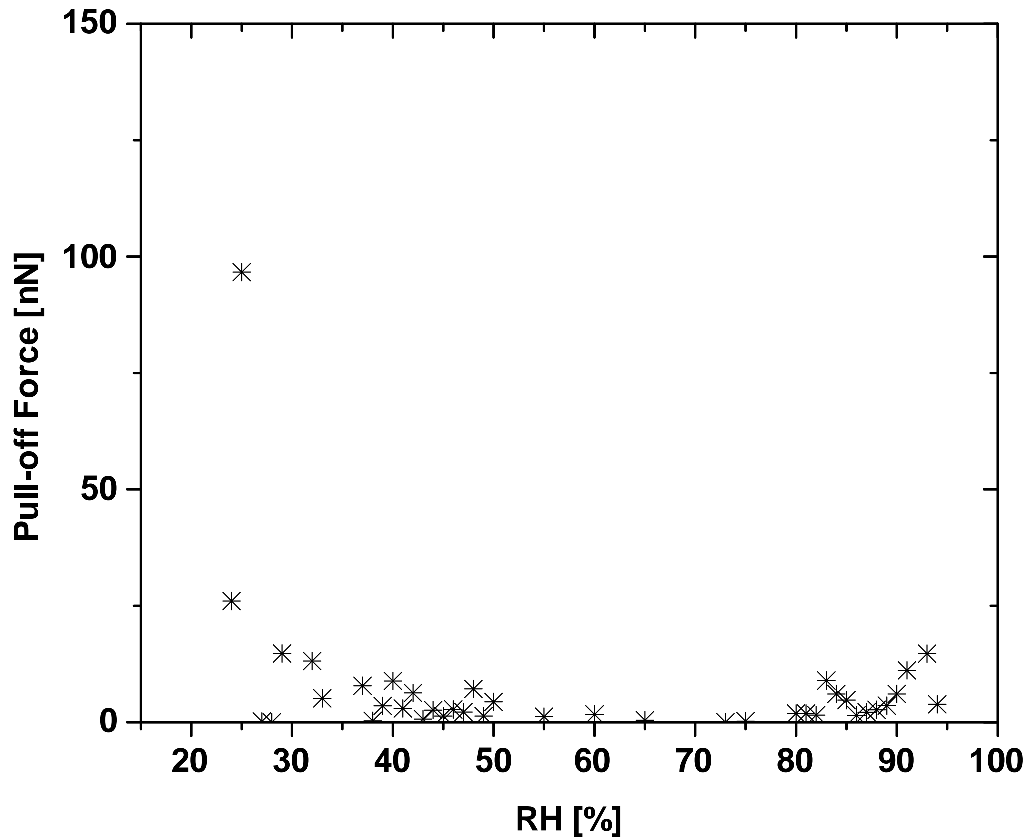

Figure 4.1.2.1-1. Pull-off force as a function of relative humidity (RH). The pull-off force appears approximately constant within the range of about 30-80%, which was as close as possible to fab conditions. The sample surface was the untreated no die-attach (UND) and the tip was a commercial AFM tip.

4.1.3. RMS roughness [nm] versus radius [μm] results

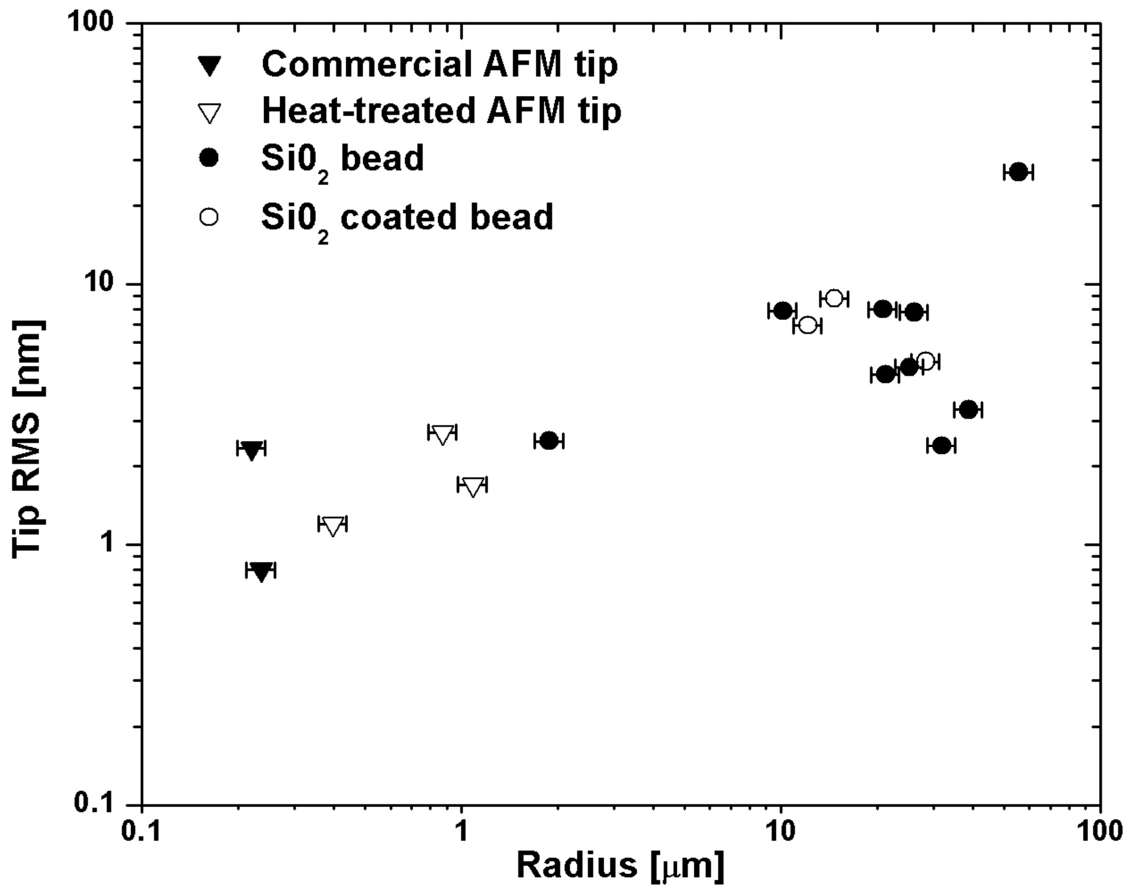

Figure 4.1.3-1. AFM tip RMS roughness as a function of tip radius. The RMS roughnesses of the AFM tips were measured with different techniques, explained in the text (Section 3.2.4).

4.1.4. UND adhesive force [nN] versus radius [μm] results

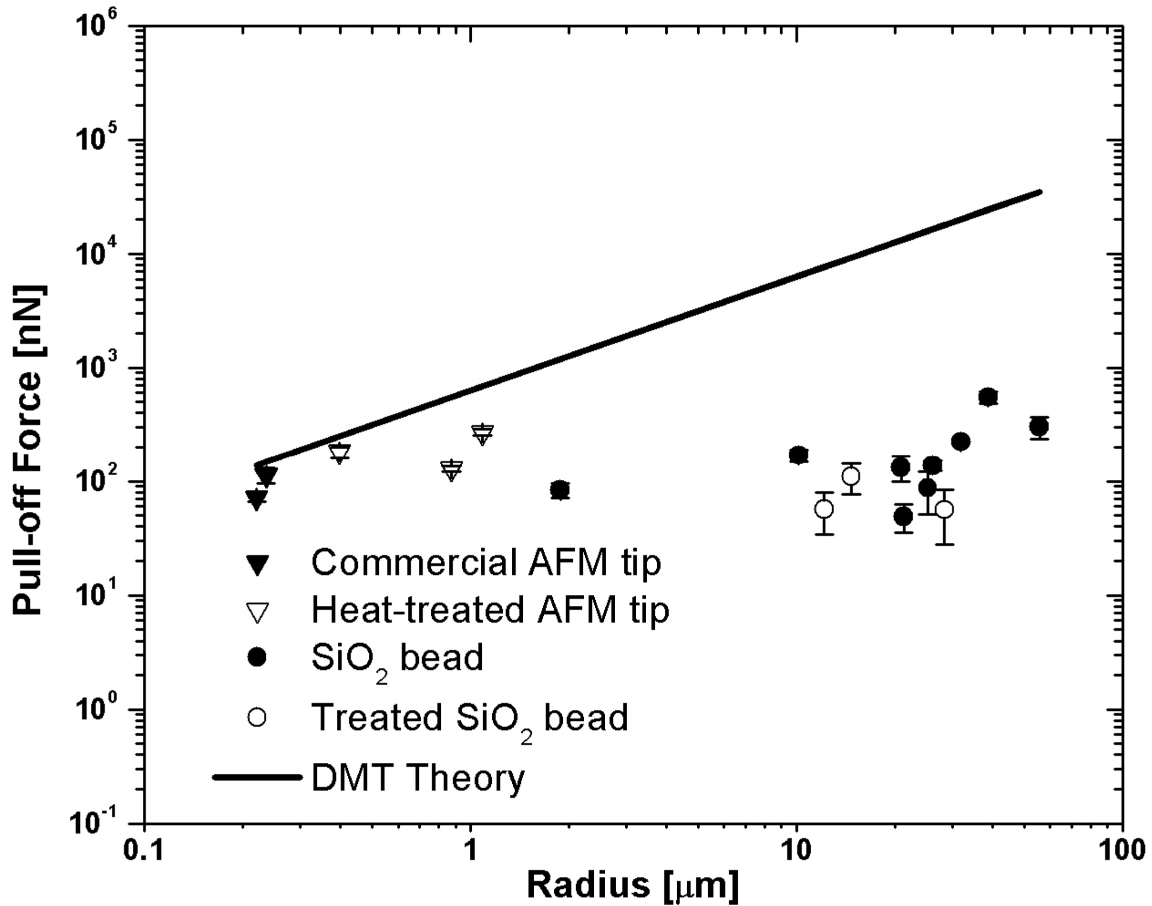

Figure 4.1.4-1. Pull-off force as a function of radius compared to DMT theory for the untreated no die-attach sample Theoretically we estimated, using Equation (2.15), the work of adhesion to be 100 mJ/m^2, which was for treated silicon dioxide (A = 1x10^{-19} J). The pull-off force was corrected for effects due to the angle of repose.

4.1.5. TND adhesive force [nN] versus radius [μm] results

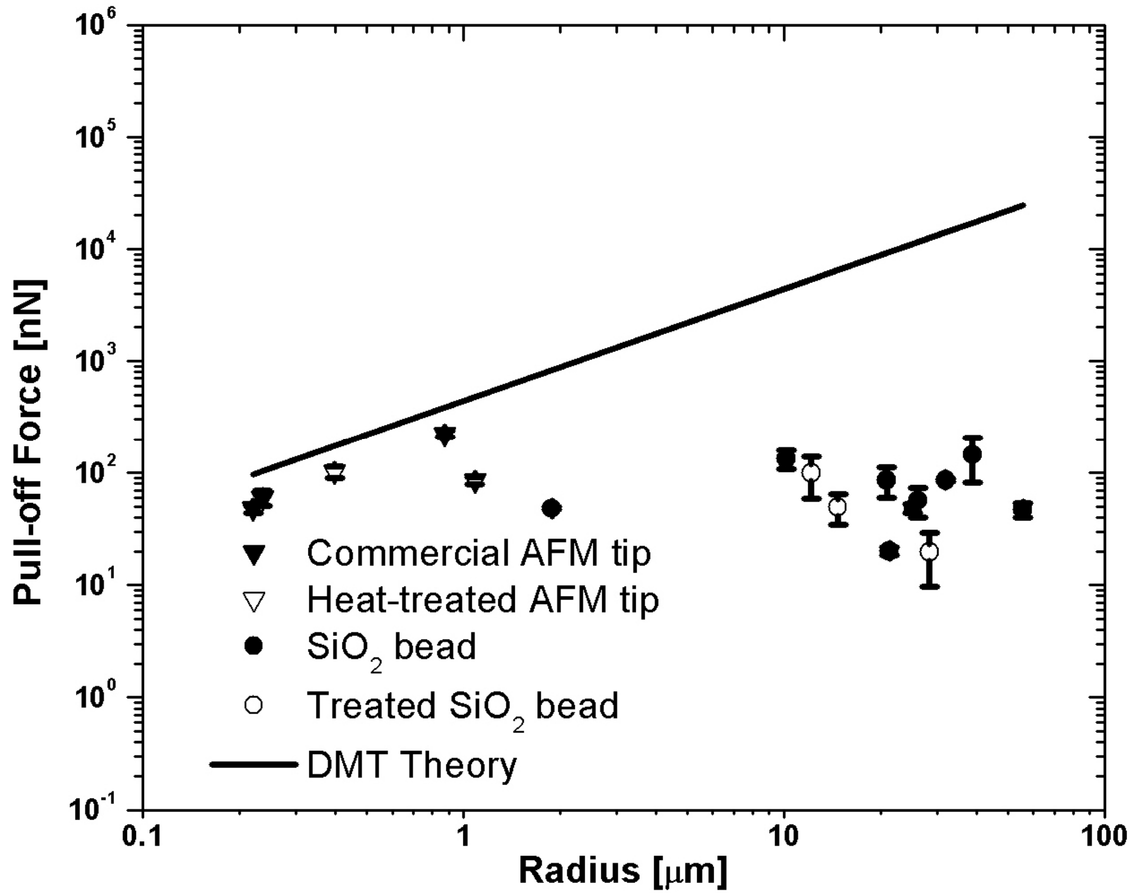

Figure 4.1.5-1. Pull-off force as a function of radius compared to DMT theory for the treated no die-attach sample Theoretically we estimated, using Equation (2.15), the work of adhesion to be 70 mJ/m², which was for treated silicon dioxide (A= 0.7×10^{-19} J). The pull-off force was corrected for effects due to the angle of repose.

4.2. Discussion

In this section we discuss the plots from the results section. We start with the plots that show the influence of material properties and environmental conditions. Next, the influence of surface roughness is discussed in a subsection entitled “Surface roughness.” The surface roughness subsection discusses how the unexpected behavior from Figure 4.1.4-1 and Figure 4.1.5-1 was handled, what influence the angle of repose correction had on the experimental data, the influence on the work of adhesion, and the influence of plastic deformation of the asperities. Finally, we conclude this section with an additional subsection entitled “The physics of contact,” which describes the physical implication of the surface roughness in adhesion.

Both Figure 4.1.1-1 and Figure 4.1.2-1 indicate that the adhesive force is independent of the maximum load on the cantilever and the rate of force curve acquisition, which means that these parameters do not influence the adhesion within the ranges tested.

There was tight quality control on the material properties of the surfaces manufactured by the fabrication facility, but the surfaces of the AFM tips were not as well controlled. The sample wafers were manufactured in a commercial semiconductor wafer fab and hermetically packaged in a Class 1000 assembly room. The packages were opened in a less stringent laboratory environment, which might have made them susceptible to adsorbed particles and hydrocarbons. Adsorbed particles, in general, would cause lower pull-off forces, influencing the measured value but not the trend. If there were different types of adsorbed particles for different tip and sample combinations, we would have expected larger scatter in the measurements. The dew point (the point at which condensation occurs) was measured in the laboratory to be about 1 °C.

[Additionally, the pull-off force as a function of relative humidity was measured. (See Figure 4.1.2.1-1.)] The densities of the materials for the AFM tip and the sample were expected to be uniform and the same.

The sample surfaces (UND and TND) were relatively flat and smooth (0.4 ± 0.5 nm RMS roughness), but not all AFM tips were smooth. The commercial AFM tips were expected to be the smoothest, making single-asperity contact with the surface (Figure 4.1.3-1). The measurement techniques for the surface roughness of commercial AFM tips are the least reliable, since the characterizer might have dimensions and surface roughnesses of the same order as the commercial AFM tips. The heat-treated tips were smooth and measurement of their surface roughness might experience the same problems as the commercial AFM tips. Figure 4.1.3-1 shows the dependence of the tip RMS roughness on the radius of the tip.

The observed behavior of the measured pull-off force data in Figure 4.1.4-1 and Figure 4.1.5-1 was contrary to continuum mechanics theoretical predictions (see Section 4.2.1). All continuum contact models predict that the force should increase linearly with the radius of the AFM tip (slope of $2\pi\varpi$ for DMT contact mechanics). The plots indicate that the force was constant as the size of the tip increases, despite more interacting molecules (material). The data were corrected for effects due to the angle of repose (Figure 4.1.4-1, Figure 4.1.5-1, and Equation (2.19); see references 22 and 23 for details).

4.2.1. Surface roughness

Section 2.2.2.2 describes the correction that we developed to handle the fact that the behavior in Figure 4.1.4-1 and Figure 4.1.5-1 did not match continuum mechanics predictions.

Figure 4.2.1.1-1 and Figure 4.2.1.2-1 clearly show that the trend is modified significantly after applying the correction due to the surface roughness (Section 2.2.2.2; Equation (2.16)), becoming similar to that predicted by DMT contact theory. However, the results were two orders of magnitude larger than expected, which was not surprising given the bold assumption that the asperities were represented by a single asperity with a radius equal to the RMS surface roughness. To measure the surface roughness of the AFM tips, a small portion of the AFM tip was measured (approximately 0.5 micron square patch). The small patch was assumed to be representative of the homogenous isotropic tip. Ideally one would prefer to measure the surface roughness within the contact area before and after pull-off force measurements, but the contact radius is expected to change with the size of the tip and load.

The measurement of the surface roughnesses might have caused the high magnitudes of the pull-off forces. It is important to remember that the topography image, used to obtain roughness values, is a dilation between the inverted surface of the AFM tip and the sample surface, which is a nonlinear relationship. Both the sample and tip might wear with use. Thus, the measured RMS value was thought of more appropriately as an interfacial roughness. Measuring the roughness within the actual contact area is

important, since the surface roughnesses might be scale-dependent. The spikes from the delta-function are assumed to have a nominal radius of 10 nm, but that could change after repeated use. Additionally, every effort was made to image the part of the sphere that makes contact with the sample surface, but measuring the point where the sphere makes contact was not an easy task. The topography image might have been acquired at a point different from the point of contact of the sphere with the sample surface. A small difference in the tilt angle of the surface roughness characterizer and the sample surface would cause different contact points on the sphere. Despite the issues with measuring the roughness, in the future the number, size and shape of the asperities should be measured because the surface roughness causes the actual contact area to be smaller than the apparent contact area.

The correction due to the angle repose during loading of the cantilever was about 4% for commercial AFM tips and 26% for the largest attached bead. Initially it was thought that the work of adhesion was an appropriate measure for stiction, and that it should have been constant as the size of the tip increases. Theoretical predictions ($\left|F_{DMT_pulloff}\right| = 2\pi R\varpi$) did not match our experimental data, and the dependence of work of adhesion on radius seemed to disagree with any known contact model. The root cause for the discrepancy was the surface roughness.

Without correcting for the surface roughness, the observed work of adhesion on radius in Figure 4.2.1.3-1 and Figure 4.2.1.4-1 (gray data points) was not expected, and it did not match continuum contact model predictions. Figure 4.2.1.3-1 and Figure 4.2.1.4-1 (dark data points) show that the correction due to the surface roughness causes the work of adhesion to become approximately constant as the size of contact (AFM tip radii)

increased. Despite the data being corrected for surface roughness, the data (values) were still much higher than the expected DMT prediction, which was not surprising due to the

4.2.1.1. Corrected UND adhesive force [nN] versus radius [μm] results

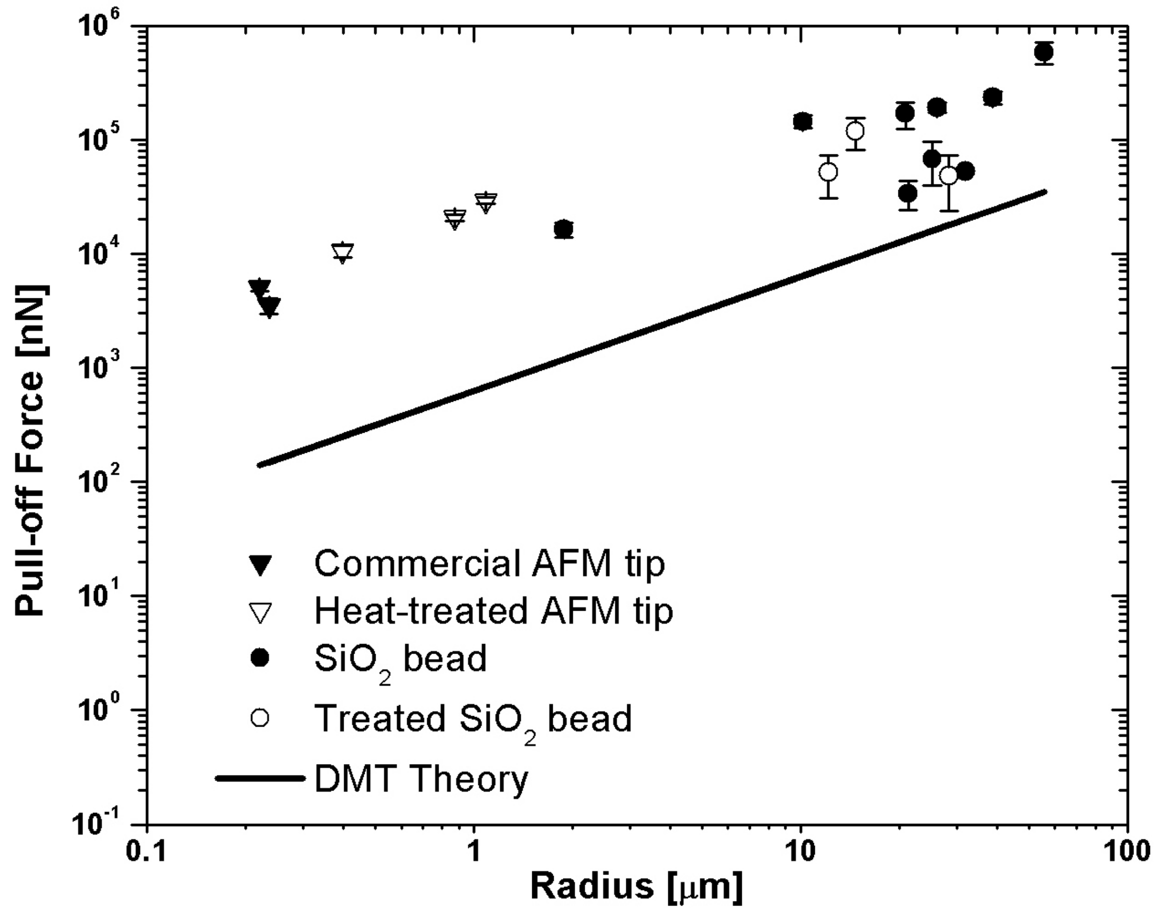

Figure 4.2.1.1-1. Pull-off force as a function of radius compared to DMT theory for the untreated no die-attach sample. The pull-off force was corrected for effects due to the angle of repose and surface roughness; the latter causes the pull-off force to become roughly linearly dependent on R.

4.2.1.2. Corrected TND adhesive force [nN] versus radius [μm] results

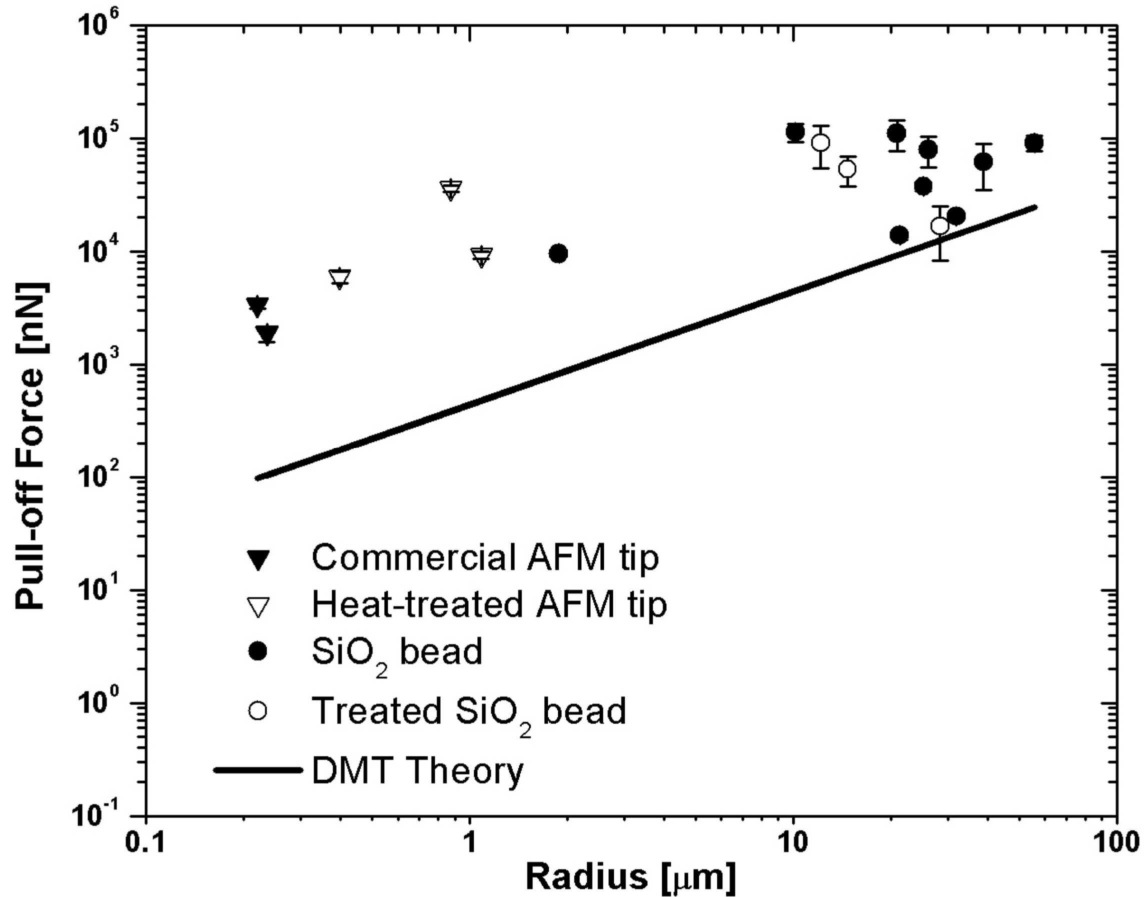

Figure 4.2.1.2-1. Pull-off force as a function of radius compared to DMT theory for the treated no die-attach sample. The pull-off force was corrected for effects due to the angle of repose and surface roughness; the later causes the pull-off force to become roughly linearly dependent on R.

4.2.1.3. Uncorrected and corrected UND work of adhesion [mJ/m^2] versus radius [μm] results

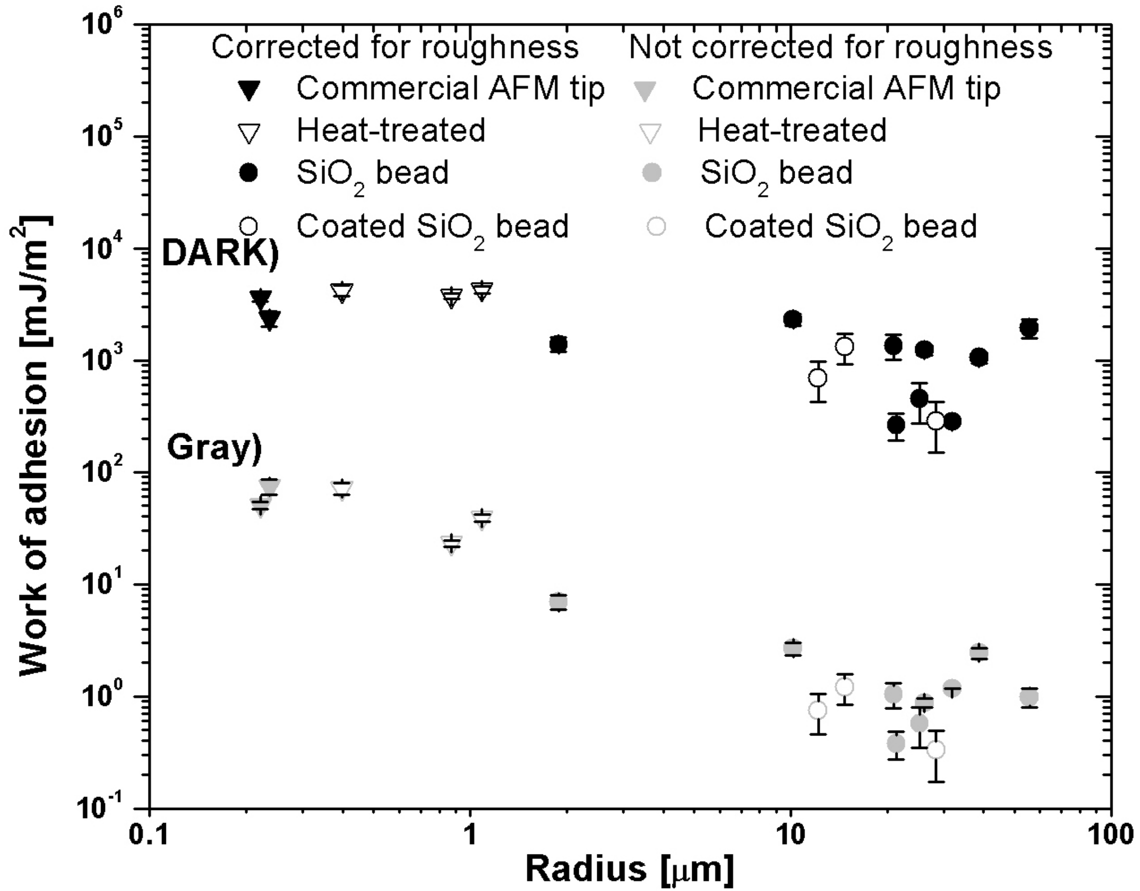

Figure 4.2.1.3-1. Work of adhesion versus radius for the untreated no die-attach sample (UND). a)The data were corrected for angle of repose and surface roughness. b) The data were corrected for effects due to the angle of repose only and the work of adhesion decreases by four orders of magnitude. $\varpi = 70 \pm 30$ mJ/m^2, for commercial and heat-treated tips only. The expected work of adhesion for two flat plates of silicon was $\varpi = 100$ mJ/m^2.

4.2.1.4. Uncorrected and corrected TND work of adhesion [mJ/m^2] versus radius [μm] results

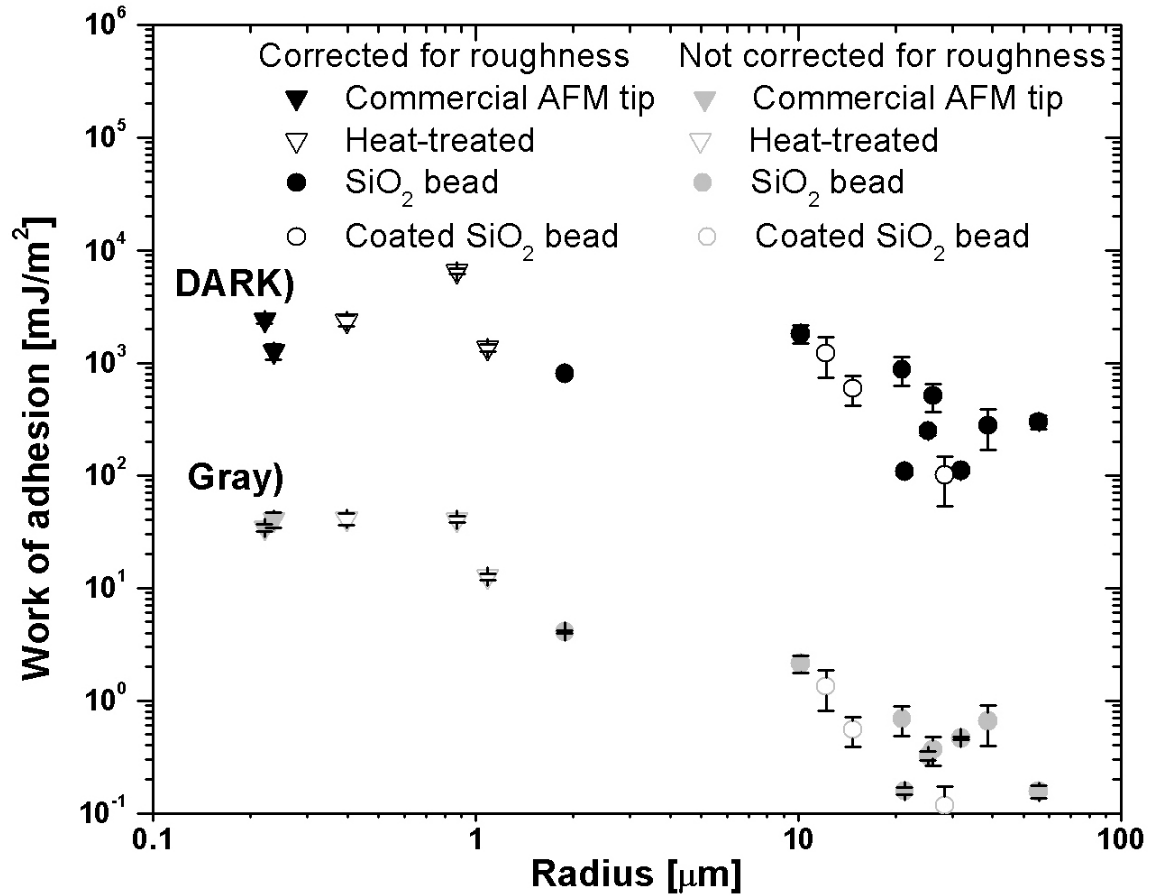

Figure 4.2.1.4-1. Work of adhesion versus radius for the treated no die-attach sample (TND). a)The data were corrected for angle of repose and surface roughness. b) The data were corrected for effects due to the angle of repose only and the work of adhesion decreases by four orders of magnitude. ϖ = 45 ± 16 mJ/m^2, for commercial and heat-treated tips only.

simplicity of the assumptions involved[69]. The number, size, and shape of the asperities within the contact area should be measured, but they were estimated to be equivalent to a single average asperity described by the RMS roughness of the AFM tip surface. The accuracy for the work of adhesion was calculated to be 15% and the scatter for each data point was measured to range from less than 1% to 50% (one standard deviation).

Lastly, the asperities of the rough tip that contact the sample might experience plastic deformation; however, the largest size radius that would be subject to plastic deformation at equilibrium contact can be estimated as[73]

$$R_{plastic} = 0.1926\varpi \frac{K^2}{Y^3} = 0.9 \text{ nm}, \tag{4.1}$$

where ϖ is the work of adhesion (100 mJ/m^2; the value for silicon), K is the reduced elastic modulus (127 GPa), and Y is the yield stress or yield strength (7 GPa)[17]. The predicted radius at which plastic deformation happens was much smaller than the smallest sized AFM tip (~ 200 nm), but smaller sized asperities were much closer to the predicted radius. Commercial and heat-treated AFM tips had roughnesses close to 0.9 nm. The surface roughnesses for the AFM tips were measured after the pull-off forces were measured.

4.2.2. The physics of contact

The nature of contact can be much more complicated than the simplified approach developed in this thesis. Nonetheless, the physics of contact can be understood within the boundaries of the experimental conditions for this study. For instance, both the tip and sample might be rough, so it is important to know how those roughnesses offset each other. If the surfaces were to interlock perfectly (commensurate), then it might make

sense to treat the two surfaces as smooth. If the surfaces were incommensurate, they would need to be treated as rough. Most likely, for random rough surfaces, it would be expected that they would be incommensurate.

Additionally, the measured pull-off (adhesion) forces are influenced by the types of materials that are in contact, which could influence the amount of adhesion between the surfaces. The material consistency of the tip might also play a role and so both the sample and tip would need to have well controlled material properties. A few other items that can influence the adhesion are plastic deformation of the asperities, the shape of the tip, charging between the tip and sample, and whether or not the entire surface area of the contacting surfaces are the same material.

We believe our system was stiff with relatively low work of adhesion (i.e. DMT regime). The separation between the tip and sample is assumed to be small compared to the radius of the tip. The pull-off force was not influenced, within experimental conditions, by relative humidity, rate of force curve acquisition, or load on the cantilever, but the surface roughness did influence the measured pull-off force.

The physics of contact can be analyzed easier with one more bold assumption. The assumption is that within the contact region of the tip and sample there are N asperities and each asperity contributes equally to the adhesive force. This assumption modifies Equation (2.16) so that it becomes (Figure 4.2.2-1 and Figure 4.2.2-2)

$$\left|F_{total}(R,R_a)\right| = 2\pi R\varpi\left[\left(\frac{(h+2R_a)h^3}{R(h+R_a)^3} - \frac{h}{R} + \frac{R_a}{R}\right)N + \frac{h^2}{(h+R_a)^2}\right], \tag{4.2}$$

where N is the number of asperities; assuming the asperities are all the same size, shape, and at the same height within the contact area. We assume for analysis purposes that the tip-sample interface is silicon.

To understand the contact, the adhesive force was plotted as a function of RMS roughness for two different cases. The first case varied the number of asperities (N = 10, 100, and 1000; Figure 4.2.2-1) on the tip, while the radius of the tip was held fixed at 2 μm. For the second case, the radius of the tip was varied (R = 0.02 μm, 0.2 μm, and 2 μm), while the number of asperities on the tip were fixed at 1000.

From Figure 4.2.2-1, the net influence on adhesion, as the number of asperities increases, is that the minimum interaction force increases and shifts to the left. From Figure 4.2.2-2, the net influence on adhesion, as the size of the tip increases, is that the minimum interaction force increases and shifts to the right. For each set of conditions (radius and number of asperities), there is a minimum in the adhesive force and that minimum (well) in the interaction force depends on the radius of the tip and the number of asperities on it. When the surface roughness is low, it is the size of the tip that determines the total interaction force. When the surface roughness is large, it is the number of asperities and their attraction to the sample which determines the total interaction force. Thus, it is seen that the physics dictates it is the competition between the attraction of the asperities to a sample surface and the influence they have on separating the tip and sample, which most influence adhesion of contact.

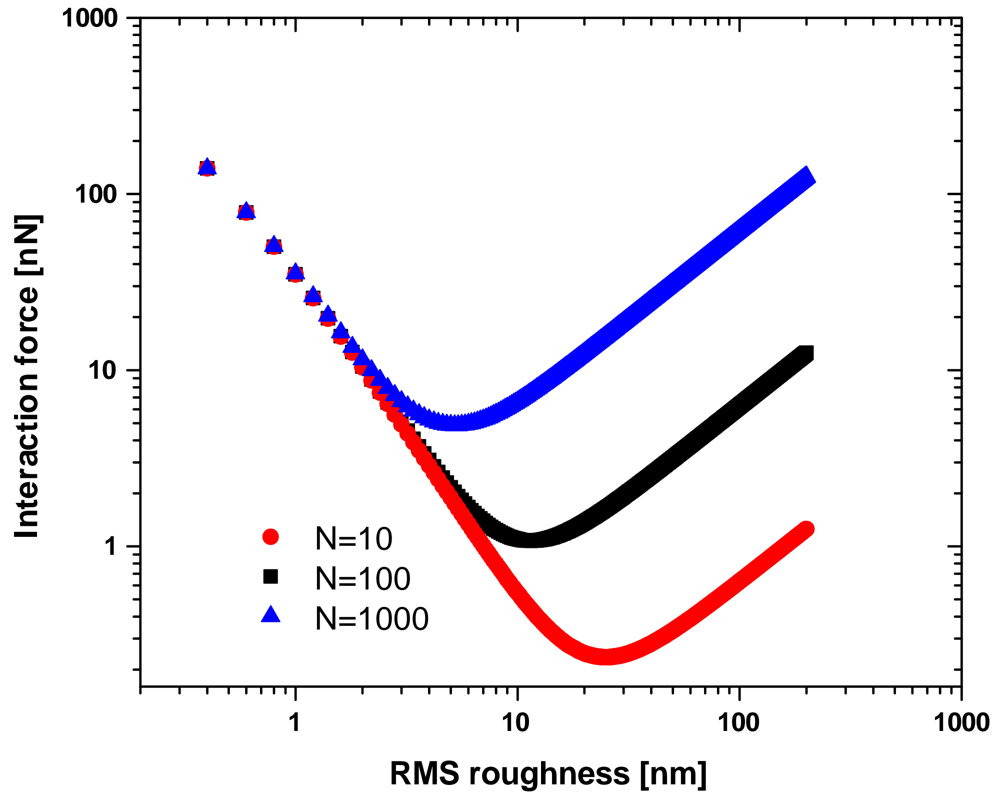

Figure 4.2.2-1. The interaction force as a function of RMS roughness. The value for the number of theoretical asperities was varied (see Equation (4.2) as N=10, 100, and 1000. R was 2 μm, ϖ = 100 mJ/m^2, and h = 0.165 nm. The minimum in the force of interaction is shifted upward and to the left as the number of asperities increases.

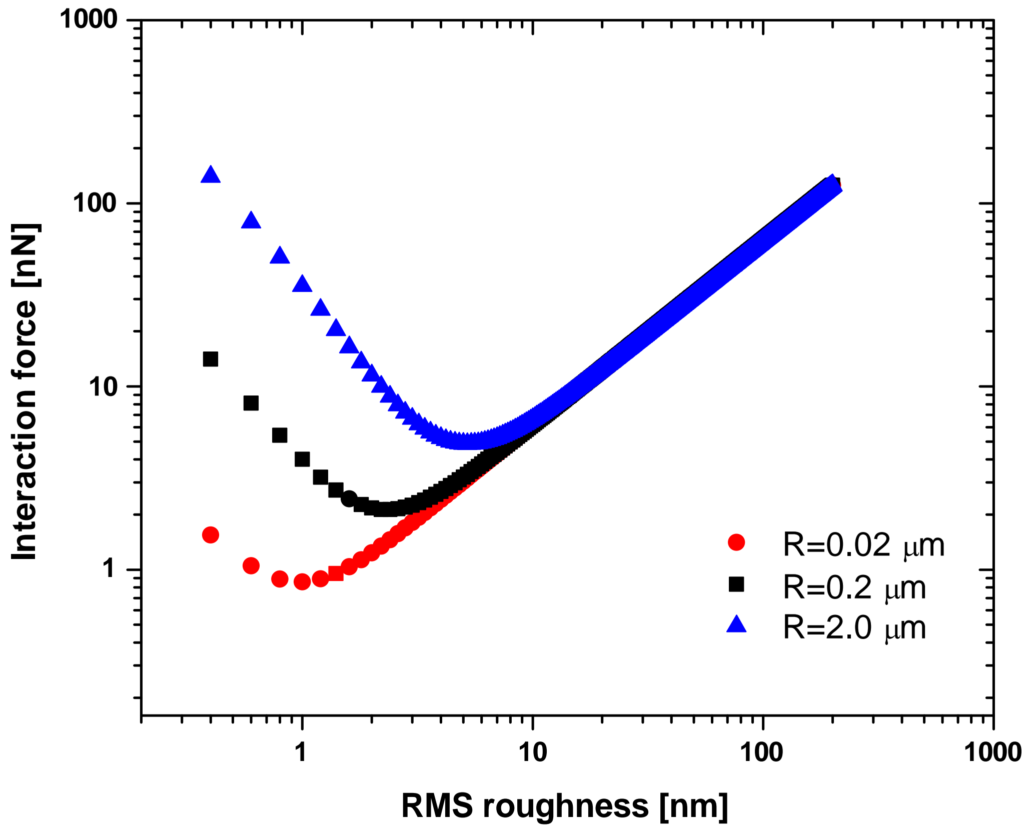

Figure 4.2.2-2. . The theoretical interaction force as a function of RMS roughness. The value for the radius of the tip was varied (see Equation (4.2)) as R = 0.02 μm, 0.2 μm, and 2.0 μm. N=1000, ϖ = 100 mJ/m^2, and h = 0.165 nm. The minimum in the force of interaction is shifted upward and to the right as the size of contact increases.

4.3. What might be the impact on other fields of science?

In 2004 M. Stolz et al.[74] reported that the stiffness of cartilage was two orders of magnitude different between a nanometer sized AFM tip and a micron sized AFM tip. The roughnesses of the tip and sample were not reported. Could the surface roughness explain the two-orders of magnitude difference between the stiffnesses? Although it is not possible to conclude that the roughness was the cause, it is a probable explanation for the change in stiffness.

In a 2005 news article in Nature, P. Patel-Predd[75] reported that H_2 is far more abundant than atomic hydrogen within dense dust clouds, from which stars form. The article also noted that current models could not explain the high temperature formation of H_2 within the clouds. However, a recent computer simulation run by E. Herbst and colleagues suggested that if the space dust were “bumpy” the atomic hydrogen would form at higher temperatures.

Although at this time it is not possible to conclude that our work and the above works are all interrelated, it is interesting to note that roughness in some form, whether from bumpy space dust or rough cartilage, might explain seemingly unexpected behavior.

CHAPTER 5

5. Conclusions

The spring constants of the cantilevers[26,28], the radii of the AFM tips[27], the surface roughnesses of both the samples and tips have been measured using procedures we have developed[69]. The AFM was calibrated to ensure proper conversion from the voltage squared to length squared domain for the power spectrum. We estimated the relative uncertainty in adhesive (pull-off) forces and radii to be 10%. We have developed procedures to measure the pull-off forces between (different types of tips with different surface roughnesses) AFM tips and sample surfaces (for two different types of surfaces).

Initially, we unexpectedly found that the pull-off force was independent of the radius of the tip. After applying a simple correction for the measured RMS roughness of the AFM tips, the correct functional dependence was returned for force upon radius. The values were still two orders of magnitude larger than expected, which was not surprising due to the assumption that the RMS roughness was set equal to a single average asperity. Despite this, the surface roughness correction has indicated it was the competition between the attraction of the asperities to the sample surface and the role they play in separating the tip-sample surface that most influence adhesion.

Now that we understand what caused the unexpected trend for pull-off force on radius, we can return to discussing the work of adhesion. Clearly, the initial assumption that measuring the work of adhesion would be a relatively quick and easy measurement was naive. This work has taught us that, in order to obtain quantitative work of adhesion values, measuring the radius of the tip, the deflection of the cantilever, and spring

constant of the cantilever were insufficient. The length of the cantilever and the height (or radius) of the AFM tip must be measured as well. The surface roughness correction to the adhesive force between surfaces seems to be explained in terms of summing up all the interactions for all the molecules interacting between the two surfaces.

The work presented here should progress the understanding of adhesion data lying between the macroscale and nanoscale. To our knowledge, no other experimental work has measured the adhesive (pull-off) forces between so many different types of tips and samples for the intermediate range between the macroscale and nanoscale.

CHAPTER 6

6. Future work

The following subsections are not meant to be all encompassing, but to convey the scope of work that can be done within this field of study. Some of the sections are posed as questions to answer, some are brief commentaries on issues with current methods, and some are brief suggestions for future work.

6.1. Measuring the roughness

Measuring the roughness can be difficult for the sizes of contacts that are typically used in the AFM. Since it was determined the asperities that interact within the contact area influence the pull-off forces, more work needs to be done to measure the actual contact area; a proper solution currently does not exist. One might measure the surface roughness of the AFM tip with the SEM, but that requires the AFM tip to be coated with a conducting material, which changes the surface chemistry. Additionally, SEM is a two-dimensional image, which means that three-dimensional roughness must be estimated. The plastic deformation was estimated to determine whether the surfaces were changed during contact, but the estimate requires prior knowledge of the work of adhesion, which is typically the quantity that is desired. To circumvent the circular argument, one might prepare the tip and sample so that the material consistency of both are well-known, but that still does not guarantee that surfaces have worn during contact. Ideally, one would prefer to measure the surface roughness of the sample and tip within the contact area

before and after an experiment in-situ, without changing the surface chemistry. A blind reconstruction technique might help, but after many decades the question, “What is the actual contact area and the roughness within it?” still persists.

6.2. Optimized surface roughness

Equation (4.2) hints that it might be possible to engineer surfaces so that a certain amount of adhesive force between surfaces could be obtained. This application would be most useful to the MEMS industry. MEMS manufacturers could minimize the adhesive force experienced between two surfaces by tailoring the surfaces so that their contact radii and number of asperities would produce the minimum amount of adhesive force.

6.3. Material properties

Since the material properties of the tip were not well-controlled, it would be interesting to repeat the experiment using AFM tips that have been made under similar conditions as the samples. The feasibility of producing these tips is not known.

6.4. AFM probe parameters

The length of the cantilever and height of the AFM tip might be measured using an SEM. The angle of repose was measured with a ruler, which resulted in large relative uncertainties. Perhaps another method could be developed, which measures the angle of repose more accurately. Future AFM’s might have additional functions incorporated into them, so that the AFM can be calibrated accurately and automatically. For instance, an

optoelectronic laser interferometric microscope (OELIM) might be combined with an AFM to produce very accurate measurements of the motion of the cantilever[76, 77].

6.5. Biomaterials

How does roughness influence the adhesion of biomaterials? There has been fast growth in the use of SPM techniques in the study of biomaterials, but not enough has been done to ensure that the SPM has been calibrated sufficiently to make quantitative comparisons between different biomaterial measurements; however, work is being done toward higher standards.

6.6. Experiments in liquid

How does the pull-off force on radius behave between rough surfaces in liquid? Is the roughness effectively smoothed out? The experiment described in this thesis could be repeated within a liquid cell to determine the influence of an intervening fluid and surface roughness in adhesion.

6.7. Heat-treated AFM tips

The tips for this study were grown under less than ideal conditions. The temperature controller was difficult to maintain within ± 20º C, there was no regulation of air-flow, and the furnace might have had contaminants. With the proper control and setup, uniform hemispherical tips could be made[67]. As a simple view to make tips of a given repeatable

size, the optimal temperature and time required to make a hemispherical tip would be needed.

6.8. NIST traceable measurements

Quantitative analysis with the AFM has been lacking, but to compare data between experiments, the AFM and its probe must be calibrated. Work is currently under way to develop cantilevers that can be traced to fundamental units. Ideally, all measurements from the AFM would be traceable to NIST standards, but there are many technical hurdles to overcome to get to that point. Much work is needed in developing traceable standards.

6.9. Device performance

We have measured unpatterned silicon die, but correlation to actual device performance was not known. Do various steps in the manufacturing process influence the resulting performance of MEMS or NEMS devices? The AFM could be employed as a diagnostic tool within the fabrication facility. The adhesive force could be measured at various points during manufacture as a trouble shooting or engineering tool. Which combination of processes produces the best performing devices?

6.10. Long term-surface stability

How does adhesion change over long periods of time? Initial work indicated that there was little change over a three month period in the work of adhesion values between

a commercial AFM tip and the untreated no die attach sample, but more work (longer studies) could be done.

Date	ϖ [mJ/m^2]
July 20, 2004	90 +/- 4
October 14, 2004	67 +/- 4
October 14, 2004	72 +/- 4
October 18, 2004	65 +/- 12

Table 6.10-1. The long-term stability of the UND sample. The work of adhesion was measured with a commercial AFM tip.

6.11. Material standards

Working in ambient (standard temperature and pressure) conditions can be difficult. The humidity is not usually well-controlled, and there are particulates in the air which can be adsorbed onto a surface. A surface with a work of adhesion that was well-known and stable over a long period of time (under normal room conditions) could be used as a standard. Once the AFM instrument and probe have been calibrated, the work of adhesion could be measured on the standard as a final check to see how well the instrument and probe have been calibrated. No known standards currently exist.

6.12. The future of MEMS and NEMS

Two major components of this thesis will be useful to the future of MEMS and NEMS devices. The first component is practical (an in-Fab stiction monitor; Apendix K) and the second is scientific, which could also lead to practical applications (e.g. surface roughness optimization).

The first component addresses a common problem for commercializing MEMS devices, which is stiction (but there are many other problems that occur during manufacturing and packaging). The work from this thesis will allow manufacturers the ability to monitor the adhesive properties all the way through the manufacturing process. The AFM is a common tool used in fabrication facilities and it could potentially take a more practical and productive role in the manufacturing of MEMS and NEMS devices. With the AFM, special structures are not required to measure the adhesion of surfaces. The roughness and adhesion between the AFM tip and a wafer could be monitored through the stages of manufacture, which could increase the probability of producing MEMS devices that fail during manufacture or use.

The second component addresses the understanding about the nature of contact. Understanding how surfaces adhere under realistic conditions is important from not only a scientific standpoint, but from a practical application standpoint as well. As part of the practical side, it is the calibration techniques that have been developed here that will allow measurements to be compared between different data sets. From the scientific point of view, it is the nature of contact that is interesting at the MEMS or NEMS level. Once devices have been shrunk to a small enough size, it is the surface interactions that dominate. For the future, it is the hope of this thesis to shed light on those surface interactions and how they relate to the size of the contact.

Appendix A. High resolution images

A.1 Abstract

Both the lateral and z-scanner ranges can be limited depending on the choice of scan parameters and image type (topography or topoX16). Knowledge of how these parameters might influence the surface roughness is important. The purpose of this section is to explain the lateral and z-scanner ranges[*], show what happens when the z-scanner range is exceeded, explain the difference between a topography image and topoX16, and show that the surface roughness is not influenced by high voltage, low voltage, the topography image, or the TopoX16 image.

A.2 DAC (Digital to Analog Converter)

With the closed-loop detection engaged, the lateral resolution of the Scan Master is limited to approximately 20 nm resolution*. The lateral resolution is given by the scan range divided by the number of pixels (e.g. 2 μm/256 pixels = 78.1 nm/pixel).

The z-scan range is limited by the DAC. For a topography image, the DAC acquires data at a rate of 20 bits/step and the voltage is represented as a 20-bit number with 2^{20} possible values. The z-scanner resolution for a two-micron image is limited to 6 $\mu m/2^{20}$ =.06 angstroms/step. However, the file format (*.hdf) for a topography image is not able to record 20-bits of data, so the 4 least significant digits are truncated. The topoX16 image acquires data at a rate of 16-bits/step, so the voltage is represented as a 16-bit number with 2^{16} possible values. In this case the z-scanner range is limited to 6 $\mu m/2^{16}$ =

[*] See Chapter 4 of Part II "Taking high-resolution topography images," of the AFM manual for more information.

0.9 angstroms/step. The difference between the two is that the topoX16 image acquires the 16 least significant digits, recovering the 4 dropped digits from the topography image. For the topoX16 image, the overall z-scanner range is reduced to 1/16th of what it would have been for a topography image. If a surface feature is outside the z-scanner range (called a wrap-around point) for a topoX16 image, the signal will change abruptly to the opposite limit causing a large step in the image, making interpretation difficult. To prevent this, the z-scanner can be moved up or down (a certain number of steps) until the surface feature lies within the z-scanner range. If adjusting the z-scanner does not work, then the sample surface may be too rough to image with topoX16.

Setting the hardware configuration to low-voltage mode and turning the scan master off will result in the minimum obtainable noise level. With the scan master off the scanner may drift, which will also influence the acquired image. If force curves were acquired after taking an image, it is possible that the location of contact of the AFM tip with the sample could drift outside the acquired image. Thus, no information about the interfacial roughness at the exact point of contact (for the force curve) is known.

A.3 Methodology

A silicon wafer (PC00108 #5 die B20) was imaged (with a normal AFM tip) with two different scan settings (high and low voltage mode) using two different types of images (topography and topoX16), in order to observe the influence of the scan settings on the surface roughness. Next, a silicon wafer that had surface features larger than the z-scanner range was imaged (high-and low-voltage modes) with a topoX16 image, which did show a wrap-around point.

A.4 Results

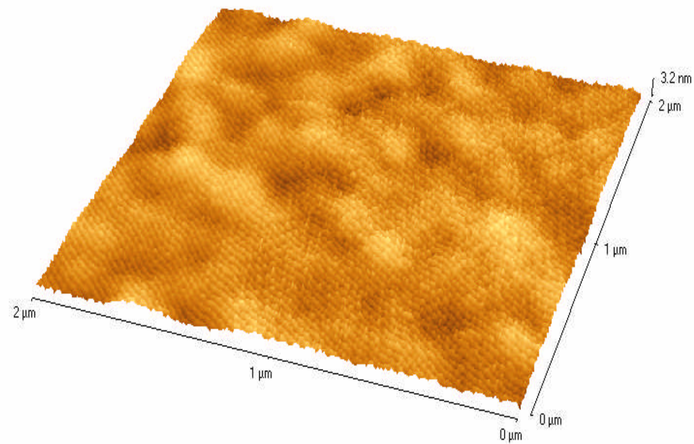

Figure A-1. Surface roughness measured on a silicon wafer (PC00108 #5 die B20). TopoX16 image. The parameters were set to low voltage, two-micron by two-micron, rate 1 Hz, set-point 50 nN, gain 0.1. The RMS roughness is 0.4 nm.

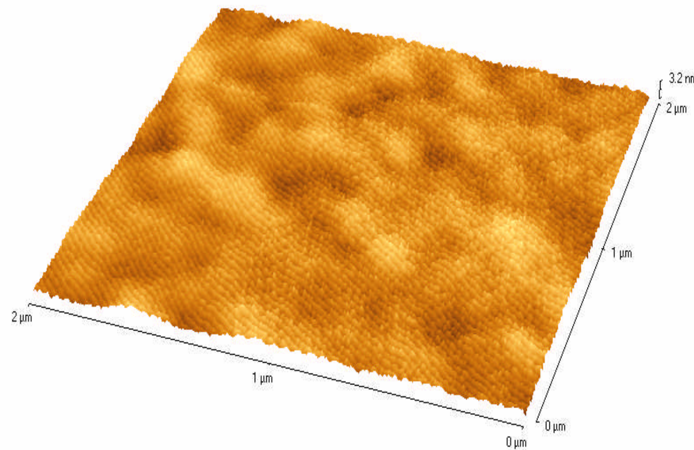

Figure A-2. Surface roughness measured on a silicon wafer (PC00108 #5 die B20). Topography image. The parameters were set to low voltage, two-micron by two-micron, rate 1 Hz, set-point 50 nN, gain 0.1. The RMS roughness is 0.4 nm.

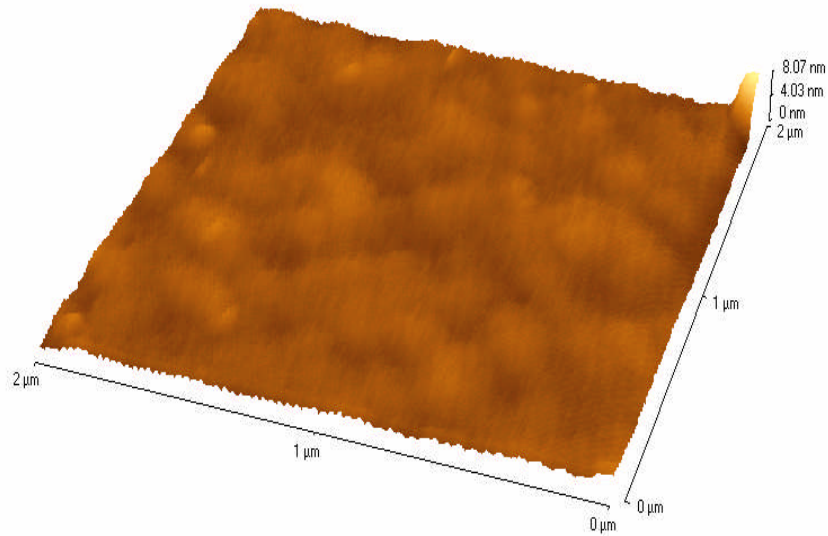

Figure A-3. Surface roughness measured on a silicon wafer (PC00108 #5 die B20). TopoX16 image. The parameters were set to high voltage, two-micron by two-micron, rate 2 Hz, set-point 50 nN, gain 0.1. The RMS roughness is 0.4 nm.

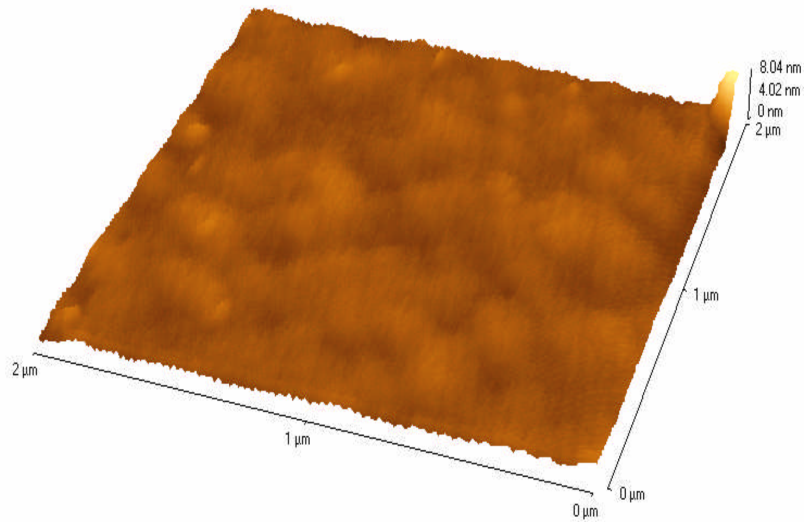

Figure A-4. Surface roughness measured on a silicon wafer (PC00108 #5 die B20). Topography image. The parameters were set to high voltage, two-micron by two-micron, rate 2 Hz, set-point 50 nN, gain 0.1. The RMS roughness is 0.4 nm.

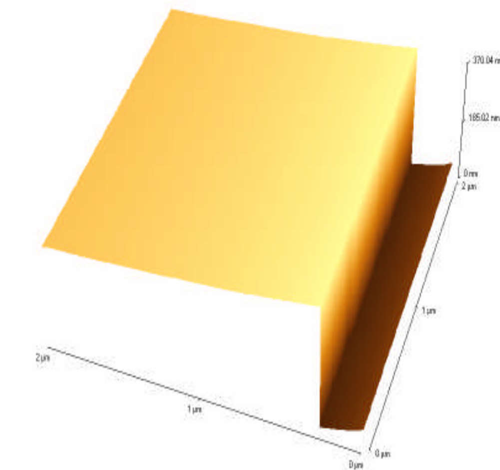

Figure A-5. Demonstration of the wrap-around point on a silicon wafer (PC00108 #5 die B20). TopoX16 image. The parameters were set to high voltage, two-micron by two-micron, rate 2 Hz, set-point 50 nN, gain 0.1. The above image illustrates what happens when the z-scanner scans surface features that are larger than the z-scanner range. If the features are not too large, moving the scanner up or down can solve this problem.

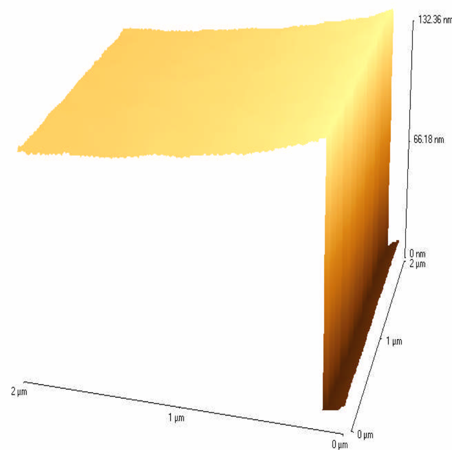

Figure A-6. Demonstration of the wrap-around point on a silicon wafer (PC00108 #5 die B20). TopoX16 image. The parameters were set to low voltage, two-micron by two-micron, rate 1 Hz, set-point 50 nN, gain 0.1. The above image illustrates what happens when the z-scanner scans surface features that are larger than the z-scanner range. If the features are not too large, moving the scanner up or down can solve this problem.

Figures A-1 through A-4 show that the measured surface roughness is not influenced (RMS roughness: 0.4 nm) by high-voltage mode, low-voltage mode, or by the type of topography image (topography and topoX16). The wrap-around point in a topoX16 (for high and low voltage) was demonstrated in Figure A-5 and Figure A-6.

A.5 Conclusion

The difference between a topography image and topoX16 has been explained. The surface roughness was measured on a silicon wafer and was not found to be different for the different types of data acquisition settings (high-voltage mode, low-voltage mode, topography image, and topoX16 image). Lastly, the wrap-around point was demonstrated for a topoX16 image (high and low voltage).

Appendix B. Measuring the AFM laser wavelength

B.1 Introduction

Electromagnetic radiation for the visible spectrum has wavelengths between 400 nm and 700 nm. Light is classified as monochromatic (single wave of electromagnetic radiation) or polychromatic (superposition of two or more waves of electromagnetic radiation). A light wave can be made to constructively or destructively interfere. A classical demonstration of light behaving as a wave is the double slit experiment performed by Thomas Young in 1802[1]. In this Appendix we show that the wavelength of light for the laser diode (Samsung SLD 67018250) of an AFM can be measured in two different ways. One way requires the manual set-up of a double-slit type experiment and the other way uses an Optical Spectrum Analyzer (OSA) to measure the wavelength of light. The latter of the two methods is more accurate, but it is useful to show that reasonably accurate values can be obtained with relatively simple measurements.

In order to observe fringe contrast from constructive interference, light must be coherent temporally and spatially. The temporal coherence is related to the wavelength (λ) and the linewidth ($\Delta\lambda$). The divergence (how quickly the light spreads out) is

$$\theta \sim \frac{\lambda}{D}, \qquad \text{B.1.}$$

where λ is the wavelength (670 nm as reported by the manufacturer) and D (~ 4.3 mm as reported by the manufacturer) is the diameter of the aperture for a laser diode. The spatial coherence is

---

[1] F. L. Pedrotti and L. S. Pedrotti, *Introduction to optics*, **2nd** edition (Prentice Hall, New Jersey, 1993), Vol. **1**, Chap. 10 + 12, p.205.

$$l_s = \frac{r\lambda}{s} \sim \frac{\lambda}{\theta}, \quad \text{B.2.}$$

where r is the distance between the aperture of the laser diode and the diffraction grating, and s is the diameter of the aperture. Therefore, for our laser diode the spatial coherence is 4.3 mm. If a grating with 80 lines per mm is used, the distance between the laser diode aperture and the grating should be

$$r = \frac{s l_s}{\lambda} = \frac{\left(\frac{1}{80}\text{ mm}\right)4.3\text{ mm}}{670\text{ nm}} \sim 0.085\text{ m} = 8.5\text{ cm}. \quad \text{B.3.}$$

Typically, the distance from the laser diode is much further than 8.5 cm. The light must be made coherent before being diffracted by the grating to achieve optimal fringe contrast. This can be done by placing a pinhole or slit in front of the diffraction grating. The pinhole acts as a point source causing the light to propagate outwards as spatially coherent spherical waves. The spatial coherence must be equal to or greater than the spacing between lines on the grating (1/80 mm) for good spatial contrast. If we assume the diameter of our pinhole is 10 mm, then the distance from the source (pinhole) to the grating should be

$$r = \frac{s l_s}{\lambda} = \frac{10\text{ mm}\left(\frac{1}{80}\text{ mm}\right)}{670\text{ nm}} \sim 0.187\text{ m} = 18.7\text{ cm}. \quad \text{B.4.}$$

This distance can be accommodated by an optical rail. If a lens is used to collimate the light (make the rays of light parallel to the axis of propagation) after the pinhole, then the distance between the lens and the diffraction grating is not as crucial.

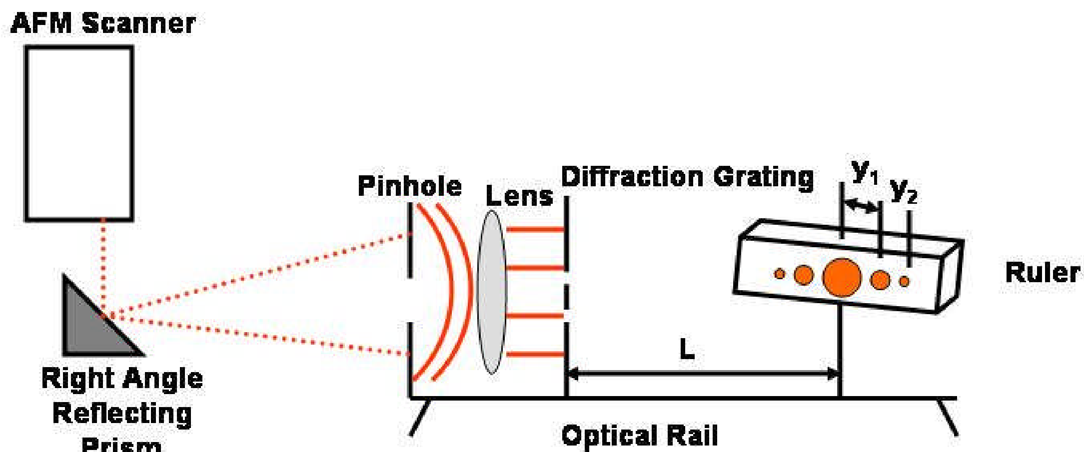

Figure B-1. Experimental setup to measure the laser wavelength of the AFM scanner.

B.2 Measuring the wavelength of the laser using an optical rail

The following is a list of steps required to complete the measurement of the wavelength of the laser light coming from the AFM scanner head (see Figure B-1).

1. Place a right angle mirror underneath the AFM scanner so that the laser diode beam propagates freely to the pinhole on the optical rail.
2. Make sure the laser beam is centered on the pinhole. Note, the pinhole diameter can be increased or decreased depending on the desired distance between the pinhole and the grating.

3. Autocollimate the lens (set the distance between the lens and slit to be the focal length of the lens).
    a. Place a lens after the pinhole.
    b. Place a mirror after the lens.
    c. Fix the mirror. Angle the mirror so that an image of the pinhole is formed next to the actual pinhole.
    d. Move the lens back and forth until the image of the pinhole is minimized.
    e. Fix the lens in place. The light rays coming from the lens are now parallel.
4. Be sure to record the position of the grating with the ruler (L); (should be ~ 20 cm in order to minimize error) on the optical rail.
5. Measure the distance between the first and second maxima to the nearest 0.5 mm. The distance between peaks (y_n) should be ~ 1 cm in order to minimize the error. (Suggestion: measure the diameter of the maxima and then calculate y based on the center of those maxima.)
6. Calculate the average wavelength and standard deviation. The left and right side (the two first-order maxima) should yield the same wavelength within a few percent.

$$\lambda = \frac{y_n d}{nL}, \qquad \text{B. 5.}$$

d is the spacing between lines on the grating (1/80 mm), and n is the order of the bright spots. The zero-order is the middle peak or the brightest peak. The relative uncertainty is

$$\% \frac{\delta\lambda}{\lambda} = \left\{ \sqrt{\left(\frac{\sigma_{y_n}}{y_n}\right)^2 + \left(\frac{\sigma_L}{L}\right)^2 + \left(\frac{\sigma_d}{d}\right)^2} \right\} 100. \qquad \text{B. 6.}$$

$\sigma_{yn} = \sigma_L = 0.5$ mm, $\sigma_d << \sigma_{yn}$, $\sigma_d \sim 0$, and y and L are your measured values. This value should be low (< 4 %). The wavelength measured for our instrument (Autoprobe M5), with this method, was 655 ± 19 nm (for one standard deviation).

B.3 Measuring the wavelength of the laser using an OSA (Optical Spectrum Analyzer)

The second method uses an OSA[2] to measure the wavelength of light. The OSA (Ando AQ6317B; see Figure B-2) is located in Dr. Quimby's IPG Photonics Optics Laboratory (IPG Lab). In order to measure the wavelength of the laser, the light must make it to the IPG Lab. The school network has a fiber optic backbone, so the fiber optic port in our lab (see Figure B-3) was connected to the fiber optic port in Dr. Quimby's laboratory. After the connection, only a few steps are required to set up. Additionally, the accuracy of the measurement is high, making it the preferred method for measuring the wavelength.

First, a right angle reflecting prism reflects the light from the positioning laser and sends it propagating perpendicularly to the scanner head. The light is then collected by a lens and then focused onto the end of a multimode fiber (FC connector; see Figure B-4). Next, the (LC connector) other end of the fiber was connected to the fiber optic network port OH 009 B # 5 in the AFM Lab. An identical fiber was connected to the IPG Photonics Lab network port OH 205 D # 5. Despite the huge dispersion in the fiber, the output is visible in the IPG Photonics Lab (if the lights are low). When the light is visible there should be a sufficient amount to measure the wavelength of the laser with the OSA.

[2] http://cp.literature.agilent.com/litweb/pdf/5980-0746E.pdf

The FC connector is then connected to the FC port of the OSA and authorized personnel (Rodica Martin) then measures the wavelength of the light.

For the OSA method, the measured wavelength was 664.83 ± 1.93 nm (one standard deviation). The measured value of the wavelength using the OSA was within the relative uncertainty for the simple method, indicating that simple methods can be used to measure the wavelength of light reasonably well.

Figure B-2. Ando AQ6317B Optical Spectrum Analyzer located in the IPG Photonics Laboratory.

Figure B-3. Network port in the AFM Lab. A similar port is located in the IPG Photonics Laboratory.

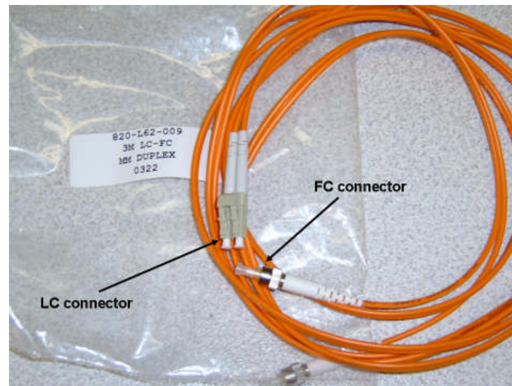

Figure B-4. FC to LC fiber connector. The laser light from the AFM is coupled into the FC connector and the LC connector is connected to the network port. An identical fiber is located in the IPG Photonics Laboratory, except that the FC connector is connected to the OSA.

Appendix C. Calibrating the z-scanner displacement

C.1 Instructions

The following list is a set of instructions that will allow a user to calibrate the z-scanner movement. See Chapter Six of Part II, "Scanner Calibration," of the AFM manual for further information.

1) Load a cantilever with a reflective coating (preferably rectangular). Align the AFM laser half on and half off the cantilever.
2) Place the AFM cantilever close to a reflective surface (like the AFM stage), but far enough away so the surface does not interact with the cantilever.
3) Go to set-up menu and choose input configuration. Choose z-detector and CN7.
4) Turn off the z-servo.
5) Go to the tools menu.
6) Choose x-y mode.
7) Set the range -1 to 1.
8) Click sweep. Stop after one sweep.
9) Change the x-axis to z-detector.
10) Click in the CN7 window.
11) Choose view one.
12) Choose measure.
13) Click sweep; allow a decent force curve to acquire (see Figure C-1).
14) Stop sweep.
15) Left click on the first peak of the interference pattern.

16) Right click on the last peak of the interference pattern. Be careful not to move the mouse!

17) Read the dx value in nm and divide by the number of peaks minus 1 (this gives the actual measurement for the peak to peak interference distance).

18) Go back to spectroscopy mode.

19) Turn z-servo back on.

20) Calibrate the z-scanner movement using Chapter Six Part II, "Scanner Calibration," of the AFM manual.

21) Repeat steps 1-20 until the measured peak to peak separation matches the actual calculated peak to peak separation within a few percent. $\Delta z_p = \frac{\lambda}{1+\cos(2\theta)}$ where Δz_p is the distance between interference peaks, λ (664.83 nm) is the wavelength of the laser, and θ (10.739 °, for the unmounted cantilever holder[1]) is the angle of repose of the AFM cantilever. The distance between peaks should be 344.37 nm ± 3%[2].

[1] A mounted cantilever has at a different angle of repose. Additionally, each mounted cantilever might have a different angle of repose.
[2] See G. A. Matei, E. J. Thoreson, J. R. Pratt et al., "Precision and accuracy of thermal calibration for atomic-force microscopy cantilevers," (submitted 2005).

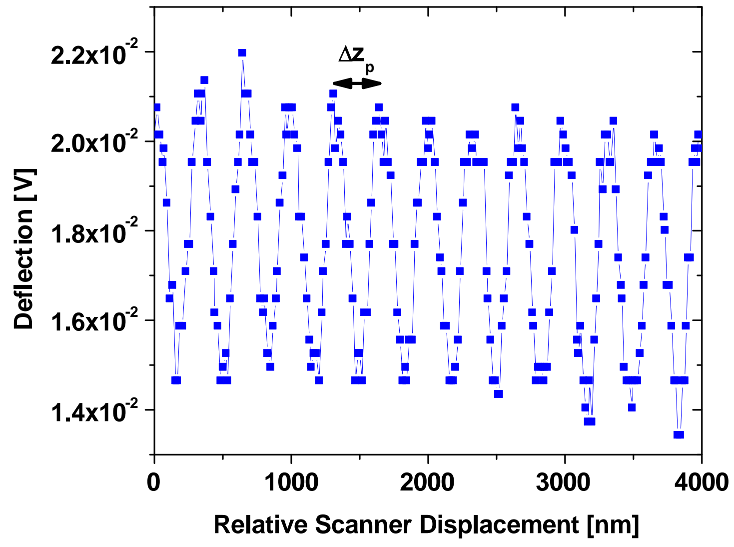

Figure C-1. Example interference pattern.

Appendix D. Calibrating the spring constant

D.1 Instructions

The following list is a set of instructions that will allow a user to calibrate the spring constant for an AFM cantilever using a thermal method[1]. The needed equipment for measuring the spring constant is the AFM, the oscilloscope, and the data acquisition computer. The needed software for measuring the spring constant is Agilent Data Capture, HP VEE, and MathCad.

1) Measure the resonant frequency with the AFM in the NCM mode.
2) Go to set-up menu and choose input configuration. Choose z-detector and CN7.
3) Come into contact with a stiff surface (e.g. AFM stage or mica).
4) Turn off the z-servo and Scan-master.
5) Go to the tools menu.
6) Choose x-y mode.
7) Set the range from -0.5 to 1.
8) Click sweep. Stop after one sweep.
9) Change the x-axis (horizontal axis) to z-detector.
10) Click in the CN7 window.
11) Choose view one.
12) Choose measure.
13) Click sweep; allow a decent force curve to be acquired.

[1] See N. A. Burnham, X. Chen, C. S. Hodges et al., "Comparison of calibration methods for atomic-force microscopy cantilevers," Nanotechnology 14 (1), 1-6 (2003) and G. A. Matei, E. J. Thoreson, J. R. Pratt et al., "Precision and accuracy of thermal calibration for atomic-force microscopy cantilevers," (submitted 2005).

14) Stop sweep.

15) Left click at the intersection of the first horizontal grid and the linear portion of the force curve.

16) Right click at the intersection of the last horizontal grid and the linear portion of the force curve. Be careful not to move the mouse!

17) Read the dx and dy values in nm/V; this gives the conversion factor $\Delta z/\Delta v$.

18) Go back to spectroscopy mode.

19) Turn z-servo and Scan-master back on.

20) Raise the z-scanner all the way.

21) Push the Scan Off button and turn the z-servo off.

22) Log into the data acquisition computer and turn the oscilloscope on (be sure one end of the the raw A-B BNC cable is plugged into channel 1 of the oscilloscope and the other end is plugged into the raw A-B BNC on the signal access module).

23) Open: set-oscope.vee, read_ave.vee, fit.mcad, and Data Capture for 54620 series oscilloscopes.

24) Wait a couple of minutes for the cantilever to come into thermal equilibrium with its surroundings.

25) Run set-oscope.vee; wait for acquisition to finish.

26) Run the Data Capture for 54620 series oscilloscopes by choosing the instrument and all data.

27) Wait for the data acquisition to finish.

28) Save file as waveform#.csv in c:\userprograms\Thermal\Inutilink\

29) Go to read_ave.vee and enter the conversion factor $\Delta z/\Delta v$.

30) Start read_ave.vee. Make sure the correct calibration value is listed (should be: ϕ= 10.739, λ= 664.83 nm, Auto-probe Correction = 1.23); be sure to choose the waveform#.csv you just saved.

31) Name the result bee.txt and place it in: c:\userprograms\thermal\data

32) Go to fit.mcad.

33) Enter the frequency you measured with the AFM.

34) Click on C:= (read command) and push F9; this updates the file.

35) Scroll down; you should see an hourglass telling you that the software is thinking. Within a minute or two; it should find a solution. Please see nonlinear fitting function routine genfit within MathCad for more information on the guess values.

Be sure to record:

A, the 1/f noise [nm^2Hz]

B, the white noise [nm^2],

$<x(\nu_k)^2>$, the mean-squared amplitude at kinetic resonance [nm^2],

Q, the quality factor,

ν_k, the kinetic resonance [Hz],

k_t, the thermal spring constant [N/m].

Appendix E. NIST comparison

E.1 Instructions

The following list is a set of instructions that were used to determine the spring constant of an unknown cantilever by pushing against a piezoresistive cantilever calibrated at NIST using an Electrostatic Force Balance (EFB)[1]. Steps 19 and 20 were performed in order to compare spring constant measurements between the NIST cantilever and the thermal method[2].

1. Load the unknown tipless cantilever in the AFM.
2. Place the piezoresistive cantilever on the x-y stage.
3. Make sure that the long axis of the unknown cantilever and the piezoresistive cantilever are parallel to each other.
4. Tape the microscope slide that the piezoresistive cantilever is on to the x-y stage. (* CAUTION: the electrical leads to the piezoresistive leads can come into contact with the cantilever. If they do, they will break the cantilever.*)
5. Tape the electrical leads to the x-y stage. (*NOTE: when taping it is best to fold one side of the tape over on itself, that way the tape can be easily removed.*)
6. Attach the multimeter leads to the leads from the piezoresistive cantilever.
7. Tape the multimeter leads to the x-y stage.
8. Make sure the multimeter is set to record resistance and not voltage.

---

[1] J. R. Pratt, D. T. Smith, D. B. Newell et al., "Progress toward Système International d'Unités traceable force metrology for nanomechanics," J. Mater. Res. **19** (1), 366-379 (2004).
[2] G. A. Matei, E. J. Thoreson, J. R. Pratt et al., "Precision and accuracy of thermal calibration for atomic-force microscopy cantilevers," (submitted 2005).

9. Bring the unknown cantilever into contact with the piezoresistive cantilever. (*NOTE: be sure to stop scanning and translate the z-scanner down until contact is made with the piezoresistive cantilever.*)
10. Make sure the filtered A-B is the input CN7 on the back of the interface module (AUX 2 IN).
11. Choose to acquire the z-detector and CN7 signals.
12. Once in contact, turn the z-detector off and open x-y mode from the AFM software. (Leave Scan Master ON)
13. Set the oscilloscope to fifty seconds total time.
14. Choose twenty seconds for the time base (in x-y mode) and click run.
15. Simultaneously push start on the HP VEE program NIST_2.vee. (*NOTE: there will be a finite time required for you to get to the data acquisition computer. All that is needed are the total changes in resistance and voltage, so as long as the pull-off portions of the curves are not truncated, good data will be acquired.*)
16. As soon as the HP VEE program is done, push stop on both the x-y mode and oscilloscope.
17. Open the Agilent software (Data Capture for 54620 series oscilloscopes), and acquire the data from the oscilloscope.
18. Use a spreadsheet to determine the minimum and maximum change for both the resistance and the voltage.
19. Without changing the position of the laser (on the unknown cantilever) disengage the piezoresistive cantilever, reset to nominal conditions, and bring the cantilever

into contact with mica or the AFM stage. (*CAUTION: do not change the laser position or turn the head off; doing so will require you to restart the method.*)

20. Follow steps 1-20 of Appendix D (Calibrating the spring constant).

Appendix F. Calibrating the radius of an AFM tip

F.1 Calibrating the radius of a normal AFM tip

The following list is a set of instructions that will allow a user to calibrate the radius of a normal AFM tip using a parabolic fitting function.

1) See AFM Instrument Lab #4 on tip calibration and use the delta function grating (TGT01).
2) Once an image has been acquired, Open ParabolaRadiusCalibration.xls and follow the instructions.

F.2 Calibrating the radius of a SiO_2 bead

The following list is a set of instructions that will allow a user to calibrate the radius of beads attached to tipless AFM cantilevers.

1) Acquire a topography image on a sharp step. To start, the scan range should be approximately the expected radius for the bead and the step height should be smaller than the diameter of the bead.
2) Open the file in SPMLab.
3) Choose file and export the image as *.txt.

Open http://www.wpi.edu/Academics/Depts/Physics/AFM/Downloads/SphereRadiusCalibration.xls . Follow the instructions.

Appendix G. Making large AFM tips

G.1 Bead attachment to tipless AFM cantilever

Commercial AFM tips with larger AFM tips are not available, so they must be made. One way larger AFM tips were made was by attaching a silicon dioxide sphere to a tipless AFM cantilever. Spheres 6 μm in radii and larger are made in our laboratory by attaching them to tipless cantilevers[27]. Spheres as small as one to two microns can be attached, but need to be sent out, since we do not have the equipment to attach the smaller spheres; however, when the small spheres are attached for us, the beads are attached with a proprietary glue and its influence on contact is unknown.

To attach the 6 μm and larger in radii spheres in our lab, an optical microscope, micropositioner, UV light cure glue, UV light source, two tapered pipettes (these are made with a PUL-1 pipette puller from World Precision Instruments), and two syringes with needles are needed (Appendix F and reference 27). The bead (sphere) and glue applicator must be assembled by inserting a syringe into the larger end of one applicator. A small amount of UV cure glue is placed at the interface between the pipette and syringe. Placing the pipette, syringe and UV cure glue under the UV light source for approximately 15 minutes causes the glue to harden. Two of these must be made to attach a silicon dioxide sphere (bead) to a tipless cantilever. One of them is used for the application of the UV cure glue to the tipless cantilever (glue applicator) and the other is used to place the sphere (bead) on the tipless cantilever (bead applicator).

Once the two applicators are ready for use, the syringe pump is placed in a three-axis micropositioner (by Stoelting). The syringe with applicator is screwed onto the syringe pump, and the micropositioner is then used to dip the applicator in UV glue (Norland Optical Adhesive NOA - 81). A single, small drop of glue is placed at the end of a tipless AFM cantilever with the aid of the stereo microscope (Olympus SZ60). A very small amount of glue should be used, less than the diameter of the sphere, otherwise capillary action will coat the entire bead with glue.

Before bead placement, a clean (new) syringe / applicator is screwed to the syringe pump. The tip of the applicator is brought down into contact with a clean spot on the AFM chip, where it is rubbed against the silicon, causing an electrostatic charging of the applicator. The electrostatically charged applicator is positioned over a bead on a microscope slide, and since the electrostatic attraction of the bead to the applicator is stronger than the bead's adherence to the glass slide, the bead is picked up. Subsequently, the applicator with bead is placed over the cantilever with glue. When the bead is brought close to the glue, the liquid-bead interaction dominates the bead and applicator interaction, causing the bead to be pulled from the applicator to the liquid. Finally, the cantilever with bead is placed under a short-wave UV light source (UVP, Inc. UVSL-14P) for about 15-20 minutes.

Two steps should be performed before using the sphere. First, make sure that it has adhered to the cantilever by trying to pry it off with the applicator used to place the bead, being careful not to pry too hard or the cantilever might break. Second, look at the side profile of the bead through the stereo microscope to verify that capillary action did not

cause the glue to coat the sphere. Should the bead-cantilever ensemble pass this examination it is ready for radius characterization (Appendix F).

G.2 Instructions for bead attachment

The following list is a set of instructions that will allow a user to attach beads (12 µm in diameter and larger) to tipless AFM cantilevers.

1) Use a pipette puller (PUL-1 from World Precision Instruments) to create the glue and bead applicators. The applicators look like glass syringes. One is used to pick up and place the bead and the other is used to place the glue.
2) Insert a syringe into the larger diameter end of the applicator and glue in place (Usually UV glue, but any glue that keeps the syringe and applicator connected will work).
3) Connect the syringe / applicator to a syringe pump.
4) Place syringe / pump into a three-axis micropositioner (by Stoelting).
5) The micropositioner is then used to dip the applicator in UV glue (Norland Optical Adhesive NOA - 81). A single, small drop is placed at the end of a tipless AFM cantilever with the aid of the stereo microscope (Olympus SZ60). A very small amount of glue should be used (less than the diameter of the sphere); otherwise capillary action will coat the entire bead with glue.
6) Get a new clean syringe / applicator.
7) The tip of the applicator is brought down into contact with a clean spot on the AFM chip, where it is rubbed against the silicon causing an electrostatic charging of the applicator. The electrostatically charged applicator is positioned over a

bead on a microscope slide, and since the electrostatic attraction of the bead to the applicator is stronger than the bead's adherence to the glass slide, the bead is picked up. Subsequently, the applicator with bead is placed over the cantilever with glue. When the bead is brought close to the glue, the liquid bead interaction dominates the bead / applicator interaction causing the bead to be pulled from the applicator to the liquid.

8) Finally, the cantilever with bead is placed under a short-wave UV light source (UVP, Inc. UVSL-14P) for about 15-20 minutes.
9) Ensure that the bead has adhered to the cantilever by trying to pry it off with the applicator used to place the bead, being careful not to pry too hard or the cantilever might break.
10) Look at the side profile of the bead through the stereo microscope to verify that capillary action did not cause the glue to coat the sphere.
11) The tipless AFM cantilever with attached bead is now ready to use.

G.3 Heat-treated AFM tips

Attaching SiO_2 beads to AFM tipless cantilevers was relatively easy and convenient. However, the SiO_2 material consistency of the tips may not be the same as the AFM tip itself or the sample surface being studied. To resolve this issue, larger AFM tips can also be made by heat treating them according to reference 66. Our lab does not have the same tools as listed in reference 66, so we adapted available existing equipment to produce a similar result-AFM tips that are relatively smooth with a hemispherical shape.

To make heat-treated AFM tips, one needs a furnace, uncoated commercial AFM cantilevers, ceramic crucible, high temperature tongs, high temperature thermometer, and a sputter-coater. Ideally the commercial AFM tips should be heated to 1200° C, like reference 66. The tube furnace that was available only heated to about 900° C safely. So our AFM tips were baked at a temperature as high as possible, but for a longer period of time. Using this method tips as large as 2 micron in diameter were made.

G.4 Instructions for heat-treated tips

1) Collect ceramic crucible, uncoated commercial AFM tips, thermometer, and tube furnace (Thanks to Dr. Germano Iannacchione) in one location (Thanks to Dr. George D. J. Phillies).
2) Place the uncoated AFM cantilever, with the tip facing upward, in the crucible.
3) Place the crucible with cantilever in the furnace, so the tip is facing upward.
4) Place the high temperature probe into the midsection of the tube furnace.
5) Turn on the furnace so that it will produce a temperature as high as possible within ± 20° C.
6) Once the furnace has reached temperature, leave the tip in the furnace for the desired length of time. The final size of the tip is dependent on many factors (the time it takes to get to temperature, the starting environmental conditions, and the final temperature of the furnace to name a few contributing factors). The tips were left in the furnce for a single to multiple days. The longer the time period the larger the tip.
7) Once the tip has baked, turn the furnace off and wait for it to cool down.

8) Once the tip has cooled down, remove it from the furnace and take it to the sputter coater. The backside of the cantilever must be coated with aluminum. This allows the backside of the cantilever to be reflective enough to produce an appropriate A-B signal.

9) Coat the backside of the cantilever with aluminum (Thanks to Dr. Rafael Garcia). Once this is done, the tip should be ready to use. Be sure to check that the spring constant (Appendix D) and radius of the tip (Appendix F) are within the expected range.

Appendix H. Measuring the AFM tip roughness

H.1 Introduction

This section supplements section 3.2.5 (Surface roughness calibration) by describing other methods and techniques that were attempted in order to measure the surface roughness of AFM tips. A normal AFM tip (SiO_x) was expected to make a single-point contact with the sample surface. Attached beads to tipless AFM cantilevers or grown SiO_2 tips were expected to have roughness and contact the sample surface at multiple points. When the roughness was measured on a sample surface with a normal AFM tip, the measured roughness was expected to result from the sample. If the tip and sample were both rough, the measured roughness would be an interfacial roughness. Ideally, one would like to measure the surface roughness of both the tip and sample before and after an experiment, but that was not practical.

An ideal way to measure the surface roughness (for very small dimensions) of the tip was to image the tip with a sharp peak. A delta-function grating was a series of sharp peaks that was used to measure the radius of a normal AFM tip, but it could be used to measure the roughness of the tip by measuring a small area on the normal AFM tip. The RMS (Root Mean Square) roughness would be obtained from that small area. For beads attached to tipless cantilevers, the spacing between the peaks on the delta function (otherwise known as pitch) was too small to measure the roughness accurately.

To understand the influence of the surface roughness on the work of adhesion, it was necessary to measure both the AFM tip and sample roughness. This appendix briefly describes many different techniques used, while trying to find a method for surface

roughness characterization for all the different types of tips (normal, heat-treated, and attached beads).

H.2 Methods for measuring the surface roughness of AFM tips

H.1.1 Polystyrene sphere

An image of the tip was taken after fixing a polystyrene bead to a surface and imaging the bead with a larger AFM tip[1] in an attempt to determine the surface roughness of the larger tip. To fix the bead to a substrate, a solution of polystyrene beads and water was placed on a mica surface and the water was allowed to evaporate. The beads were found to adhere well to the surface (via AFM imaging in contact mode). The mechanism causing the adherence was not known, but was assumed to be either van der Waals or capillary forces.

Despite good adherence to the substrate, problems arose that made the method impractical. One problem was that we had no way of knowing the diameter and surface roughness of the imaged bead. The diameter might be measured by assuming the bead was spherical and imaging the bead attached to a substrate with a normal AFM tip; the resulting maximum height change would be the diameter of the sphere, but we still would not know the surface roughness. One might assume that a larger sized tip would have a larger roughness and, so, imaging the bead might be appropriate. But, the size of the bead attached to the substrate would determine the size of tip that could be imaged making the method difficult to apply uniformly. Additionally, the fixed bead could slide or roll

[1] Y. Li and S. M. Lindsay, "Polystyrene Latex particles as a calibration for the atomic force microscope," Rev. Sci. Instrum **62** (11), 2630 (1991).

underneath the larger AFM tip, causing errors in the estimation of the tip radius or the surface roughness.

H.1.2 Oxide growth

When a conducting probe is placed in an AFM and when a DC voltage is applied between the tip and sample, the silicon surface will oxidize where the tip is located[2]. The localized oxidization produces a spike, which can be used to determine the roughness of a larger AFM tip. The disadvantage of this method is that it requires additional equipment. Even after modifying the AFM, many questions would need to be answered before useful spikes are made. How tall can a spike be made? What is the optimum voltage? What is the optimum dwell time at one location needed to grow a spike? How sharp is the spike? How would the spike be located on the sample surface, so that one could return repetitively to the location of the spike? How stiff are the spikes? Can an array of spikes be made in a reasonable amount of time? Our AFM is capable of such a modification, but requires additional equipment, making the technique not feasible.

H.1.3 Nanografting

A monolayer of molecules could be deposited on a surface and sections of the molecules are grafted away with an AFM tip. The resulting structure could be used to characterize the surface roughness of the tip[3].

If the molecules are grafted by the AFM tip, then the characterizer structure will most likely deform when imaged by an AFM tip. The benefit of the method depends on

---

[2] E. S. Snow and P. M. Campbell, "Fabrication of Si nanostructures with an atomic force microscope," Appl. Phys. Lett. **64** (15), 1932-1934 (1994).

[3] S. Xu, N. A. Amro, and G.-Y. Liu, "Characterization of AFM tips using nanografting," Applied Surface Science **175-176**, 649-655 (2001).

the stiffness of the molecules that are deposited. If the AFM tip used to graft the molecules is very stiff and the AFM tip that is measured is very compliant, the method might be of some use when studying compliant cantilevers, but only for compliant cantilevers. Assuming that the AFM tip is compliant, many questions still need to be answered. What molecules should be used? Where do you get the molecules? How are they deposited? How stable are the molecules (are they permanently adhered)? Do the molecules have a "shelf-life?" This method was deemed not feasible, since it needs much development.

H.1.4 FIB (Focused Ion Beam)

Silicon or another appropriate surface can be selectively etched by a FIB (Focused Ion Beam)[4]. The advantage of this method is that a single spike can be made. The disadvantage is that the single spike is difficult to locate each time a tip is measured. An array of spikes can be made, but the process is time consuming and requires access to an FIB. We did not have access and thus this method was not feasible.

H.1.5 Direct imaging of an attached bead

A stiff cantilever with a normal AFM tip was flipped over, known as the flipped over tip (FOT) method, and secured to a substrate. The FOT was placed onto the AFM stage. A tipless cantilever with attached bead was placed in contact with the FOT and the RMS roughness was measured. It was relatively easy to image the surface for a large bead (~60 μm diameter). Imaging smaller size beads was more difficult, because the tip

---

[4] M. Fukuda, S. Tomimatsu, K. Nakamura et al., "A new FIB fabrication method for micropillar specimens for three-dimensional observation using scanning transmission electron microscopy," Journal of Electron Microscopy **53** (5), 479-483 (2004).

can slide off the bead. The disadvantage to the FOT method is that the actual contact area might not be imaged, which means the roughness must be assumed uniform over the entire tip.

H.1.6 Step

A step was imaged while in contact with a bead attached to a tipless AFM cantilever as described in Thoreson et. al. (2004)[5]. Instead of averaging all scan-lines (as was done with the radius calibration), the radius was measured for several individual scan-lines and the standard deviation for the radius was calculated. The standard deviation was expected to correlate with the surface roughness of the bead. The standard deviation, although small, was much larger than expected (nanometers). Upon reflection, it was realized that the relative uncertainty for measuring the bead radius was 9%, which means we would not be able to measure a dimensional size smaller than 9% of the total radius of the AFM tip. For a 12-micron bead, this translates into 1.2 microns of uncertainty, which was much larger than the expected surface roughness. Thus, the method was deemed unsatisfactory.

H.1.7 Polymer spike

Another possible method for measuring the surface roughness was to put a normal AFM cantilever flipped over in a container of known volume. Fill the container with some polymer (polystyrene) and heat the polymer until it melts so that part of the

---

[5] E. J. Thoreson and N. A. Burnham, "Standard-deviation minimization for calibrating the radii of spheres attached to atomic force microscope cantilevers," Review of Scientific Instruments **75** (5), 1359-1362 (2004).

cantilever tip is covered, which leaves a spike of the right height and diameter. Several issues came up when using this solution. The first was that the volume of the container must be known to a few microns in each dimension. Second, the spike will not be perpendicular to the bead because the cantilever bends to match surface tension. Third, the amount of mass required to fill the container was very small (μg), much smaller than what can be measured easily. Even if we could increase the container diameter, you would need a diameter of about one meter to have an amount of mass that could be measured.

The molecular weight (MW) of the polymer determines the viscosity of the polymer melt. Different molecular weights were used to determine the most appropriate viscosity for cantilever placement. The cantilever and powder form of the polymer was placed into a small reservoir, and the reservoir was heated until the polymer melted. If the correct amount of powder was placed into the reservoir, the cantilever would be covered for all but a small portion of the tip. Alternatively, the powder could be melted and the cantilever pushed into the melt, covering all but a small portion of the tip. A MW of 190,000 was too thick (i.e. the viscosity was high). A MW of 19,300 was about right, but the correct amount of powder was difficult to dispense. A MW =1110 had the right flow rate, but charging was observed for force curves between the SiO_2 bead and polystyrene.

Another attempt was to melt the polymer and then sprinkle tiny beads (3-10 μm) into the melt. Once the melted polymer cooled, beads would be protruding from the sample. There were four main issues with this method. The first was that the cooled solid surface was not entirely flat. The second was that there would be no way to place the AFM scanner at the same spike or bead. The third was that the sprinkled beads tended to

clump. The fourth was that we could only use AFM tips that were much larger than the protruding beads. Thus, the method was deemed not feasible.

H.1.8 SEM (Scanning Electron Microscope)

A SEM (Scanning Electron Microscope) shoots electrons (called primary electrons) at a sample surface. The electrons are created by either thermal or field emission. Some of the electrons are absorbed, some bump around in the material like a plinko game board (a vertical grid of spikes; to play the game a disk is dropped at the top of the board and the disk bounces around until it comes to rest in a container at the bottom. The contestant wins a dollar amount equal to the amount written on the container), and some are backscattered. Those that are absorbed are re-emitted as secondary electrons, Auger electrons, and x-rays. The SEM measures the intensity of the secondary electrons ejected from the material, which depends on the surface features. By scanning either the scanning gun or sample and recording the intensity at each x and y position, an image is created. In essence, the image is a shadow of the surface. The benefits are that high-resolution images are obtained. The disadvantage is that the sample must be a conducting material, able to withstand high vacuum, and high-energy bombardment from electrons. Another disadvantage to using SEM to characterize the tip is that it does not give three-dimensional information about the tip and the surface chemistry of the tip.

H.1.9 TEM (Transmission Electron Microscope)

TEM is similar to SEM; an electron beam is produced and shot at a sample surface in high vacuum. The differences are that the sample must also be thin and the electrons

transmitted through the sample are recorded (as opposed to the secondary electrons from the SEM). Some electrons pass through the sample surface and some are diffracted depending on the crystal structure of the sample and the angle of observation. TEM is capable of characterizing the tip, but it is impractical for in-situ use.

H.1.10 Blind reconstruction

Blind reconstruction requires the topography of one surface to be known and is very sensitive to noise or rough surfaces[6]. The method has been used for characterization of the tip radius, but it requires much software development to incorporate into our images; it is unclear how quantitative values for surface roughness might be obtained.

H.1.11 Dip pen nanolithography (DPN)

The DPN works by dipping a pen (tip of a cantilever) into an ink reservoir of molecules (e.g. solution of DNA) and then dragging the tip along a surface. A line of molecules is left along the tip’s path and by repeating the process three-dimensional structures are made. For DPN, a small amount of glue can be placed on a surface (light curing glue)[7]. Small rods or spikes can be placed in the glue. Once the glue has been cured, the remaining spike can be used for tip characterization. The method requires a DPN machine and a significant amount of development, which makes it impractical for near term use.

---

6 J. S. Villarrubia, in *Applied scanning probe methods* (Springer, Berlin ; New York, 2004), pp. 147-167.

7 H. Zhang, K.-B. Lee, Z. Li et al., "Biofunctionalized Nanoarrays of Inorganic Structures Prepared by Dip-Pen Nanolithography," Nanotechnology **14**, 1113-1117 (2003).

H.1.12 Field emission displays

Field emission displays might have components that have spikes of the right size to use for tip characterization integrated into them. The main issue is that the spikes (emitters) are not accessible to AFM. A circular field guide about two-micron in diameter blocks access to the spikes[8].

H.1.13 Plasma screen TV

A plasma TV might have integrated components of the right size for tip characterization integrated into them. After disassembling a broken Plasma TV[9], no sharp peaks or any harvestable items were found. Plasma TVs work similar to fluorescent light bulbs[10].

H.1.14 Custom design of TGT01

One can design a custom grating that has spikes placed at the correct pitch (spacing between spikes). The rough estimate for cost of making a custom characterizer was $3,000-$4,000. Mikromasch makes them, but we would have had to buy half a wafer and lead times were long. Mikromasch has discontinued the use of the standard delta-function grating, which can increase the cost of a custom delta-function grating.

---

[8] B. Q. Wei, R. Vajtai, and P. M. Ajayan, "Reliability and current carrying capacity of carbon nanotubes," Appl. Phys. Lett. **79** (8), 1172-1174 (2001).
[9] Thanks to Gary Guidi from Hi Rez Services for the broken plasma TV.
[10] http://electronics.howstuffworks.com/plasma-display.htm

H.1.15 Carbon nanohorns

Carbon nanohorns are carbon nanotubes orientated perpendicular to a substrate. If they were ordered or spaced far enough apart, they might be used as tip characterizers. Information from the manufacturer indicates that the carbon nanotubes form 80-100 nm islands (or clumps) that are randomly deposited. The method was deemed not useable, because the spacing between islands was uncertain.

H.1.16 UV (Ultraviolet) glue

A small drop of glue might be made to form a small spike. A glue drop (UV glue) was placed on a substrate. By inserting and retracting a small sharp object into the drop a meniscus was formed between the tip and drop. Curing the glue while the meniscus formed would result in the formation of a small spike. The disadvantage to the UV glue was that the small sharp object would need to be the same size as the resulting spike (~ 10 nm), and the glue would need to cure quick enough to freeze the meniscus in place.

H.1.17 Whiskers

A common failure mode when soldering electronic devices are the formation of very thin strands (whisker) of solder[11]. However, the whiskers do form spikes that might be used for tip characterization. The whiskers are randomly orientated and not perpendicular to the sample surface, making them unusable as a tip characterizer.

---

[11] Y. Zhang, C. Xu, C. Fan et al., "Tin whisker growth and prevention," J. Surface Mount Technology, 1-9 (2000).

Appendix I. Report on the work of adhesion between six-inch wafers and an AFM tip.

Table of Contents

Appendix I. Report on the work of adhesion between six-inch wafers and an AFM tip. I-1
I.1 Introduction....I-4
I.2 Experimental methods I-5
I.3 Results....I-7
I.4 Roughness....I-11
I.5 Work of adhesion....I-12
I.6 Tip cleaning I-12
I.7 Discussion....I-12
I.7.1 Roughness....I-12
I.7.2 Work of adhesion....I-13
I.7.3 Tip cleaning I-14
I.8 Future work....I-15
I.8.1 Surface charge I-15
I.8.2 Normal AFM tip radius I-16
I.8.3 AFM tip roughness I-16

List of Figures

Figure I-1.Treated polysilicon. RMS roughness is 13.6 nm. The average work of adhesion is 0.46 ± 0.41 mJ/m^2. ....I-7
Figure I-2. Untreated polysilicon. RMS roughness is 3.1 nm. The average work of adhesion is 4.0 ± 3.3 mJ/m^2. ....I-7
Figure I-3. Treated silicon nitride. RMS roughness is 0.6 nm. The average work of adhesion is 160 ± 20 mJ/m^2. ....I-8
Figure I-4. Untreated silicon nitride. RMS roughness is 0.8 nm. The average work of adhesion is 17 ± 9 mJ/m^2. ....I-8
Figure I-5. Treated Silicon. RMS roughness is 0.4 nm. The average work of adhesion is 13 ± 2 mJ/m^2. ....I-9
Figure I-6. Untreated silicon. RMS roughness is 0.5 nm. The average work of adhesion is 6.1 ± 2.7 mJ/m^2. ....I-9
Figure I-7. Untreated silicon no die-attach that has been roughened with steel wool. ...I-10
Figure I-8. Work of adhesion as function of RMS roughness for six different substrates. A different tip was used for the polysilicon (treated and untreated) samples (radii listed in the figure key). The silicon wafers had the lowest overall roughness. The treated silicon nitride had the highest work of adhesion followed by the treated

silicon rerun. The uncertainty in the measured RMS value is expected to be 0.2 nm for one standard deviation. The y-error bars represent one standard deviation……I-11

Abstract

The work of adhesion was measured between a normal AFM (Atomic-Force Microscope) tip (SiO_2) and silicon wafers. The radius of the tip and spring constant of the cantilever were measured before each experiment. Two sample variables were explored: three crystal systems (silicon, polysilicon, silicon nitride), and two surface conditions (native oxide with and without a few angstroms of vapor-deposited diphenylsiloxane), which resulted in a total of six different kinds of samples. The treated polysilicon surface had the highest roughness and the lowest work of adhesion. The treated silicon nitride surface displayed the highest work of adhesion. The high variability in the work of adhesion on the six samples might be caused by a combination of local variations in the contact roughness, both the RMS (Root Mean Square) roughness and the mean distance between asperities, and the surface condition (at contact). The surface condition could result from either charging or local variations in surface chemistry.

I.1 Introduction

Magnetic, gravitational, strong nuclear, and weak nuclear forces are assumed negligible compared with short to long-range (0.2 nm to 100 nm) electric forces. The three most pertinent electric forces (between an AFM tip and sample) are the meniscus, patch charge, and van der Waals force. The meniscus force (water on the sample or tip surface) can be long-ranged and should result in a measured work of adhesion equal to 142 mJ/m^2. The van der Waals interaction is short-ranged (the magnitude will drop a million times at a separation distance of 100 nm) and usually dominates when a water layer is absent (at a distance of < 10 nm) or very thin (monolayer). The patch force can be repulsive in the intermediate range and attractive in the short-range.

The amount or degree to which a surface makes contact with the AFM tip can strongly affect the measured work of adhesion. The work of adhesion should be constant for a given set of materials. If the contact area was estimated to be larger than the actual size, the measured work of adhesion would be lower than expected. The converse of this is also true.

In addition, the local surface condition at contact can influence the work of adhesion. The local surface chemistry is affected by absorbed species, defects, and preparation. Charging can also occur between insulators (dielectrics) via charge exchange[1] caused by local differences in the work functions of the tip and sample. Adsorbed species will tend to lower the work of adhesion and charging can increase the work of adhesion. This report will delineate data obtained by measuring the work of adhesion on six different types of samples, single silicon, polysilicon, and silicon nitride (with and without a few angstroms of vapor deposited diphenylsiloxane).

I.2 Experimental methods

The radius of the tip (a parabolic fit to a linescan of a topography image of a delta function and AFM tip) and spring constant of the cantilever were measured before each experiment. Since a topography image for an AFM is a dilation between the sample surface and the inverted shape of the tip, the measured radius of the tip will be larger than the actual tip radius. For SiO_2 beads attached to tipless cantilevers, the accuracy, in the measurement of the radius, is measured to be 9%. For normal AFM tips, the accuracy, in the measurement of the radius, is assumed to be 9%.

Two sample variables were explored: three crystal systems (silicon, polysilicon, and silicon nitride), and two surface conditions (native oxide with and without a few angstroms of vapor-deposited diphenylsiloxane), which resulted in a total of six different kinds of samples. The wafers were placed on the AFM stage and imaged with a normal AFM tip (SiO_2). The RMS roughness was measured from a two-micron by two-micron image of the wafer. Sixteen approach and retraction force curves were obtained across a two-micron square section of the wafer. Each of the sixteen force curves was an average of sixteen force curves at a single location. The pull-off force (F_{po}) was measured from the sixteen force curves and was used to determine the work of adhesion (ϖ) at each point.

$$F_{po} = -k\,\delta z \,, \qquad \text{I.1}$$

where k is the spring constant and δz is the deflection of the AFM cantilever.

$$\varpi = \frac{-F_{po}}{2\pi R}, \qquad \text{I.2}$$

where F_{po} is the pull-off force and R is the AFM tip radius. The final reported value for the work of adhesion was the average of the sixteen different locations. In between

measuring each type of wafer, an attempt to clean the AFM tip was made by irradiating it for two minutes with UV (UltraViolet) light (253.7 nm). The UV light causes a photochemical reaction, which removes hydrocarbons from the sample surface and breaks them down. An alpha (positively charged) particle source was placed near the AFM tip, to neutralize negative charges ejected during the irradiation and to reduce negative charge build-up on the AFM tip.

To test the influence of tip cleaning, the work of adhesion was measured on silicon (untreated and treated) die, which were removed from their LCC (Leadless Ceramic Chip Carrier) packages with silver-glass die-attachments, after the tip was cleaned. To test the influence of roughness, the work of adhesion was measured on silicon (untreated) die, which were removed from their LCC packages with no die-attachments, before and after the silicon die was roughened with steel wool.

All measurements (see Figure I-8) were made at a relative humidity of 51.9 ± 2.7% and temperature of 22.9 ± 0.5 °C. The accuracy for the work of adhesion is 13% (10% accuracy for pull-off force and 9% accuracy for tip radius) by the method of quadratures (the measurement errors are independent and random). All reported relative and absolute uncertainties are given as one standard deviation of the scatter in the measurements.

I.3 Results

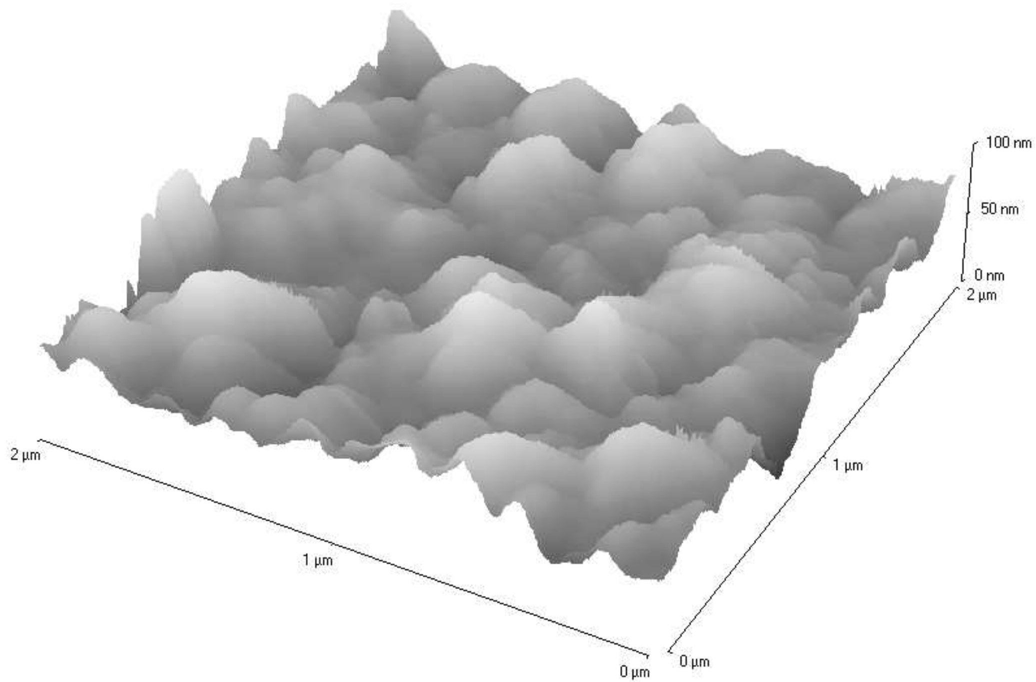

Figure I-1.Treated polysilicon. RMS roughness is 13.6 nm. The average work of adhesion is 0.46 ± 0.41 mJ/m^2.

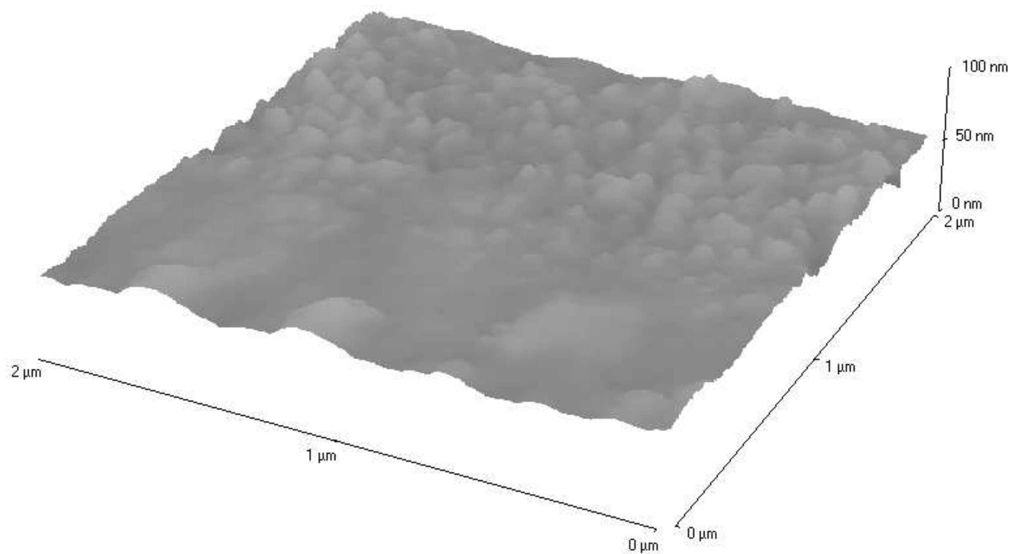

Figure I-2. Untreated polysilicon. RMS roughness is 3.1 nm. The average work of adhesion is 4.0 ± 3.3 mJ/m^2.

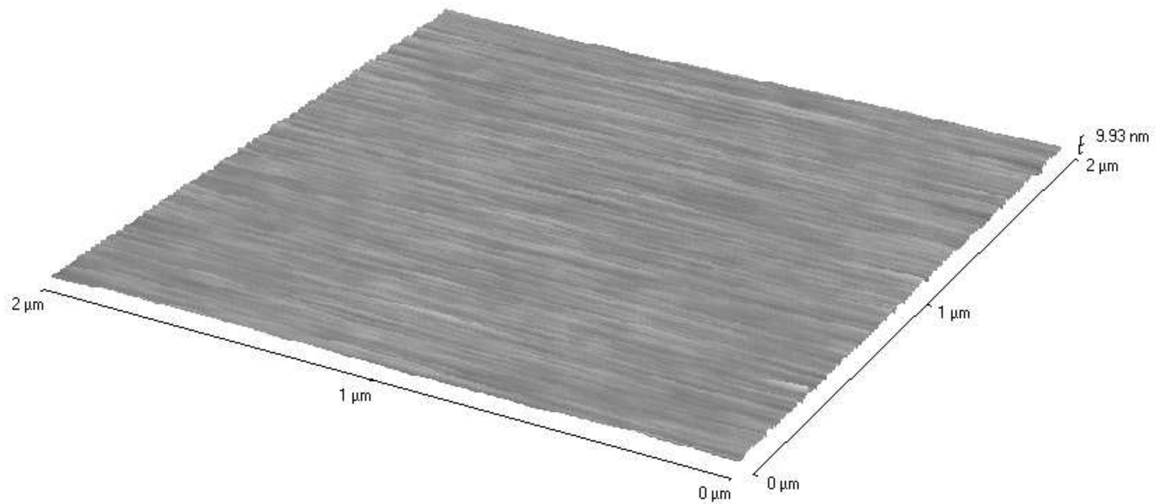

Figure I-3. Treated silicon nitride. RMS roughness is 0.6 nm. The average work of adhesion is 160 ± 20 mJ/m^2.

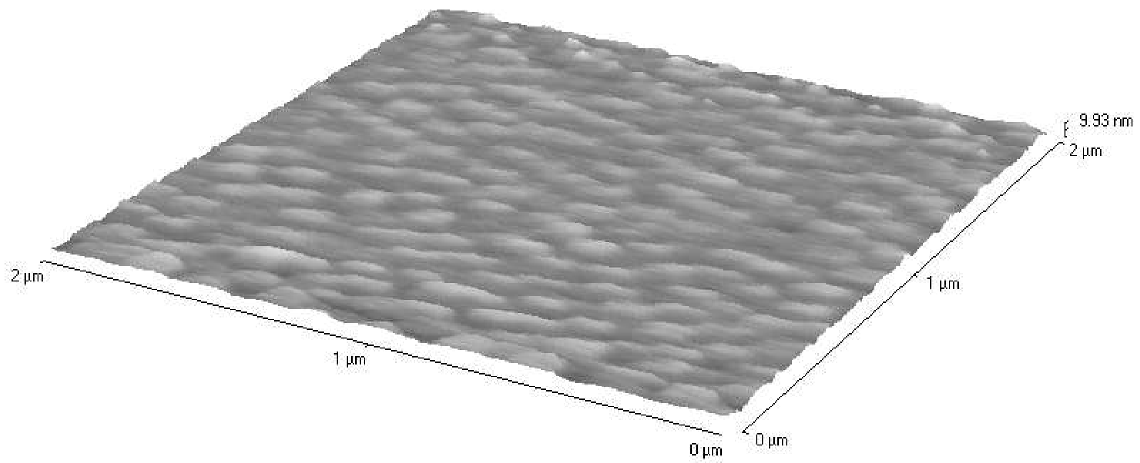

Figure I-4. Untreated silicon nitride. RMS roughness is 0.8 nm. The average work of adhesion is 17 ± 9 mJ/m^2.

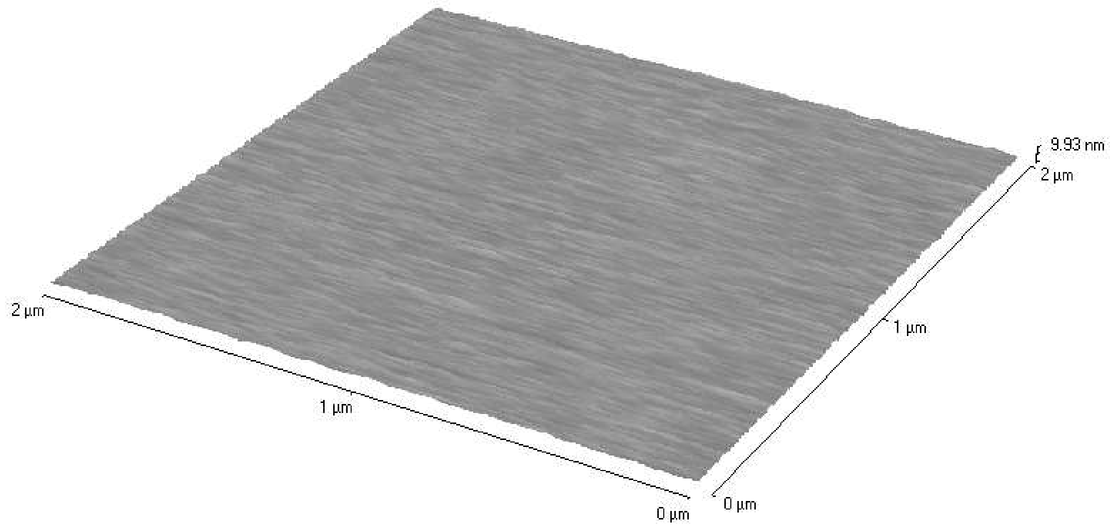

Figure I-5. Treated Silicon. RMS roughness is 0.4 nm. The average work of adhesion is 13 ± 2 mJ/m^2.

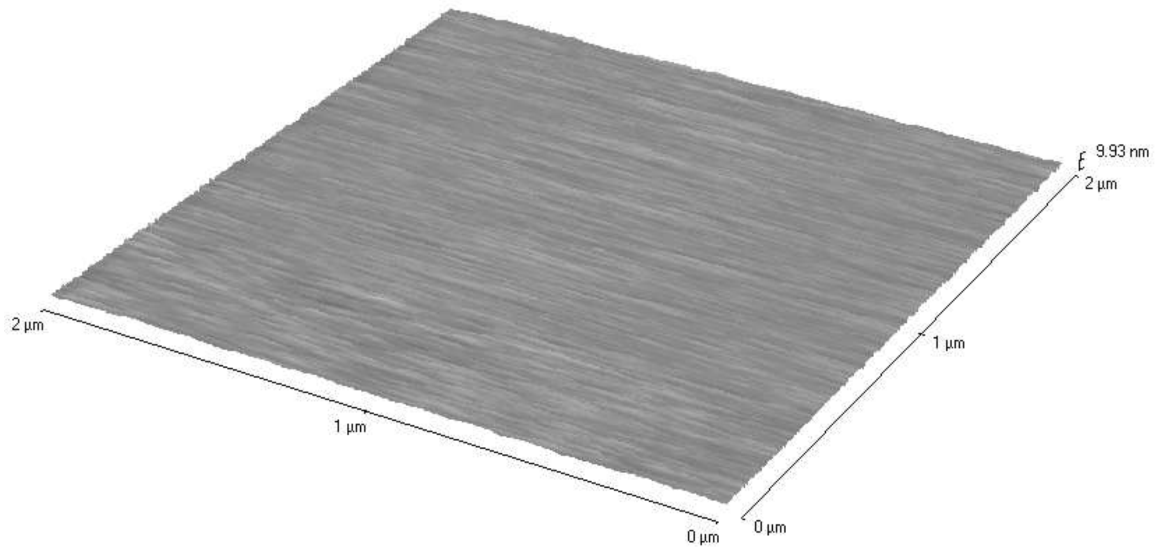

Figure I-6. Untreated silicon. RMS roughness is 0.5 nm. The average work of adhesion is 6.1 ± 2.7 mJ/m^2.

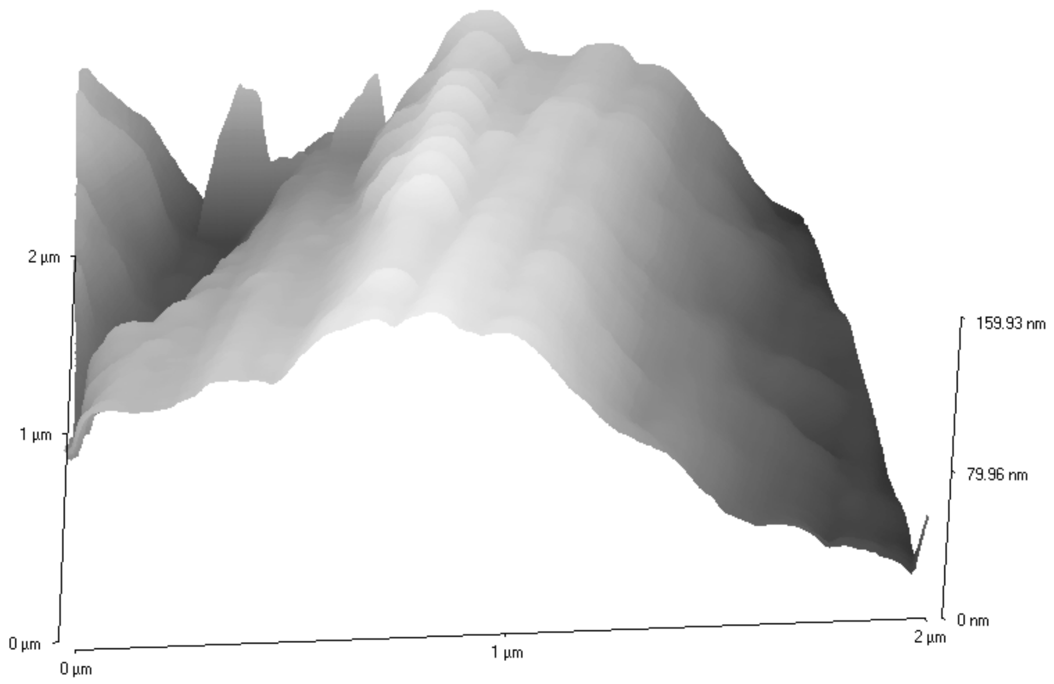

Figure I-7. Untreated silicon no die-attach that has been roughened with steel wool.

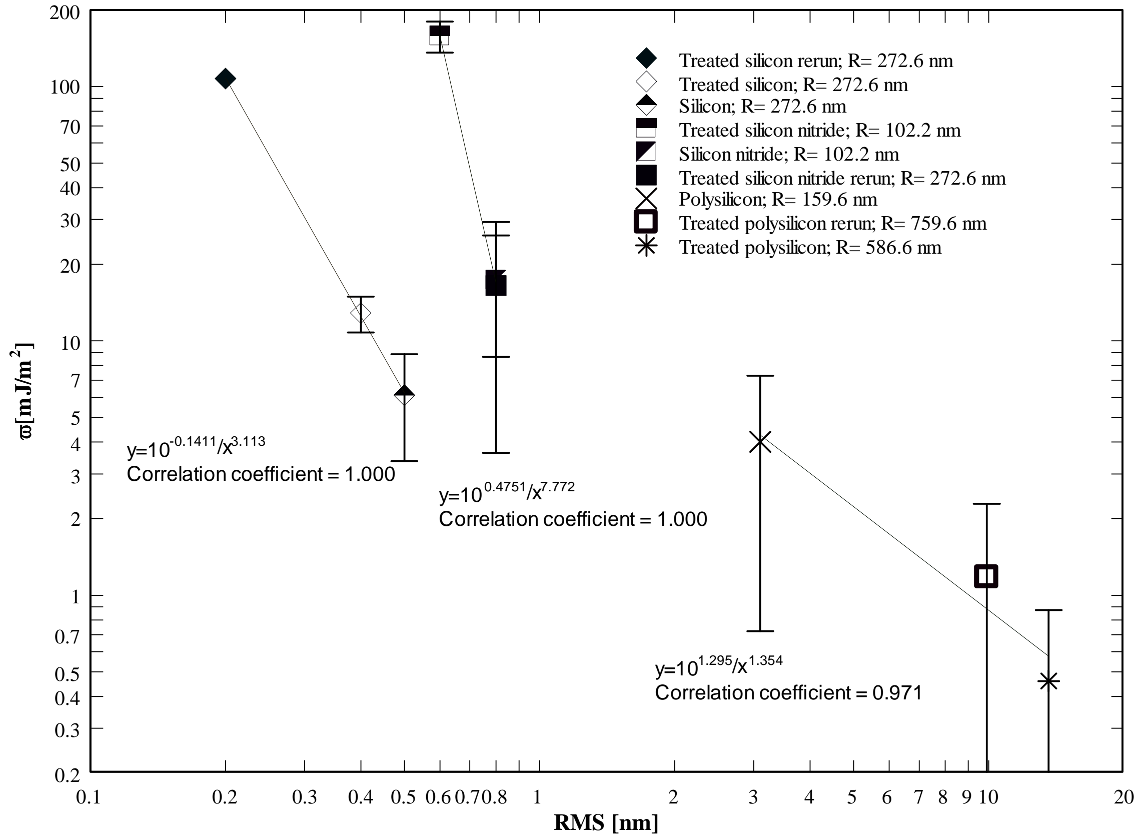

Figure I-8. Work of adhesion as function of RMS roughness for six different substrates. A different tip was used for the polysilicon (treated and untreated) samples (radii listed in the figure key). The silicon wafers had the lowest overall roughness. The treated silicon nitride had the highest work of adhesion followed by the treated silicon rerun. The uncertainty in the measured RMS value is expected to be 0.2 nm for one standard deviation. The y-error bars represent one standard deviation.

I.4 Roughness

Comparing roughnesses on the different wafers, the treated polysilicon wafer was rougher than the untreated (the RMS roughness of the treated polysilicon was measured to be 13.0 nm with a different AFM tip, which is similar in roughness to Figure I-1); whereas for the silicon wafer the trend is reversed (the untreated is rougher). The first run of the RMS roughness for the treated silicon nitride surface was lower (0.6 nm) than the rerun measurement (0.8 nm). The RMS roughness for the rerun data point of the treated

silicon surface was less (0.2 nm). In light of the assumed error in the RMS roughness, the difference seen for silicon and silicon nitride are not significant.

From the additional test for the influence of surface roughness on the work of adhesion, it was found that the measured work of adhesion for the smooth untreated no die-attachment silicon die was 54 ± 5 mJ/m^2 (RMS roughness 0.2 nm) and for the roughened untreated no die-attachment was 51 ± 42 mJ/m^2 (RMS roughness 36.3 nm).

I.5 Work of adhesion

Comparing the works of adhesion and their scatter for the different wafers, the treated silicon nitride had the highest work of adhesion followed by the treated silicon rerun. The treated polysilicon rerun wafer had the lowest work of adhesion and the highest scatter in the measurements for the work of adhesion. The treated silicon rerun had the lowest scatter in the measurements for the work of adhesion.

I.6 Tip cleaning

From testing the influence of tip-cleaning, it was found that the measured work of adhesion for the untreated silver-glass die-attachment was 19 ± 1 mJ/m^2 (RMS roughness 1.0 nm) and for the treated 36 ± 15 mJ/m^2 (RMS roughness 0.2 nm). Previously, the measured work of adhesion for the untreated silver-glass die-attachment was 310 mJ/m^2 (RMS roughness 0.2 nm) and for the treated 390 mJ/m^2 (RMS roughness 0.3 nm).

I.7 Discussion

I.7.1 Roughness

The polysilicon and silicon nitride wafers seemed to be unusually rough, which is expected for unpolished wafers. From Figure I-8, it is evident that the work of adhesion is

lower for the rougher wafer. Specifically, the work of adhesion is lower on the treated than the untreated polysilicon wafer; whereas the trend is reversed for the other two types of treated and untreated wafers. Clearly, roughness plays a large role (increased roughness can reduce the real contact area and reduce the work of adhesion). Caution should be adhered to when analyzing the affect of the RMS roughness on the work of adhesion. The roughness can be measurably different for different length scales. The reported RMS roughness values were measured for a two-micron by two-micron topography image. The RMS roughness may be different between the whole two-micron squared topography image and the point where the force curves were acquired. The expected error in the measurement of the RMS roughness is 0.2 nm, the limit for detection of deflection with our instrument. The RMS roughness for a normal AFM tip is assumed to make a single point contact with the sample surface. Therefore, roughness of the AFM tip is assumed to not contribute to the work of adhesion.

Roughening the sample surface of the no die-attach untreated silicon die did not cause a significant decrease in the work of adhesion However after roughening the surface, the scatter in the measured works of adhesion did increase significantly. This might indicate that not only is the RMS roughness important, but so is the distance between asperities (points of contact).

I.7.2 Work of adhesion

The work of adhesion for the silicon nitride was in the range of what would be expected for a thick layer of water (142 mJ/m^2). Either the treated silicon rerun or the silicon nitride could have been influenced by either a water layer, the surface chemistry, or charging. A thick layer of water would be unexpected, since the dew point temperature

was low. The wafer surfaces are assumed to have a well defined surface chemistry that varies little over the span of the wafer, so it would be unexpected that local variations in surface chemistry play a role. Charging could increase the work of adhesion, but it is not clear why the work of adhesion was so different between the first and rerun data point for the silicon and silicon nitride sample. The linear trends (from Figure I-8) for the three types of crystals include both the treated and untreated versions. The cause for the high variability in the work of adhesion is unknown.

In some cases, the work of adhesion varied by more than 20% from sample run to sample run and from site to site. The high variability might be caused by a combination of local variations in the contact roughness (both the RMS roughness and the mean distance between asperities) and the surface condition (i.e. charging or surface chemistry) at contact.

I.7.3 Tip cleaning

Cleaning a normal AFM tip seemed to cause a lowered work of adhesion for the silver-glass die-attach treated and untreated samples, although the relative humidity, at the time of the measurements, for the cleaned tips was about twice that for the uncleaned tips. The treated silver-glass die-attach had a higher work of adhesion than untreated silver-glass, which is consistent with previous results. For a 12 μm SiO_2 bead attached to a tipless cantilever, there was no significant difference in the work of adhesion (on untreated no-die attach) between the cleaned and uncleaned tip (cleaned = 3.1 ± 0.6 mJ/m^2; uncleaned = 2.5 ± 0.4 mJ/m^2).

From the *Handbook of semiconductor wafer cleaning technology, science and applications*[2], the most effective method for cleaning silicon surfaces has been to

irradiate a silicon sample with two ultraviolet wavelengths (253.7 nm and 184.9 nm) while bombarding with ozone (O_3) gas for 20 seconds. Irradiating an AFM tip, for one hour with a single wavelength (253.7 nm) and no ozone, will clean the silicon surface of some adsorbents. The tips were cleaned by irradiating for a couple minutes by a single wavelength source (253.7 nm), so a measured change in the work of adhesion, due to cleaning, should not be expected.

I.8 Future work

I.8.1 Surface charge

One way to access the charge state of the surface is to use a scanning probe technique called Kelvin Probe Force Microscopy (KPFM) [3,4]. The method is based on the parallel plate capacitor where the probe for an AFM becomes one of two electrodes for the capacitor and the second electrode is the sample. The amount of surface charge can be monitored by measuring the voltage on each of the plates relative to ground. Even if there is no applied voltage between the electrodes of the capacitor, an electric field can exist due to the differing work functions between materials.

Another way to observe the charge state is to measure the work of adhesion. The work of adhesion between a sample surface and AFM tip is the total energy per unit area required to separate two surfaces. The charge state is just one component to the total work of adhesion, so it is not likely to measure the charge state directly. Since the surface charge would induce an image of itself with opposite sign on the uncharged AFM tip, it would be expected that the presence of charge on the surface would cause a higher than expected work of adhesion, as compared to the condition when no charge is present. If one could place a known amount of fixed surface charge on a sample, one might observe

the difference in the works of adhesion between the presence of a surface charge and no surface charge. However, the KPFM approach would be more appropriate for quantitative analyses of surfaces with charge.

I.8.2 Normal AFM tip radius

Finally, confirmation for the accuracy in measurement of the radius for a normal AFM tip is needed. Comparing measurements made of the normal AFM tip shape with TEM, a step-function, and delta-function, the accuracy of the measured radius for a normal AFM tip can be verified.

I.8.3 AFM tip roughness

The roughness of a normal AFM tip is not expected to contribute to the work of adhesion. The roughness of SiO_2 beads attached to cantilevers can contribute to the work of adhesion. Observing roughnesses (of the sample and attached beads) is important to the understanding of the nature of contact roughness and its influence on the work of adhesion.

REFERENCES

[1] B. D. Terris, J. E. Stern, D. Rugar et al., Physical Review Letters **63** (24), 2669-2672 (1989).

[2] Werner Kern and Knovel (Firm), (Noyes Publications, Park Ridge, N.J., U.S.A., 1993), pp. xx, 623 p.

[3] Lord Kelvin, Nature (1881).

[4] M. Nonnenmacher, M. P. O'Boyle, and H. K. Wickramasinghe, Applied Physics Letters **58** (25), 2921-2923 (1991).

Appendix J. Report on the works of adhesion between no die-attach samples (untreated and treated) and an AFM tip before and after application of UV light, heat, and a positively charged source (StaticmasterTM brush).

Table of Contents

Appendix J. Report on the works of adhesion between no die-attach samples (untreated and treated) and an AFM tip before and after application of UV light, heat, and a positively charged source (StaticmasterTM brush). J-1
J.1 Introduction J-4
J.2 Experimental methods J-4
J.3 Results J-9
J.1.1 Roughness J-14
J.1.2 Work of adhesion J-14
J.4 Discussion J-16
J.1.3 UV light J-16
J.1.4 Heating J-17
J.1.5 Staticmaster^{TM} (UND141 and TND142) J-18
J.5 Conclusions J-18
J.6 Future work J-20
J.1.6 UV J-20
J.1.7 Heat J-20
J.1.8 Gloves J-21

List of Figures

Figure J-1. Untreated no die-attach (UND22) before and after seven minutes of UV light irradiation. RMS roughness was 0.3 ± 0.1 nm. The average work of adhesion was 130 mJ/m^2 ± 20 % before irradiation and after it was 190 mJ/m^2 ± 20%. Treated no die-attach (TND26) before and after seven minutes of UV light irradiation. RMS roughness was 0.3 ± 0.1 nm. The average work of adhesion was 70 mJ/m^2 ± 90 % before irradiation and after it was 140 mJ/m^2 ± 30 %. UND22 and TND26 were previously opened samples. The error bars represent one standard deviation for the measured works of adhesion for all locations within one global site. J-9

Figure J-2. The works of adhesion for the untreated (UND141) no die-attach before and after heat was applied to only the samples (200 °C for one hour). RMS roughness was 0.3 ± 0.1 nm. The average work of adhesion was 210 mJ/m^2 ± 30 % before the application of heat and after it was 250 mJ/m^2 ± 20 %. Treated (TND142) no die-attach before and after applied heat (200 °C for one hour). RMS roughness was 0.3 ± 0.1 nm. The average work of adhesion was 160 mJ/m^2 ± 40 % before the application of heat and after it was 250 mJ/m^2 ± 30 %. The error bars represent one standard deviation for the measured works of adhesion for all locations within one global site. J-10
Figure J-3. The works of adhesion for the untreated (UND141) no die-attach before and after applied heat (200 °C for one hour) to both the AFM tip and sample. RMS roughness was 0.2 ± 0.1 nm. The average work of adhesion was 220 mJ/m^2 ± 50 % before the application of heat and after it was 180 mJ/m^2 ± 20%. Treated (TND142) no die-attach before and after applied heat (200 °C for one hour) to both the tip and sample. RMS roughness was 0.3 ± 0.1 nm. The average work of adhesion was 230 mJ/m^2 ± 50 % before the application of heat and after it was 110 mJ/m^2 ± 70%. The error bars represent one standard deviation for the measured works of adhesion for all locations within one global site.......... J-11
Figure J-4. The works of adhesion for the untreated (UND171) no die-attach before and after applied heat (200 °C for 15 min.) to both the AFM tip and sample. The RMS roughness for UND.TA.before (Untreated No Die-attach.Tip A.before thermal treatment) was 0.3 ± 0.1 nm. The work of adhesion was 126 mJ/m^2 ± 11%. The RMS roughness for UND.TB.before (Untreated No Die-attach.Tip B.before thermal treatment) was 0.5 ± 0.1 nm. The work of adhesion was 131 mJ/m^2 ± 22%. The RMS roughness for UND.TB.after (Untreated No Die-attach.Tip B.after thermal treatment) was 0.3 ± 0.1 nm. The work of adhesion was 64 mJ/m^2 ± 30%. The error bars represent one standard deviation for the measured works of adhesion for all locations within one global site.......... J-12
Figure J-5. The works of adhesion for the untreated (UND141) no die-attach before and after brushing the sample with a Staticmaster^{TM} brush (positive charge source). RMS roughness was 0.3 ± 0.1 nm. The average work of adhesion was 250 mJ/m^2 ± 20 % before the application of heat and after it was 220 mJ/m^2 ± 50%. Treated (TND142) no die-attach before and after applied heat (200 °C for one hour) to both the tip and sample. RMS roughness was 0.3 ± 0.1 nm. The average work of adhesion was 250 mJ/m^2 ± 30 % before the application of heat and after it was 230 mJ/m^2 ± 50%. The error bars represent one standard deviation for the measured works of adhesion for all locations within one global site.......... J-13

List of Tables

Table I-1. The works of adhesion for the untreated (UND169) and treated no die-attach (TND170) recently opened samples before and after UV irradiation for seven minutes. The uncertainty represents one standard deviation for the measured works of adhesion for all locations within one global site. J-9

Abstract

Surfaces exposed to air can become contaminated. The contaminated surfaces can cause the work of adhesion to be different than expected for ideal surfaces that come into contact with each other. The purpose of this work was to explore the influence of different types of surface preparations on the measured works of adhesion between an AFM tip and sample surface. With the proper surface treatment, contamination on the surface can be minimized or removed. The work of adhesion was measured between no die-attach samples that were untreated (native oxide) and treated (few angstroms of diphenylsiloxane) before and after several different types of surface preparations. The preparations were the application of UV (Ultra-Violet) light, heat, and a positively charged source (Staticmaster™ model # 1C200). The work of adhesion was influenced by the application of UV light. Heating both the AFM tip and sample together seemed to lower the work of adhesion. The results suggest that surface contaminates can be removed or minimized by the application of UV light or heat. If the values for the works of adhesion, after the surface preparation, are found to have a repeatable value, it is expected that the no die-attach samples (with and without a few angstroms of vapor deposited diphenylsiloxane) could be used as adhesion standards.

J.1 Introduction

The local surface condition at contact can influence the work of adhesion. The local surface chemistry is affected by absorbed species, defects, and preparation. Charging can also occur between insulators (dielectrics) via charge exchange[1] caused by local differences in the work functions of the tip and sample. Adsorbed species typically lower the work of adhesion and charging increases the work of adhesion. With proper surface treatment, samples that have been exposed to environmental contaminants might be returned to their precontaminant state.

This report will present data obtained by measuring the works of adhesion on seven different samples (with and without a few angstroms of vapor deposited diphenylsiloxane) that were treated differently in an attempt to return the surfaces to precontaminant state.

J.2 Experimental methods

The radius of the tip (a parabolic fit to a linescan of a topography image of a delta function and AFM tip) and the spring constant of the cantilever were measured. Since a topography image for an AFM is a dilation between the sample surface and the inverted shape of the tip, the measured radius of the tip will be larger than the actual tip radius. For SiO_2 beads attached to tipless cantilevers, the relative uncertainty for the radius measurement is 9 %[2]. To estimate the relative uncertainty for a normal AFM tip, the spacing between spikes on a delta-function (TGT01) grating was measured with an SEM (Scanning Electron Microscope) and AFM (with a normal AFM tip). The spacing as measured by the SEM was 2.26 ± 0.01 μm and as measured by the AFM was 2.32 ± 0.07 μm. The lateral measured distances with the SEM and AFM were in good agreement

(within 2%). Measurement of the tip radius requires knowledge of uncertainties for both lateral (x and y-direction) and normal (z-direction) measured distances that the AFM tip and cantilever move. The normal measured distance (z-direction) has a relative uncertainty of 2%. Using the method of quadratures the relative uncertainty for the tip radius is 3 %. To be conservative we multiply that by a factor three and, so, the estimated relative uncertainty, in the radius, for a normal AFM tip is 9%.

There was a total of seven different samples. Two (untreated no die-attach # 22 and treated no die-attach # 26) of the samples were exposed to ambient laboratory conditions for 16 months. Two (untreated no die-attach # 141 and treated no die-attach # 142) of the samples were exposed to ambient laboratory conditions for 9 months. Three (untreated no die-attach #169, untreated no die-attach #171, and treated no die-attach #170) samples were recently opened. Untreated No Die-attach # 22 (UND22) and Treated No Die-attach # 26 (TND26) samples were from the lot fabricated in May 2003. Untreated No Die-attach # 169 (UND169), Treated No Die-attach # 170 (TND170), Untreated No Die-attach # 141 (UND141), Untreated No Die-attach # 171 (UND171), and Treated No Die-attach # 142 (TND142) no die-attach samples were from the lot fabricated in October 2003. The die were placed on the AFM stage and imaged with a normal AFM tip. The same tip was used throughout all experiments contained in this report, except for measurements taken on UND171. The RMS roughness was measured from a two-micron by two-micron image of the die. Sixteen approach and retraction force curves were obtained at different locations across a two-micron square section of the die. Each location was an average of sixteen force curves at a single location. There were a total of four different two-micron square images (one two-micron square image is

referred to as a global site) taken on each die (except for the recently opened UND169 and TND170). The pull-off force (F_{po}) was measured at the sixteen different locations and was used to determine the work of adhesion (ϖ) at each global site.

$$F_{po} = -k\,\delta z\ , \qquad \text{J.1.}$$

where k is the spring constant and δz is the deflection of the AFM cantilever.

$$\varpi = \left|\frac{F_{po}}{2\pi R}\right|, \qquad \text{J.2.}$$

where F_{po} is the pull-off force and R is the AFM tip radius. The reported values for the works of adhesion were the average of the sixteen different locations for each global site. The process was repeated at four global sites before and after the application of seven minutes of UV light (UND22, TND26, UND169, TND170), the application of heat (UND141, UND171, and TND142), and the application of a positively charged particle source (Staticmaster™ brush model# 1C200) to the samples (UND141 and TND142). Only one image of a global site and its force curve data were taken for the samples UND169 and TND170.

The works of adhesion were measured after the samples (UND141 and TND142) were heated to 200 ± 2 °C and then baked for 60 ± 6 minutes. The UND141 and TND142 samples were placed (separate crucibles; different times) into the muffle furnace (Thermolyne type 1500 furnace), when the furnace reached 200 °C. When the bake time was completed (~ 1 hr.), the crucibles were removed and allowed to cool down to room temperature. The application of heat was repeated to the samples UND141 and TND142 except that the AFM tip and sample were placed together.

The work of adhesion was measured between the sample UND171 with two different tips (Tip A and Tip B), on two consecutive days. On the second day, the sample and tip (Tip B) were handled with gloves and face mask to reduce possible human contaminants. After the work of adhesion was measured with tip B, the sample and tip were heated to 200 ± 2 °C and then baked for 15 ± 1 minutes. The UND171 sample and tip were placed into a crucible and then set on top of a heating plate (Corning Hot Plate model # PC-400). When the bake time was completed (~ 15 min.), the crucible was removed and allowed to cool down to room temperature before being placed on the AFM stage.

To make the study time-feasible, the radius of the AFM tip and the spring constant of the cantilever were measured at the beginning of the experiment (the same tip was used for the entire experiment). The radius of the same tip was measured before and after measuring the works of adhesion on UND169 and TND 170 and the radius was found to be 154.7 ± 14.3 nm. Since the radii measurements were all within 9% of each other, it seems reasonable to claim that the radius of the AFM tip was not significantly changed by measuring the treated or untreated no die-attach sample surfaces.

The works of adhesion were measured for UND141 and TND142, after being gently brushed with a positively charged particle source to reduce the static charge build-up and dust. The untreated sample # 141 (UND141) and treated sample # 142 (TND142) were measured with a normal AFM tip before and after being swiped with a Static Master brush.

All measurements were made at a relative humidity of 29 ± 12 % and temperature of 21.1 ± 1.0 °C. The relative uncertainty for the work of adhesion is 15 % (10 % relative

uncertainty for the pull-off force and 9% relative uncertainty for the tip radius) by the method of quadratures (the measurement errors are independent and random). All error bars in the plots represent one standard deviation of the scatter in the measurements.

J.3 Results

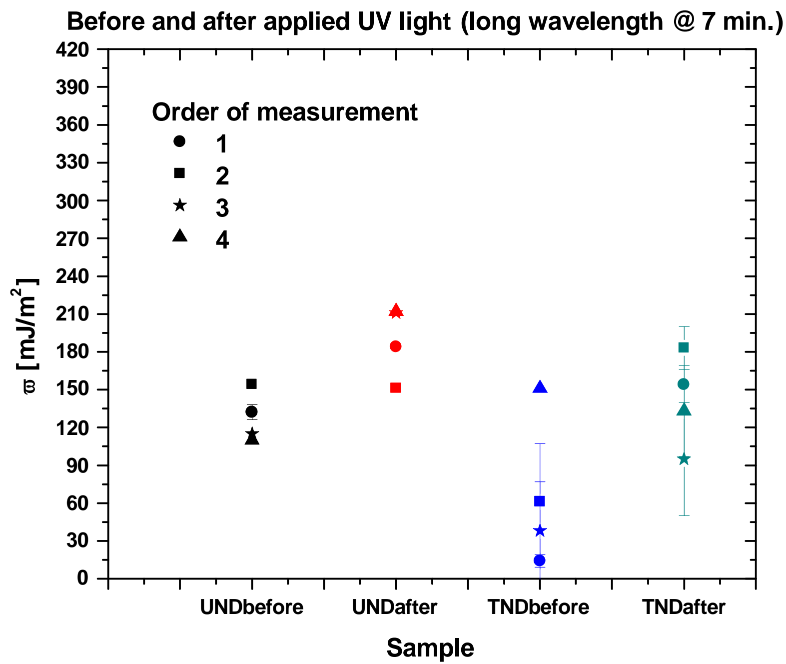

Figure J-1. **Untreated no die-attach (UND22) before and after seven minutes of UV light irradiation. RMS roughness was 0.3 ± 0.1 nm. The average work of adhesion was 130 mJ/m^2 ± 20 % before irradiation and after it was 190 mJ/m^2 ± 20%. Treated no die-attach (TND26) before and after seven minutes of UV light irradiation. RMS roughness was 0.3 ± 0.1 nm. The average work of adhesion was 70 mJ/m^2 ± 90 % before irradiation and after it was 140 mJ/m^2 ± 30 %. UND22 and TND26 were previously opened samples. The error bars represent one standard deviation for the measured works of adhesion for all locations within one global site.**

Sample	RMS roughness[nm]	ϖ[mJ/m2]	Std. Dev. [%]
UND169 Before	0.2	90	10
UND169 After	0.2	120	1
TND170 Before	0.2	110	10
TND170 After	0.2	30	30

Table I-1. The works of adhesion for the untreated (UND169) and treated no die-attach (TND170) recently opened samples before and after UV irradiation for seven minutes. The uncertainty represents one standard deviation for the measured works of adhesion for all locations within one global site.

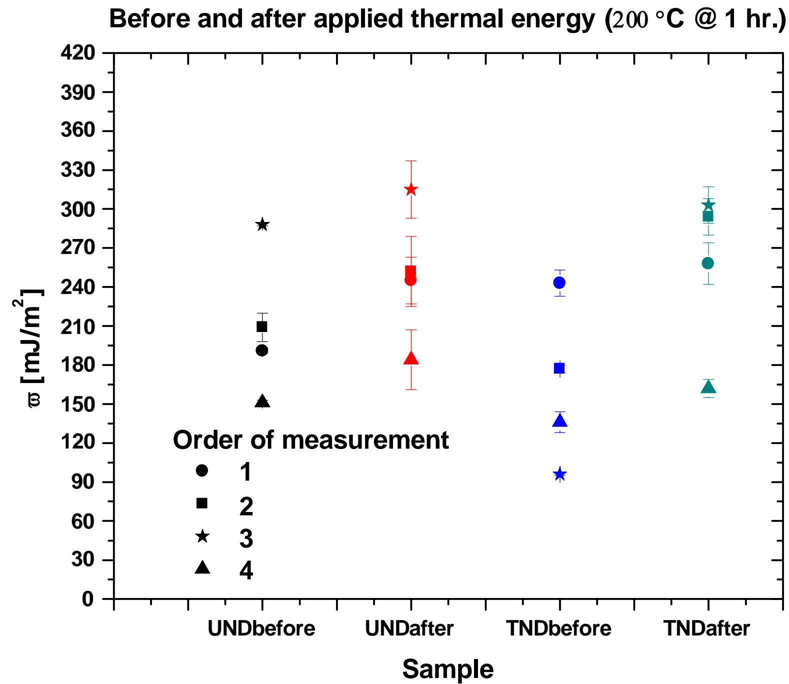

Figure J-2. The works of adhesion for the untreated (UND141) no die-attach before and after heat was applied to only the samples (200 °C for one hour). RMS roughness was 0.3 ± 0.1 nm. The average work of adhesion was 210 mJ/m^2 ± 30 % before the application of heat and after it was 250 mJ/m^2 ± 20 %. Treated (TND142) no die-attach before and after applied heat (200 °C for one hour). RMS roughness was 0.3 ± 0.1 nm. The average work of adhesion was 160 mJ/m^2 ± 40 % before the application of heat and after it was 250 mJ/m^2 ± 30 %. The error bars represent one standard deviation for the measured works of adhesion for all locations within one global site.

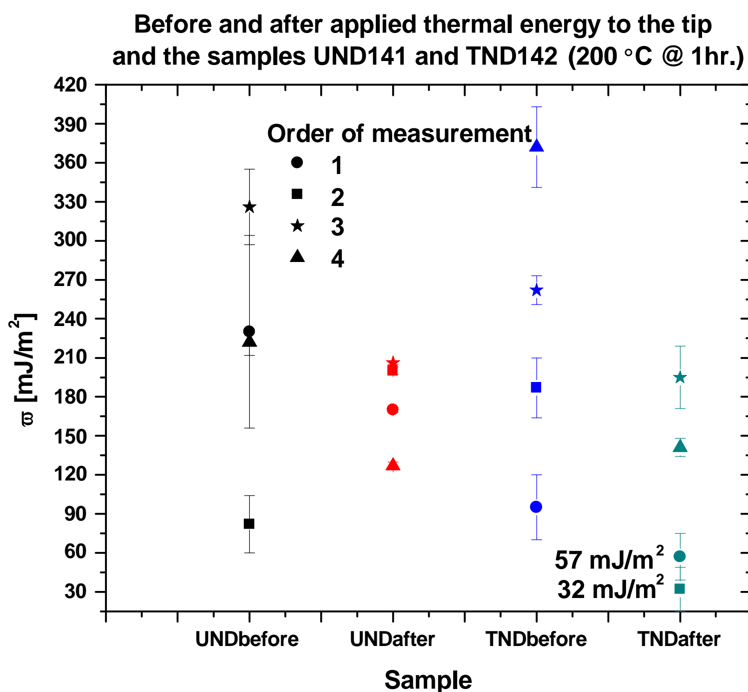

Figure J-3. The works of adhesion for the untreated (UND141) no die-attach before and after applied heat (200 °C for one hour) to both the AFM tip and sample. RMS roughness was 0.2 ± 0.1 nm. The average work of adhesion was 220 mJ/m^2 ± 50 % before the application of heat and after it was 180 mJ/m^2 ± 20%. Treated (TND142) no die-attach before and after applied heat (200 °C for one hour) to both the tip and sample. RMS roughness was 0.3 ± 0.1 nm. The average work of adhesion was 230 mJ/m^2 ± 50 % before the application of heat and after it was 110 mJ/m^2 ± 70%. The error bars represent one standard deviation for the measured works of adhesion for all locations within one global site.

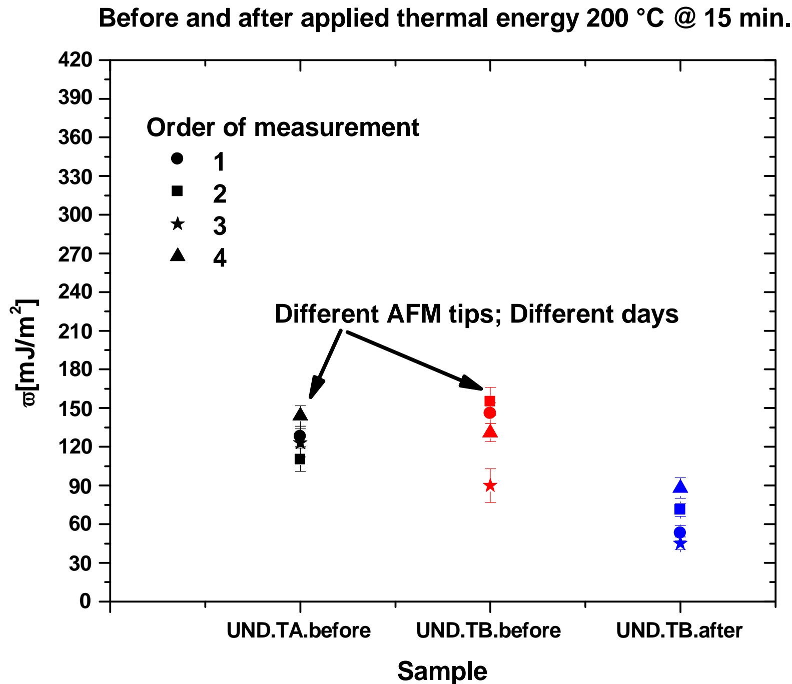

Figure J-4. The works of adhesion for the untreated (UND171) no die-attach before and after applied heat (200 °C for 15 min.) to both the AFM tip and sample. The RMS roughness for UND.TA.before (Untreated No Die-attach.Tip A.before thermal treatment) was 0.3 ± 0.1 nm. The work of adhesion was 126 mJ/m^2 ± 11%. The RMS roughness for UND.TB.before (Untreated No Die-attach.Tip B.before thermal treatment) was 0.5 ± 0.1 nm. The work of adhesion was 131 mJ/m^2 ± 22%. The RMS roughness for UND.TB.after (Untreated No Die-attach.Tip B.after thermal treatment) was 0.3 ± 0.1 nm. The work of adhesion was 64 mJ/m^2 ± 30%. The error bars represent one standard deviation for the measured works of adhesion for all locations within one global site.

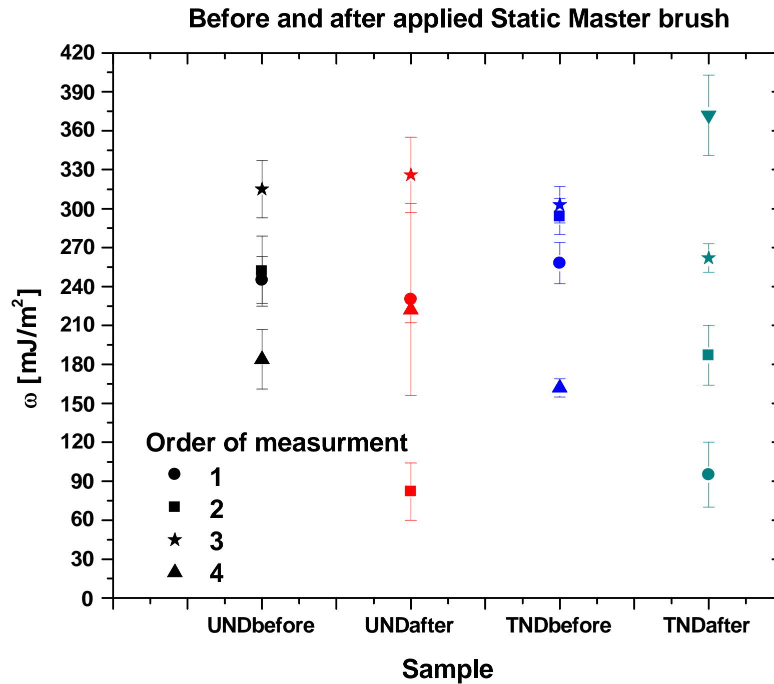

Figure J-5. The works of adhesion for the untreated (UND141) no die-attach before and after brushing the sample with a Staticmaster™ brush (positive charge source). RMS roughness was 0.3 ± 0.1 nm. The average work of adhesion was 250 mJ/m^2 ± 20 % before the application of heat and after it was 220 mJ/m^2 ± 50%. Treated (TND142) no die-attach before and after applied heat (200 °C for one hour) to both the tip and sample. RMS roughness was 0.3 ± 0.1 nm. The average work of adhesion was 250 mJ/m^2 ± 30 % before the application of heat and after it was 230 mJ/m^2 ± 50%. The error bars represent one standard deviation for the measured works of adhesion for all locations within one global site.

J.1.1 Roughness

The resolution for movement in the normal direction (z-direction) with our instrument is about 2 Å (0.2 nm). The samples did not display any change in RMS roughness (0.3 ± 0.1 nm) for the UV treatment process, the application of heat, or application of a positively charged source (Staticmaster™ brush).

J.1.2 Work of adhesion

J.1.2.1 UV light (UND22, TND26, UND169 and TND170)

The works of adhesion were measured before and after seven minutes of UV irradiation at four different global sites. The average untreated no die-attach (UND22) work of adhesion value, before irradiation, is consistent with water on the surface. (ϖ_{H20} = 142 mJ/m^2; see Figure J-1.) Likewise, the average treated no die-attach (TND26) work of adhesion value, after irradiation, suggests that water might be on the surface. UV light seems to increase the works of adhesion for all samples except the recently opened treated samples (TND170; Table I-1). The value for the work of adhesion with TND170, after irradiation, is consistent with previous results on different treated no die-attach sample (previous results ~33 mJ/m^2)[3].

J.1.2.2 Heat (UND141, TND142, and UND171)

Both samples were attached to double-sided sticky tape and removed from their container, which was exposed to ambient laboratory conditions. Both samples displayed flaking at the edges when removed. UND141 had more flaking, which left dust bits on the surface. The UND141 surface was cleaned with compressed gas (100 % tetrafluoroethane). TND142 was not cleaned. The works of adhesion (both before and after) were significantly higher than when measured upon opening (UND141 ~ 50 mJ/m^2

and TND142 ~ 33 mJ/m^2)[3]. The tweezers that were used to remove the samples from their container made rubbing contact with the sample and double-sided sticky tape, which might have caused static charging of the sample. The samples used were the same as measured for the work of adhesion as a function of radius data.

The works of adhesion (both before and after) were higher than when measured upon opening (UN141 ~ 50 mJ/m^2 and TND142 ~ 33 mJ/m^2), when heating was applied only to the samples (see Figure J-2).

The works of adhesion were measured between an AFM tip and the samples UND141 and TND142 after heat was applied to both tip and the respective sample (see Figure J-3). For UND141 after the application of heat to it and the AFM tip, the work of adhesion decreased slightly and the scatter decreased. For TND142 after the AFM tip and sample were heated, the work of adhesion decreased significantly. The first two measurements had works of adhesion consistent with the value found for the work of adhesion study (~ 33 mJ/m^2). The third measurement had a really high work of adhesion and the fourth measurement was consistent with water being present between the tip and sample (ϖ_{H20} = 142 mJ/m^2).

The works of adhesion were measured between two different AFM tips and the sample UND171 (see Figure J-4), on two consecutive days. The measured works of adhesion were close to each other for the two different tips. They had a high work of adhesion, which was consistent with water being present between the tip and sample (ϖ_{H20} = 142 mJ/m^2).

On the second day and after an initial set of work of adhesion measurements, tip B and sample UND171 were heated together in a crucible that was on top of a heating

plate. After heating, the measured work of adhesion was lower than the previous two measurements, indicating that water was no longer present between the sample and tip (see Figure J-4).

J.1.2.3 Staticmaster™ brush (UND141 and TND142)

The works of adhesion (both before and after) were higher than when measured upon opening (UN141 ~ 50 mJ/m^2 and TND142 ~ 33 mJ.m2). The application of the brush seemed to increase the work of adhesion and the scatter in the measurements (see Figure J-5).

J.4 Discussion

J.1.3 UV light

J.1.3.1 Old samples (UND22 and TND26)

The works of adhesion were increased for both UND22 and TND26 (see Figure J-1). This was most significant for TND26. The scatter in the data was large for TND26 before irradiation and after the irradiation the scatter was decreased slightly. Clearly, the irradiation of the samples with UV light seems to have some influence on the work of adhesion. It is plausible that any samples measured in our laboratory might be influenced by UV light. If a package were to leak (allow a small amount of UV light to enter) the samples might measure an increased work of adhesion over time.

J.1.3.2 New samples (UND169 and TND170)

The work of adhesion for UND169 was increased by the application of UV light, but the scatter was not significantly different between before and after measurements (see Table I-1). The most intriguing result was for TND170. The application of UV light to TND170 causes a significantly lower work of adhesion value that is consistent with

previous measurements (previous measurement was ~ 33 mJ/m^2)[3]. It is not clear why this occurs, although the old and new samples were from different lots. The old samples were produced in May 2003 and the new samples were produced in October 2003. It appears that the application of UV light is beneficial in only one case; the treated no die-attach samples produced in October 2003.

J.1.4 Heating

J.1.4.1 Samples only (UND141 and TND142)

Heating only the samples seemed to cause slightly higher works of adhesion (see Figure J-2). Since the work of adhesion is a measurement that depends of both surfaces of contact it seems likely that the work of adhesion will be dependant on the local surface properties of both surfaces that are in contact. For a cleaning technique to be successful both the AFM tip and sample surface must be cleaned.

J.1.4.2 AFM tip and samples (UND141 and TND142)

Heating the AFM tip and the samples seemed to cause a slightly lower work of adhesion and a slightly lower scatter in the measurements (see Figure J-3). However, only TND142 displayed works of adhesion values close to the values for the works of adhesion at first opening (at first opening ~ 33mJ/m^2). This seems to indicate that under certain circumstances the treated no die-attach sample might be used as an adhesion standard.

J.1.4.3 Different tips and sample UND171

There was no statistically observed difference in the work of adhesion when measured by two different tips (tip A and B). Tip A was a previously used tip. Tip B was

a new tip. Additionally for tip B, proactive steps were taken to minimize the influence of human contaminants, as described in the methods section.

A lowered work of adhesion was measured after heating for about 15 minutes.

J.1.5 Staticmaster™ (UND141 and TND142)

The work of adhesion values and the scatter in the measurements were increased after the application of the Staticmaster™ brush (see Figure J-5). It is plausible that if the sample surface is neutral prior to the application of the brush, it may gain a positive net charge. Since the AFM tip is assumed neutral, there will be an equal in magnitude but opposite sign for the charge induced on the AFM tip causing an increased attraction between the tip and sample, which might explain the increased work of adhesion between the tip and sample after application of the brush.

J.5 Conclusions

The works of adhesion were measured on seven different samples before and after four different types of preparation. The first preparation was to expose the samples UND22, TND26, UND169, and TND170 to UV light for seven minutes. Only the recently opened sample TND170 measured a work of adhesion value close to the previously measured value for the work of adhesion. The previous measured value was from TND142[*]. The second preparation was to heat only the samples (UND141 and TND142). As a follow-up to the second preparation, heat was applied to the samples (UND141 and TND142) and AFM tip. Only under the condition of heat applied to the tip and sample (TND142), was the measured a work of adhesion value close to previous measured value for the work of adhesion (the previous measured was 33 mJ/m^2). The

[*] The measured value was 33 mJ/m^2 after it was first opened and with a different AFM tip.

third preparation was to apply heat to sample UND171 and AFM tip B, which seemed to decrease the work of adhesion. The final preparation was to apply a positively charged source (Staticmaster™ brush) to the samples (UND141 and TND142), which seemed to increase the work of adhesion and the scatter in the measurements.

The treated no die-attach had a value for the work of adhesion of approximately 30 mJ/m^2 on three separate samples (See Table 1, Figure 3, and footnote at the bottom of the page.) and with different tips. However, there is a large scatter in the work of adhesion which can vary, at the least, by a factor of two for a single sample. It is presumed that these variations are due to contaminants on the sample surface or AFM tip.

The untreated no die-attach had a value for the work of adhesion of 64 mJ/m^2 ± 30% (see Figure 4) after the tip and sample were heated together for 15 minutes at 200 °C. That value is consistent with a previous measured value of 49 mJ/m^2 and noticeably different than the treated no die-attach sample. Furthermore before the tip and sample were heated, the value for the work of adhesion was about the same when measured with a different tip on a different day (See Figure 4).

The results here seem to indicate two possibilities for removing surface contaminates. 1) The application of UV energy to the treated no die-attach samples that were recently opened and 2) heating the sample and AFM tip together. All samples had a low surface roughness and did not display visible wear during imaging, which would suggest that these surfaces might be used as work of adhesion standards (once the optimum conditions for a cleaning process are determined).

J.6 Future work

J.1.6 UV

The influence on the works of adhesion due to the application of UV light most likely is time and intensity dependent. The samples could be irradiated for different lengths of time and their works of adhesion measured to optimize the time required to achieve a freshly opened state. The UV light source would also need to be measured in terms of wavelength and power or intensity output. So, three variables (the time exposed, the wavelength of the light, and the intensity of the irradiation) could be investigated to determine the optimum cleaning conditions. Due to the application of UV light, one would have a deeper understanding of the influence to the work of adhesion and would gain insight into devices that are exposed to ambient sunlight.

J.1.7 Heat

Although the results are promising for cleaning a treated or untreated silicon surface by the application of heat, it is not clear whether 200 ℃ is the optimum temperature which most effectively removes the impurities on the sample surface. One could vary the temperature and length of time exposed to heat to determine which set of conditions returns the work of adhesion to freshly opened values. Additionally, one could repeat the same experiment multiple times to obtain better statistics. This would require opening a sample, measuring the work of adhesion at four different global sites, letting it sit for a month or longer, applying heat to the tip and sample, and then remeasuring the work of adhesion at four global sites.

The samples were placed directly into the furnace that was already at 200 °C and then they were removed directly to room temperature and allowed to cool down (about 15

minutes). Is there any influence on the work of adhesion caused by the rapid heat-up and cool-down of the samples?

The best results were observed when the tip and sample were heated together in the same crucible. What influence would there be on the work of adhesion if just the tip was heated?

J.1.8 Gloves

Human skin dandruff, oils, and impurities from breathing, can contaminate surfaces and they are a leading cause for contamination in clean rooms for wafer fabrication facilities. The samples are opened in ambient and are then exposed to a number of different hydrocarbons and impurities. No data suggest that the work of adhesion is influenced by samples that come close to human proximity during handling of the samples. One could acquire additional statistics by measuring the work of adhesion with and without gloves to determine whether there really is any human influence when working in close proximity to the samples. The laboratory dew point is low, so it is not expected that water will condense on the samples or tips. If the dew point is low and water molecules are not physisorbed onto the surface, why would the work of adhesion measure values consistent with water being on the surface?

Although UHV (Ultra High Vacuum) is not a typical operating environment for MEMS, insight might be gained by performing the work of adhesion experiments in UHV environment. The UHV environment should represent the cleanest (free from physically adsorbed species) environment and, measuring the work of adhesion in that environment, should represent the idealized value for the measured work of adhesion between two similar materials.

REFERENCES

[1] B. D. Terris, J. E. Stern, D. Rugar et al., "Contact electrification using force microscopy," Physical Review Letters **63** (24), 2669-2672 (1989).

[2] E. J. Thoreson and N. A. Burnham, "Standard-deviation minimization for calibrating the radii of spheres attached to atomic force microscope cantilevers," Review of Scientific Instruments **75** (5), 1359-1362 (2004).

[3] E. J. Thoreson, J. Martin, and N. A. Burnham, presented at the ISTFA, Worcester, MA, 2004 (unpublished).

K. Recommendations for the use of an Atomic Force Microscope as an in-fab stiction monitor

Abstract

An Atomic-Force Microscope (AFM) can be used to monitor surface qualities (by measuring the work of adhesion) related to stiction at different stages of manufacture, which then might be correlated to device performance. The four main challenges to using the AFM as an in-fab stiction monitor are calibration, effects from the angle of repose of the cantilever, surface roughness, and material properties. We measured the work of adhesion between different AFM tips and samples. There were seventeen tips of four different types, with radii from 200 nm to 60 μm, covering the range of typical MEMS contacts. The samples were unpatterned amorphous silicon dioxide MEMS die with two types of surface conditions (untreated and treated with a few angstroms of vapor deposited diphenylsiloxane). A simple correction for the surface roughness resulted in the expected dependence for work of adhesion on radius, but the magnitudes were higher than expected. Normal and heat-treated AFM tips have minimal surface roughness and result in magnitudes that were more reliable. In this paper, we review the four main challenges and show their influence on the measured work of adhesion from which we developed a set of recommendations for the use of an AFM as an in-fab stiction monitor.

Introduction

Stiction in MEMS (MicroElectroMechanical Systems) or NEMS (NanoElectroMechanical Systems) devices refers to the high adhesion between two surfaces and is usually associated with the two surfaces becoming permanently adhered to each other. There are two types of stiction 1) in-use and 2) manufacturing. In-use stiction occurs during the operation of MEMS devices where the two surfaces can contact repeatedly, wear, and become permanently adhered to each other, or

they can permanently adhere to each other upon initial contact. Manufacturing stiction can occur at many stages, but usually occurs during the release of some microstructure. The length scale of the contacting surfaces can range from microns to nanometers. For these dimensions, surface forces play a fundamental role in the adhesion between two surfaces. Much literature exists for the review of adhesion (stiction or surface forces)[1, 2, 3, 4, 5, 6, 7, 8, 9, 10] and for techniques to measure them [11, 12, 13, 14, 15].

Improved yields and manufacturing costs might be obtained by understanding stiction, which could be measured by the work of adhesion, the amount of energy required to separate two surfaces from contact out to infinity. The AFM (Atomic Force Microscope), a common tool found in the fab, could measure the work of adhesion at many different stages of manufacture, but there are challenges. To measure the work of adhesion, the AFM cantilever tip is ramped into (approach) and out (retraction) of contact ("force curves"), and the minimum in the retraction curve is the pull-off or adhesive force experienced between the tip and sample (see Figure K-1). The pull-off force normalized by two pi times the radius of the tip is equal to the work of adhesion in the DMT regime (see Equation (K.1)). The advantage of measuring the work of adhesion is that it should be independent of contact size, but our data showed that it was not [16]. The surface roughness was found to be the root cause for the unexpected results. For the AFM to be useful as a quantitative diagnostic tool or an in-fab stiction monitor, four core components need to be understood: calibration, effects due to the angle of repose of the cantilever, surface roughness, and material properties. We will begin by discussing the four core components, show our measured results, and make recommendations for using the AFM as an in-fab stiction monitor.

Calibration of the AFM

The work of adhesion using DMT (Derjaguin, Muller and Toporov) contact mechanics is[17]

$$\varpi = \left| \frac{F_{pull-off}}{2\pi R} \right|, \tag{K.1}$$

where R is the effective radius of curvature for the interface between the tip and sample (it is the radius of the AFM tip for a sphere-flat configuration) and $F_{pull\text{-}off}$ is the pull-off force measured by the AFM. The pull-off force is minus the spring constant (k) of the cantilever times its deflection (d), -kd. Evident from Equation (K.1), the spring constant of the cantilever, radius of the AFM tip, and the deflection of the cantilever must be known. The calibration of the radius of the tip, the spring constant, and deflection of the cantilever has been discussed by us elsewhere [[18], [19]], but we will review how they are measured.

Using a thermal method to measure the spring constant [19], the cantilever was hung freely in air and the deflection of the cantilever, as a function of time, was recorded. The resulting data was Fourier transformed and made into a power spectrum. A plot of the power spectrum resulted in mean-square amplitude (in units of voltage squared) as a function of frequency, and the mean-square amplitude in units of voltage squared was converted to units of nanometers squared. The resulting plot was fit to a fitting function that had three components (pink noise, white noise, and the simple harmonic oscillator) and five parameters. Three of the five parameters used to calculate the spring constant were the quality factor, resonant frequency, and kinetic resonance. The resulting spring constant using the thermal method was [19]

$$k = 0.97070 \frac{Q k_b T \Delta\nu}{\pi \left\langle z^2 \left(\nu_k \right) \right\rangle \nu_k}, \tag{K.2}$$

where Q is the quality factor, k_b is Boltzman's constant, T is temperature in Kelvin, ν_k is the kinetic resonance, $\langle z^2(\nu_k) \rangle$ is the mean-squared amplitude at kinetic resonance, and $\Delta\nu$ is the frequency resolution of the data acquisition device. The advantages to measuring the spring constant via the thermal method were that it can be measured in-situ and it was independent of the geometry of the cantilever.

The movement of the z-scanner was verified through interferometry and the photodiode response was calibrated by ramping the cantilever into and out of contact with a stiff sample [19]. Since the stiff sample was assumed much stiffer than the cantilever, the measured deflection was due entirely to the cantilever.

The radii of the smaller AFM tips (less than a micron) were measured by a common technique. A topography image of a delta-function grating, a series of sharp peaks about 10 nm in diameter and spaced by about 3 μm, was acquired. The resulting topography image was a dilation between the sample surface (delta-function) and the AFM tip. Since the sample surface had features that were much smaller than the smallest sized AFM tips, the resulting topography image was an inverted image of the tip. One line scan of that image was fit to a parabolic function, with the radius of the tip being a parameter of the fit, which was a simplified case of the Blind Reconstruction technique [[20]]. The radii of the larger AFM tips were measured by a similar technique, except that the tips were assumed spherical and a square step was used instead of the delta-function grating [18].

Effects from the angle of repose

The effects caused by the angle of repose of the cantilever can be corrected by two types of corrections to the measured force data. One type of correction was from the tip-sample interface being offset from the end of the cantilever, and the other was a result of considering the torque on the cantilever during pull-off. There was always a torque on the cantilever; however, there is no correction when the angle of repose is equal to zero. The AFM tip can be offset from the end of the cantilever (offset end load), which influences the measured mean-squared amplitude [[21]]. The offset end load correction does not account for the tip being offset from the center of the cantilever, only the end of the cantilever. For normal AFM tips, these corrections were negligible, but for large attached beads, the correction could be important.

Summarizing the method described by J. L. Hutter [16], the force on the cantilever was found by calculating the deflection of the cantilever (see Figure K-2). The magnitude of the torque on the cantilever during unloading (pull-off) was equated to the curvature of the cantilever. Once the deflection had been calculated, the magnitude of the force on the cantilever was the deflection (calculated) times the spring constant. After simplification, the resulting correction due to the angle of repose was [16]

$$F_{\text{repose_corrected}} = \frac{F_{pull-off}}{\cos(\phi)\left[1-\frac{3R}{2L}\tan(\phi)\right]}. \tag{K.3}$$

R is the measured radius of the AFM tip, L is the length of the cantilever, $F_{\text{pull-off}}$ is the measured pull-off force, $F_{\text{repose_corrected}}$ is the corrected force on the cantilever for effects due to the angle of repose only, and ϕ is the measured angle of repose. The correction due to the offset end load was applied when converting the mean-square amplitude from voltage squared to nanometers squared (see reference 16 for details).

Using Equation (K.1) and Equation (K.3), the work of adhesion was

$$\varpi_{\text{repose_corrected}} = \frac{F_{pull-off}}{2\pi R\left[1-\frac{3R}{2L}\tan\phi\right]\cos\phi}. \tag{K.4}$$

(see Figure K-3 and Figure K-4). Correcting the work of adhesion for effects due to the angle of repose, the work of adhesion still decreased with increasing contact size, which was unexpected. As mentioned in the introduction, the root cause was the surface roughness, so we review the influence of surface roughness in the following section.

Surface roughness

According to theoretical predictions, the work of adhesion should be constant as the size of the contact increases, and the pull-off force should increase linearly as the radius of the tip increases. Our experimental data did not match those predictions [22]. As the radius of the tip

increased, the pull-off force was constant, and the work of adhesion decreased with the increased size of the contact (see Figure K-3 and Figure K-4). The surface roughnesses of the tips were found to be the root cause for the discrepancy between experiment and theory. Continuum mechanical models overestimate the contact of rough surfaces, since the actual contact area is less than the apparent contact area. For rough surfaces, the actual contact area should be a summation of all the asperity contact areas. For smooth surfaces, continuum contact models provide an accurate description for the contacting surfaces.

To determine the total interaction force for a hemispherical tip with hemispherical asperities, one must sum the interaction between all molecules of the tip, asperities, and the sample. The asperities from the tip were assumed to be equivalent to a single average asperity, and the RMS (Root Mean Square) roughness was a measure of that average single asperity. Performing the integration over all intermolecular pair potentials and writing the result in terms of the pull-off force [22], the corrected force (for surface roughness and effects due to the angle of repose) was

$$F_{corrected} = \frac{F_{pull-off}}{\left[\left(\frac{(h+2R_a)h^3}{R(h+R_a)^3} - \frac{h}{R} + \frac{R_a}{R}\right) + \frac{h^2}{(h+R_a)^2}\right]\left[1 - \frac{3R}{2L}\tan\phi\right]\cos\phi} . \quad \text{(K.5)}$$

The total corrected (for effects due to the angle of repose and surface roughness) work of adhesion was

$$\varpi_{corrected} = \frac{F_{pull-off}}{2\pi R\left[\left(\frac{(h+2R_a)h^3}{R(h+R_a)^3} - \frac{h}{R} + \frac{R_a}{R}\right) + \frac{h^2}{(h+R_a)^2}\right]\left[1 - \frac{3R}{2L}\tan\phi\right]\cos\phi} . \quad \text{(K.6)}$$

Material Properties

The two main items to consider for the material properties of the tip and sample are homogeneity and material constitution of the AFM tip and sample surface. The tip and sample surface are assumed to be homogenous (i.e. the density is constant), but this might not be true.

There was tight quality control on the sample surfaces manufactured in a MEMS fabrication facility, but not for the AFM tips. Once the samples were manufactured, they were sealed in a container and packaged within the fabrication facility, which was typically a Class 1 clean room. The samples were opened in a less stringent laboratory environment and might have been susceptible to adsorbed particles such as hydrocarbons, and the AFM cantilever's constitutive materials were not as rigorously controlled.

The materials that were in contact might measure pull-off forces or works of adhesion differently than expected because of adsorbed layers, charging between the tip and sample, and work function anisotropies [23]. If the material properties were inhomogeneous across a sample surface, we would have expected to see scatter in the measurements across the sample surface. Adsorbed particles such as hydrocarbons or water can be physisorbed onto a surface and influence the work of adhesion. If water was adsorbed on the surface, the expected value for the measured work of adhesion would be 142 mJ/m^2. If particles were physisorbed, then the work of adhesion typically would measure lower than expected. The dew point was measured to be low, so water was not expected to be physisorbed onto the surface. The scatter in the pull-off forces for each of the data points was at most 30%, which was two standard deviations or less from the average. Therefore, variations in the material properties were not expected to make a statistically significant contribution to the measured pull-off forces.

Experimental

Summarizing the experimental procedure from reference 22, there were two types of samples, an Untreated No Die-attach (UND) and Treated No Die-attach (TND). The UND and TND were unpatterned silicon oxide MEMS die, but the TND had a few angstroms of diphenylsiloxane vapor-deposited onto the surface. Both samples were sealed into LCC (Leadless Ceramic Chip Carrier) packages and removed from their packages in our laboratory.

There were seventeen different types of AFM tips (Normal, Heat-treated, Attached $Si0_2$ bead, and Attached coated $Si0_2$ bead) used that ranged in size from 200 nm to 60 μm. The normal AFM tips were silicon cantilevers that had pre-existing tips on them when purchased from the manufacturer. The $Si0_2$ beads were attached to tipless silicon AFM cantilevers [18]. The attached $Si0_2$ beads that were coated had a monolayer of vapor-deposited diphenylsiloxane. The heat-treated tips (with characteristic dimensions similar to MEMS contact size) were made in a tube furnace [[24]].

The AFM was calibrated and the cantilever spring constants, AFM tip radii, and the surface roughness of the samples were measured before force curve acquisition [18, 16, 22]. Force curves were acquired between samples as well as many different AFM tips, within the topography image. For each type and size of tip, a new LCC package was opened and the unpatterened silicon oxide die were removed. First, a two-micron by two-micron topography image was acquired, from which the surface roughness of the sample was obtained. Second, force curves were obtained at sixteen different locations with each location an average of sixteen curves. The minimum in the retraction curve was the adhesive (pull-off) force.

The experimental conditions for this experiment were that relative humidity was 31 ± 10% (controlled by a common household unit), temperature was 22.2 ± 0.4°C, the AFM had closed-loop detection, and the air was filtered with a common household unit. The average sample roughness was 0.4 ± 0.5 nm. The relative uncertainty for the work of adhesion was calculated to be 15% [16, 22].

Results and discussion

For the angle of repose corrections, the maximum percent difference between the corrected and uncorrected work of adhesion was found for the largest bead (26%, radius = 56 μm) and the minimum percent difference was found for the smallest tip (4%, radius = 220 nm). The average percent of difference for all data points was 10%. The correction to the force becomes

important for beads 30 microns and larger (at 15% difference). The effects due to the angle of repose have a larger influence on larger sized tips and seem to influence the scatter in the data, not the trend.

Initially it was thought the work of adhesion was an appropriate measure for stiction and that it should have been constant as the size of the tip increases. Equation (K.1) did not match our experimental data, and the dependence of work of adhesion on radius seemed to disagree with any known contact model. The root cause for the discrepancy was the surface roughness [22]. Without correcting for the surface roughness, the observed work of adhesion on radius in Figure K-3 and Figure K-4 (Gray data points) was not expected, and it did not match continuum contact model predictions. The work of adhesion should be constant as the contact size increases (assuming the material properties do not change). Figure K-3 and Figure K-4 (Dark data points) show that the correction due to the surface roughness has a large influence on the observed behavior. Despite the data being corrected for surface roughness, the data (values) were still much higher than the expected DMT prediction, which was not surprising [22]. The number, size, and shape of the asperities within the contact area should be measured, but they were estimated to be equivalent to a single average asperity described by the RMS roughness of the AFM tip surface. However, the measurements of the surface roughness for the normal and heat-treated AFM tips were least reliable (see reference 22 for details).

Conclusion

We recommend that for stiction studies using the AFM in-fab, the spring constant of the cantilever, radius of the AFM tip, length of the cantilever, angle of repose, and the number, size, and shape of the asperities within the contact area should be calibrated (for rough surfaces). Once the pull-off forces were corrected for RMS roughness, the correct dependence for work of adhesion on radius was observed [22], but correcting for the RMS roughness increased the expected magnitudes for the work of adhesion. For more reliable works of adhesion, use normal

or heat-treated AFM tips, which have minimal roughness, but do not correct for surface roughness. The techniques developed here are ready to move into the fab, so that work of adhesion data can be compared to device performance.

Acknowledgements

EJT is grateful to Analog Devices Incorporated for his graduate fellowship. We thank the following colleagues at WPI: G. S. Iannacchione for the use of the tube furnace to create the heat-treated AFM tips, R. Garcia for the use of the evaporator to coat the backside of the heat-treated AFM tips, and G. D. J. Phillies for the use of the fume hood.

References

[1] N. A. Burnham, R. J. Colton, and H. M. Pollock, "Interpretation of force curves in force microscopy," Nanotechnology (2), 64-80 (1993).

[2] D. E. Packham, "Work of adhesion: contact angles and contact mechanics," Int. J. Adhesion and Adhesives **16**, 121-128 (1996).

[3] R. Maboudian and R. T. Howe, "Critical review: adhesion in surface micromechanical structures," J. Vac. Sci. Technol. B **1** (15), 1-20 (1997).

[4] B. Cappella and G. Dietler, "Force-distance curves by atomic force microscopy," Surf. Sci. Rep. **34**, 1-104 (1999).

[5] G. V. Dedkov, "Experimental and Theoretical Aspects of the Modern Nanotribology," physica status solidi (a) **179** (1), 3 - 75 (2000).

[6] J. A.D. Romig, M. T. Dugger, and P. J. McWhorter, "Materials issues in microelectromechanical devices: science, engineering, manufacturability and reliability.," Acta mater. **51**, 5837-5866 (2003).

[7] B. Bhushan, "Adhesion and stiction: Mechanisms, measurement techniques, and methods for reduction," J. Vac. Sci. Technol. B **6** (21), 2262-2296 (2003).

[8] Y. P. Zhao, L. S. Wang, and T. U. YU, "Mechanics of adhesion in MEMS - a review," J. Adhesion Sci. Technol. **17** (4), 519-546 (2003).

[9] R. J. Colton, "Nanoscale measurements and manipulation," Journal of Vacuum Science & Technology B: Microelectronics and Nanometer Structures **22** (4), 1609-1635 (2004).

[10] J. Drelich, G. W. Tormoen, and E. R. Beach, "Determination of solid surface tension from particle-substrate pull-off forces measured with the atomic force microscope," Journal of Colloid and Interface Science **280** (2), 484-497 (2004).

[11] J. N. Israelachvili, *Intermolecular and surface forces*, 2nd ed. (Academic, London, 1991), pp.xxi, 450 p.

[12] V. S. J. Craig, "An historical review of surface force measurment techniques," Coll. Surf. A **129-130**, 75-94 (1997).

[13] H. K. Christenson and P. M. Claesson, "Direct measurements of the force between hydrophobic surfaces in water," Advances in Colloid and Interface Science **91** (3), 391-436 (2001).

[14] G. G. Adams and M. Nosonovsky, "Contact modeling -- forces," Tribology International **33** (5-6), 431-442 (2000).

[15] R. Maboudian, "Surface processes in MEMS technology," Surface Science Reports **30** (6-8), 207-269 (1998).

[16] G. A. Matei, E. J. Thoreson, J. R. Pratt et al., "Precision and accuracy of thermal calibration for atomic-force microscopy cantilevers," (submitted 2005).

[17] B. V. Derjaguin, V. M. Muller, and Y. P. Toporov, "Effect of Contact Deformations on the Adhesion of Particles," Progress in Surface Science **45** (1-4), 131-143 (1994).

[18] E. J. Thoreson and N. A. Burnham, "Standard-deviation minimization for calibrating the radii of spheres attached to atomic force microscope cantilevers," Review of Scientific Instruments **75** (5), 1359-1362 (2004).

[19] N. A. Burnham, X. Chen, C. S. Hodges et al., "Comparison of calibration methods for atomic-force microscopy cantilevers," Nanotechnology **14** (1), 1-6 (2003).

[20] J. S. Villarrubia, in *Applied scanning probe methods* (Springer, Berlin ; New York, 2004), pp. 147-167.

[21] J. L. Hutter, "Comment on Tilt of Atomic Force Microscope Cantilevers: Effect on Spring Constant and Adhesion Measurements," Langmuir **21** (6), 2630-2632 (2005).

[22] E. J. Thoreson, J. Martin, and N. A. Burnham, "The role of a few-asperity contacts in adhesion," J. Colloid Interface Sci. (submitted 2005).

[23] G. Hüttl, V. Klemm, R. Popp et al., "Tailored colloidal AFM probes and their TEM investigation," Surf. Interface Anal. **33** (2), 50-53 (2002).

Figure Legends

Figure K-1. AFM schematic for constant-force images. As the cantilever tip is dragged across the sample surface, the laser diode beam is reflected from the back of a cantilever into a four-quadrant photodetector. The differential amplifier compares the set point (the constant amount of deflection; for contact mode) and A-B signal. The A-B signal is the difference between the top two quadrants and the bottom two quadrants, which is the angular deflection of the cantilever. The output from the differential amplifier is the error signal. The feedback loop determines what the z-scanner voltage should be (to keep the deflection constant) and the computer adjusts the high voltage amplifier. For raw force-curve acquisition, the scanner is stopped and the AFM tip is ramped into (approach) and out (retraction) of contact with the sample. The minimum in the retraction curve is the adhesive (pull-off) force.

Figure K-2. Free body diagram of the forces acting on the cantilever at pull-off. The magnitude of the torque ($\tau = \left| \vec{r} \times \vec{F} \right|$) on the cantilever was equated to the curvature of the cantilever. The subsequent deflection of the cantilever was calculated. The force on the cantilever was the deflection times the spring constant and, after simplifying, a correction was found due to the angle of repose for the cantilever.

Figure K-3. Work of adhesion versus radius for the untreated no die-attach sample (UND). Dark data points were corrected for angle of repose and surface roughness. Gray data points were corrected for effects due to the angle of repose only. ϖ = 70 ± 30 mJ/m^2, for normal and heat-treated tips only. The expected work of adhesion for

two flat plates of silicon was ϖ = 100 mJ/m^2. The error bars represent one standard deviation for the measured works of adhesion.

Figure K-4. Work of adhesion versus radius for the treated no die-attach sample (TND). Dark) The data were corrected for angle of repose and surface roughness. Gray) The data were corrected for effects due to the angle of repose only. ϖ = 45 ± 16 mJ/m^2, for normal and heat-treated tips only. The error bars represent one standard deviation for the measured works of adhesion.

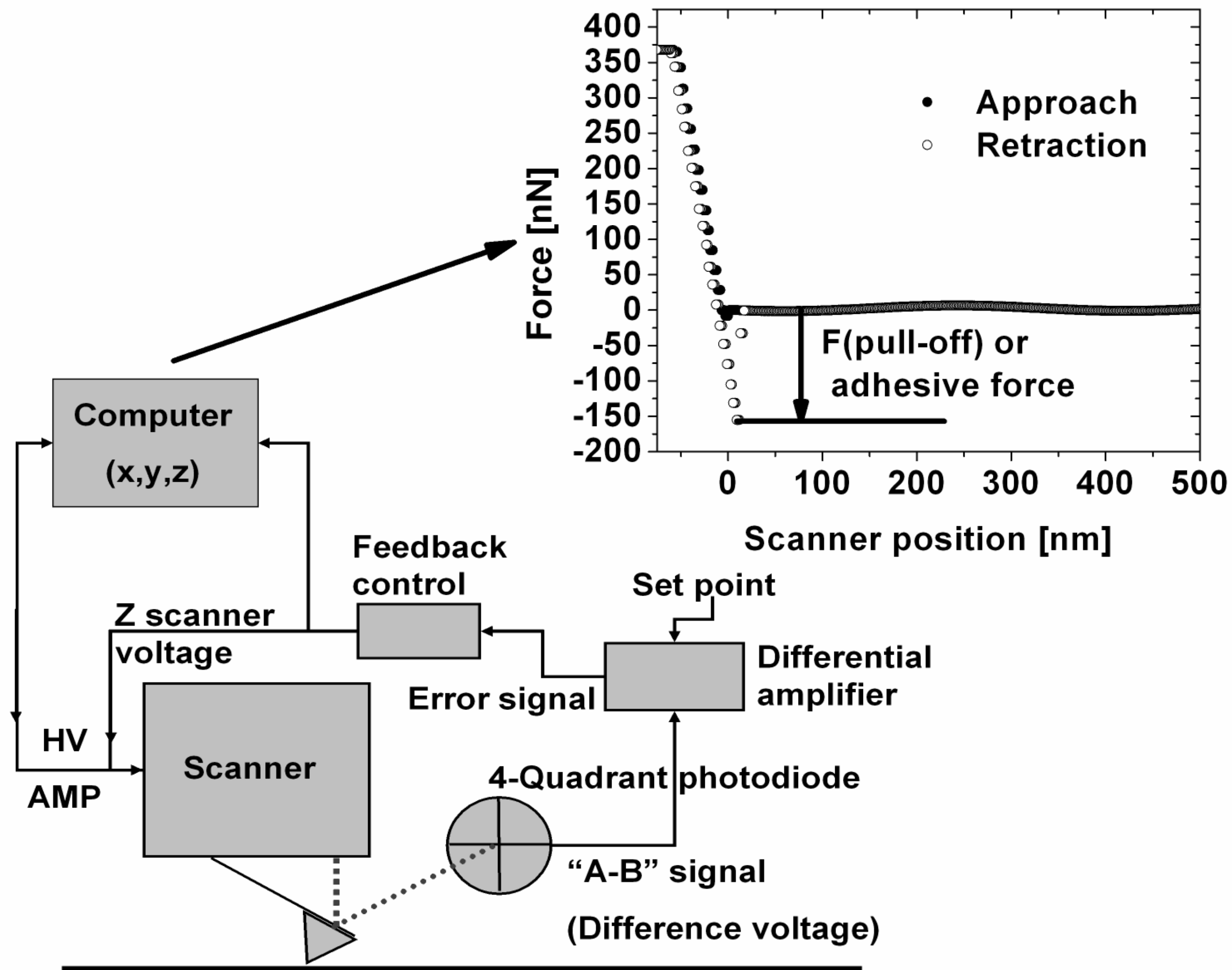

Figure K-1
Thoreson, et. al.

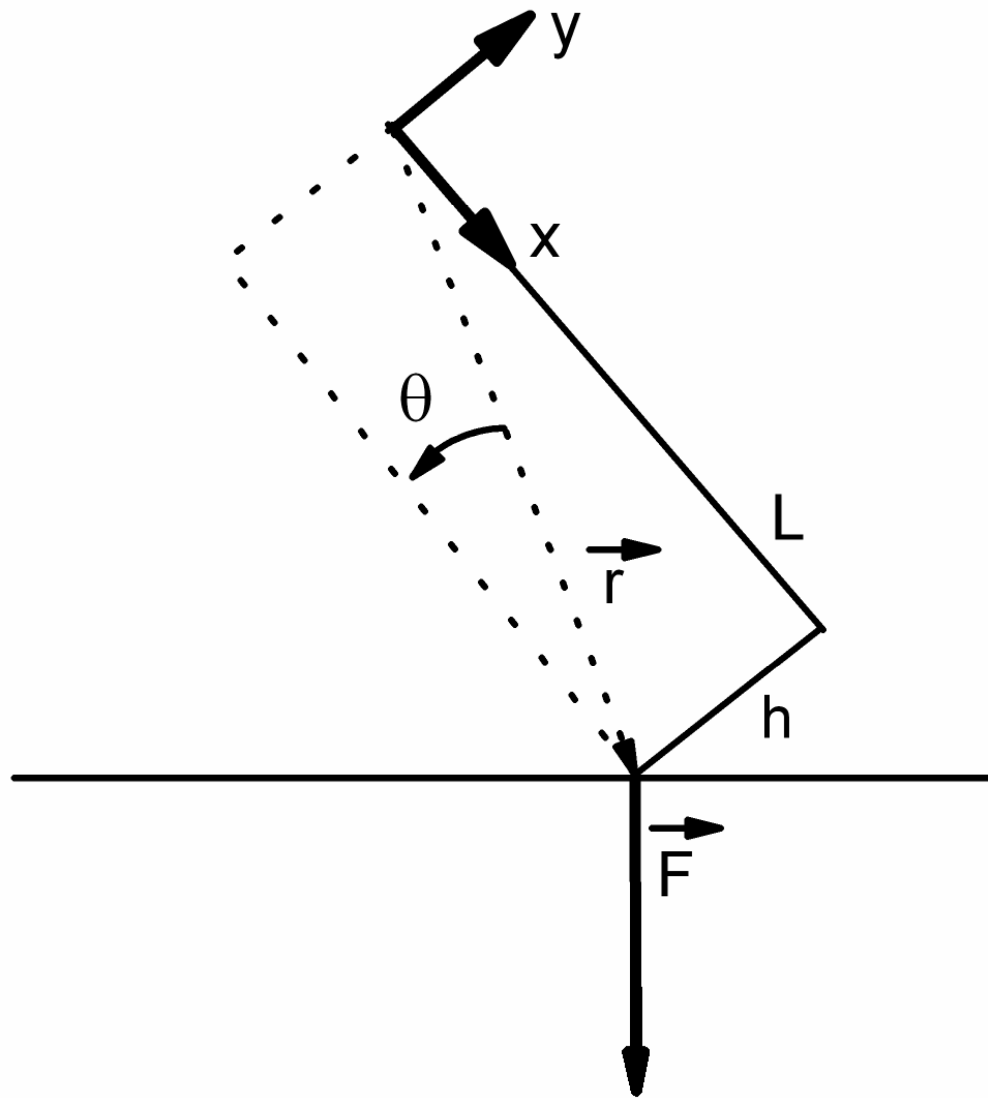

Figure K-2.
Thoreson, et. al.

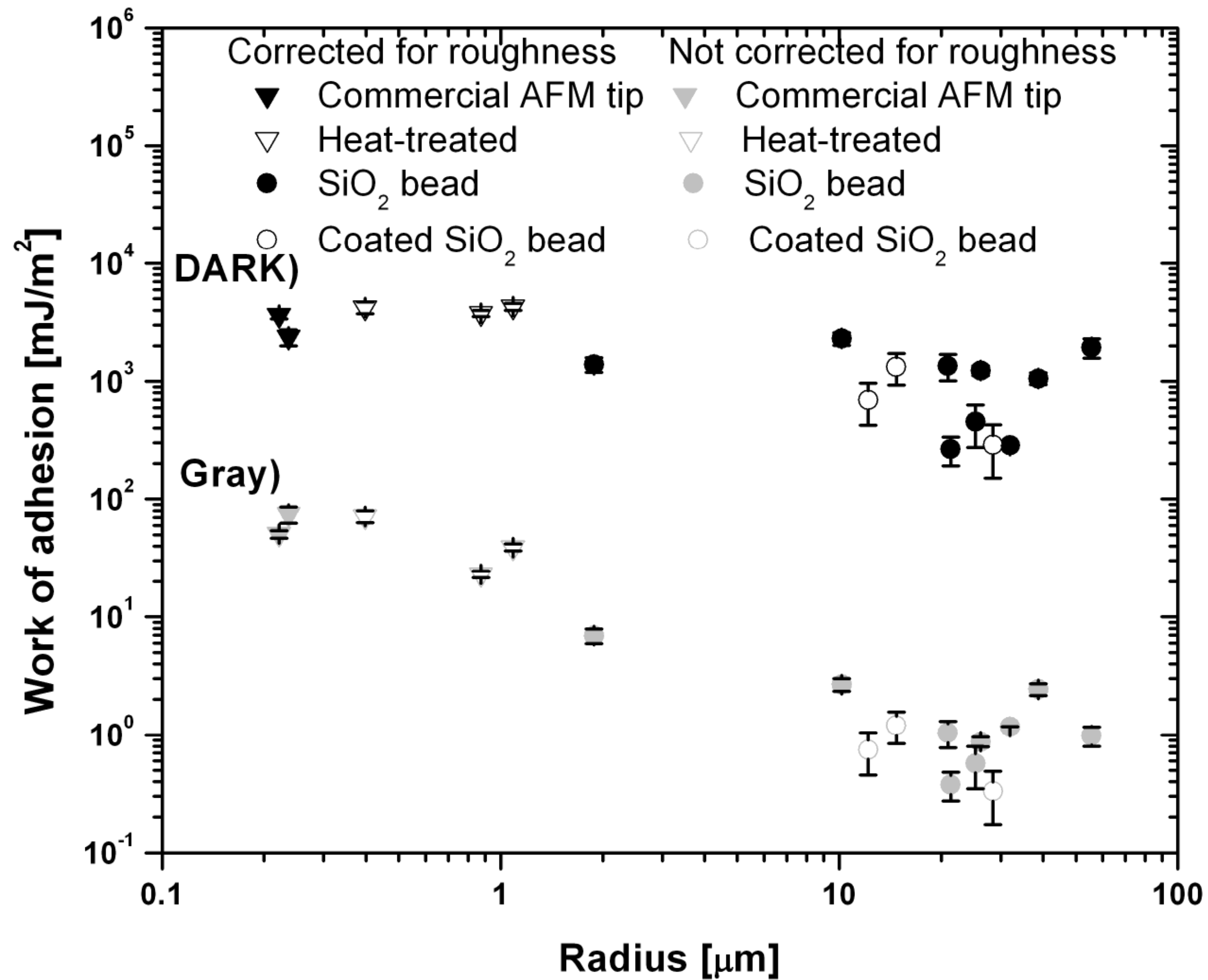

Figure K-3.
Thoreson, et. al.

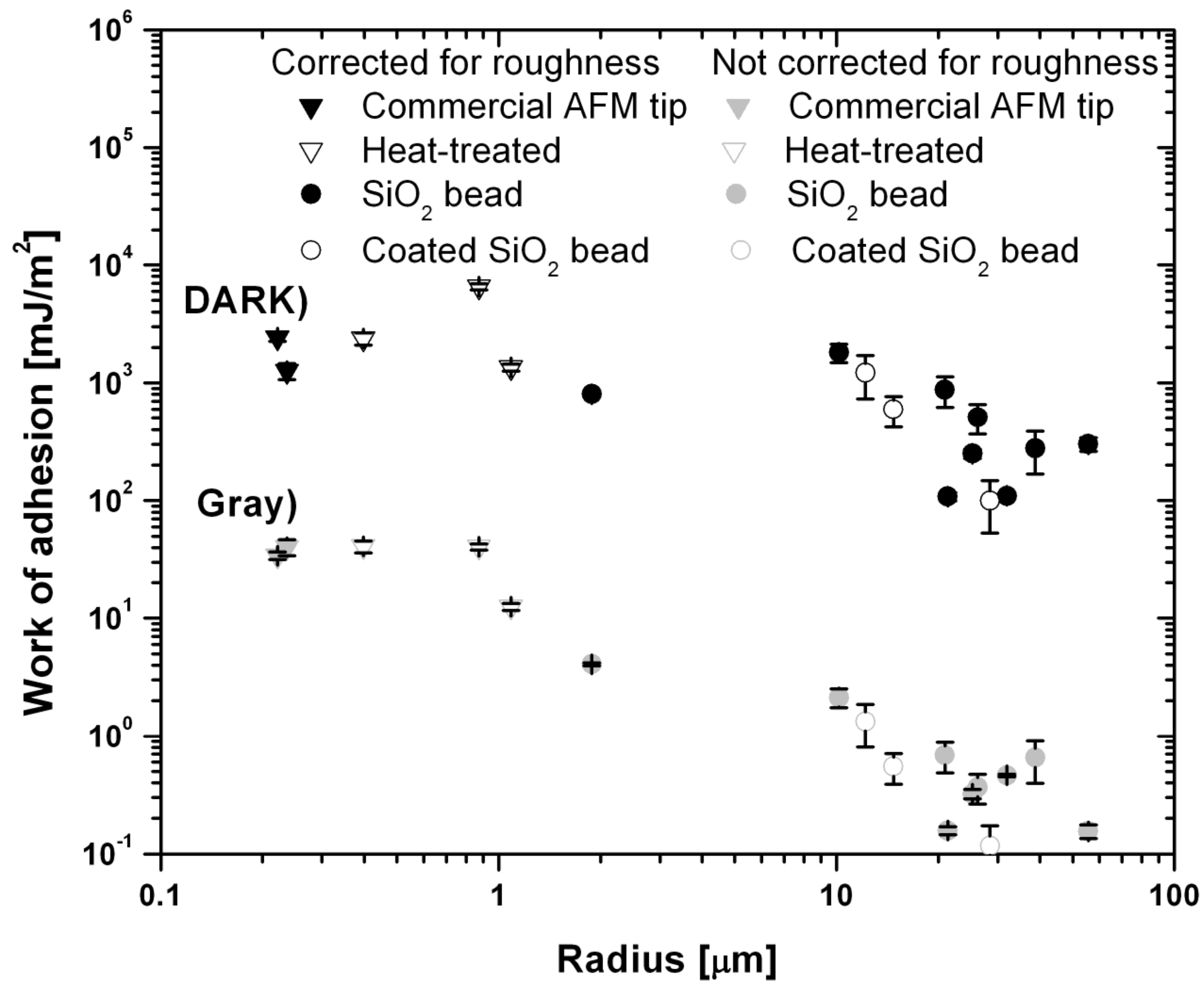

Figure K-4.
Thoreson, et. al.

[1 1] N. A. Burnham, R. J. Colton, and H. M. Pollock, "Interpretation of force curves in force microscopy," Nanotechnology (2), 64-80 (1993).

[2 2] D. E. Packham, "Work of adhesion: contact angles and contact mechanics," Int. J. Adhesion and Adhesives **16**, 121-128 (1996).

[3 3] R. Maboudian and R. T. Howe, "Critical review: adhesion in surface micromechanical structures," J. Vac. Sci. Technol. B **1** (15), 1-20 (1997).

[4 4] B. Cappella and G. Dietler, "Force-distance curves by atomic force microscopy," Surf. Sci. Rep. **34**, 1-104 (1999).

[5 5] G. V. Dedkov, "Experimental and Theoretical Aspects of the Modern Nanotribology," physica status solidi (a) **179** (1), 3 - 75 (2000).

[6 6] J. A.D. Romig, M. T. Dugger, and P. J. McWhorter, "Materials issues in microelectromechanical devices: science, engineering, manufacturability and reliability.," Acta mater. **51**, 5837-5866 (2003).

[7 7] B. Bhushan, "Adhesion and stiction: Mechanisms, measurement techniques, and methods for reduction," J. Vac. Sci. Technol. B **6** (21), 2262-2296 (2003).

[8 8] Y. P. Zhao, L. S. Wang, and T. U. YU, "Mechanics of adhesion in MEMS - a review," J. Adhesion Sci. Technol. **17** (4), 519-546 (2003).

[9 9] R. J. Colton, "Nanoscale measurements and manipulation," Journal of Vacuum Science & Technology B: Microelectronics and Nanometer Structures **22** (4), 1609-1635 (2004).

[10 10] J. Drelich, G. W. Tormoen, and E. R. Beach, "Determination of solid surface tension from particle-substrate pull-off forces measured with the atomic force microscope," Journal of Colloid and Interface Science **280** (2), 484-497 (2004).

[11 11] J. N. Israelachvili, *Intermolecular and surface forces*, 2nd ed. (Academic, London, 1991), pp.xxi, 450 p.

[12 12] V. S. J. Craig, "An historical review of surface force measurment techniques," Coll. Surf. A **129-130**, 75-94 (1997).

[13 13] H. K. Christenson and P. M. Claesson, "Direct measurements of the force between hydrophobic surfaces in water," Advances in Colloid and Interface Science **91** (3), 391-436 (2001).

[14 14] G. G. Adams and M. Nosonovsky, "Contact modeling -- forces," Tribology International **33** (5-6), 431-442 (2000).

[15 15] R. Maboudian, "Surface processes in MEMS technology," Surface Science Reports **30** (6-8), 207-269 (1998).

[16 16] G. A. Matei, E. J. Thoreson, J. R. Pratt et al., "Precision and accuracy of thermal calibration for atomic-force microscopy cantilevers," (submitted 2005).

[17 17] B. V. Derjaguin, V. M. Muller, and Y. P. Toporov, "Effect of Contact Deformations on the Adhesion of Particles," Progress in Surface Science **45** (1-4), 131-143 (1994).

[18 18] E. J. Thoreson and N. A. Burnham, "Standard-deviation minimization for calibrating the radii of spheres attached to atomic force microscope cantilevers," Review of Scientific Instruments **75** (5), 1359-1362 (2004).

[19 19] N. A. Burnham, X. Chen, C. S. Hodges et al., "Comparison of calibration methods for atomic-force microscopy cantilevers," Nanotechnology **14** (1), 1-6 (2003).

[20 20] J. S. Villarrubia, in *Applied scanning probe methods* (Springer, Berlin ; New York, 2004), pp. 147-167.

[21 21] J. L. Hutter, "Comment on Tilt of Atomic Force Microscope Cantilevers: Effect on Spring Constant and Adhesion Measurements," Langmuir **21** (6), 2630-2632 (2005).

[22 22] E. J. Thoreson, J. Martin, and N. A. Burnham, "The role of a few-asperity contacts in adhesion," J. Colloid Interface Sci. (submitted 2005).

[23 1] N. A. Burnham, R. J. Colton, and H. M. Pollock, "Interpretation of force curves in force microscopy," Nanotechnology (2), 64-80 (1993).

[24 23] G. Hüttl, V. Klemm, R. Popp et al., "Tailored colloidal AFM probes and their TEM investigation," Surf. Interface Anal. **33** (2), 50-53 (2002).

L. Bibliography

[1] J. K. Abraham, V. K. Varadan, A. K. Whitchurch et al., Proc. of SPIE, 338 (2003).
[2] Y. Arntz, J. D. Seelig, H. P. Lang et al., Nanotechnology (14), 86 (2003).
[3] R. Savic, L. Luo, A. Eisenberg et al., Science (300), 615 (2003).
[4] V. K. Varadan, Proc. SPIE (4591), 28 (2001).
[5] A. J. Harris, Proc. SPIE (4591), 39 (2001).
[6] S. A. tadigadapa and N. Najafi, J. Manu. Sci. Eng. **125**, 816 (2003).
[7] N. M. Ghoniem and K. Cho, J. Comp. Meth. Engr. Science **3**, 147 (2002).
[8] W. Merlijn van Spengen, R. Puers, and I. De Wolf, J. Micromech. Microeng. (2002) **12**, 702-713 (2002).
[9] M. L. Roukes, presented at the Technical digest of the 2000 solid-state sensor and actuator workshop, Hilton Head Isl., 2000 (unpublished).
[10] H. Guckel, J. J. Sniegowski, and T. R. Christenson, presented at the Proc. IEEE Micro Electro Mechanical Systems, Salt Lake City, Utah, 1989 (unpublished).
[11] N. A. Burnham and A. J. Kulik, in *Handbook of micro/nano tribology*, edited by B. Bhushan (CRC Press, New York, 1999), pp. 247-271.
[12] Philip Babcock Gove, *Webster's Third New International Dictionary, Unabridged*. (Merriam-Webster, 2002).
[13] Jacob N. Israelachvili, *Intermolecular and surface forces*, 2nd ed. (Academic, London, 1991), pp.xxi, 450 p.
[14] B. Bhushan, J. Vac. Sci. Technol. B **6** (21), 2262-2296 (2003).
[15] B. Cappella and G. Dietler, Surf. Sci. Rep. **34**, 1-104 (1999).
[16] E. J. Pryputniewicz, S. L. Miller, M. P. de Boer et al., presented at the Proc. Internat. Symp. on Microscale Systems, Orlando, Fl., 2000 (unpublished).
[17] T. Hsu, *MEMS & microsytems design and manufacture*. (McGraw-Hill, Boston, 2002).
[18] Jr A.D. Romig, M. T. Dugger, and P. J. McWhorter, Acta mater. **51**, 5837-5866 (2003).
[19] J. N. Israelachvili and D. Tabor, Proc. R. Soc. Lond. A. **331**, 19-38 (1972).
[20] G. Binning, C. F. Quate, and Ch. Gerber, Phys. Rev. Lett. **56**, 930–933 (1986).
[21] C. J. Coakley and D. Tabor, J. Phys. D: Appl. Phys. **11**, L77-L82 (1978).
[22] Lars-Oliver Heim, Michael Kappl, and Hans-Jürgen Butt, Langmuir **20** (7), 2760-2764 (2004).
[23] Jeffrey L. Hutter, Langmuir **21** (6), 2630-2632 (2005).
[24] Jon R. Pratt, Douglas T. Smith, David B. Newell et al., J. Mater. Res. **19** (1), 366-379 (2004).
[25] P. J. Cumpson and J. Hedley, Nanotechnology **14**, 1279-1288 (2003).
[26] G. A. Matei, E. J. Thoreson, J. R. Pratt et al., submitted Nanotechnology (2004).
[27] E. J. Thoreson and N. A. Burnham, Review of Scientific Instruments **75** (5), 1359-1362 (2004).
[28] N A Burnham, X Chen, C S Hodges et al., Nanotechnology **14** (1), 1-6 (2003).
[29] Johann Koller, Ursula Baumer, and Dietrich Mania, European Journal of archaeology **4** (3), 385-397 (1991).

[30] Chester G. Starr, *A history of the ancient world.* (Oxford University Press, Inc., New York, 1965).
[31] James E. McClellan and Harold Dorn, *Science and technology in world history.* (The John Hopkins University Press, Baltimore, 1999).
[32] Ducan Dowson, *History of tribology.* (Professional Engineering Publishing Limited, Edmunds, UK, 1998).
[33] http://users.wpi.edu/~nab/PH3117.html.
[34] J. A. Greenwood and J. B. P. Williamson, Proc. R. Soc. Lond. Ser. A. **295** (1442), 300-319 (1966).
[35] K. N. G. Fuller and D. Tabor, Proc. R. Soc. Lond. A. **345**, 327-342 (1975).
[36] Sanjit K. Das, Robert S. Schechter, and Mukul M. Sharma, Journal of Colloid and Interface Science **164** (1), 63-77 (1994).
[37] Lakkapragada Suresh and John Y. Walz, Journal of Colloid and Interface Science **183** (1), 199-213 (1996).
[38] G. M. Elimelech, X. Jia, and R. Williams, *Particle deposition & aggregation.* (Butterworth-Heinemann, Oxford, 1995), p.312.
[39] Yakov I. Rabinovich, Joshua J. Adler, Ali Ata et al., Journal of Colloid and Interface Science **232** (1), 17-24 (2000).
[40] B. N. J. Persson, F. Bucher, and B. Chiaia, Physical Review B (Condensed Matter and Materials Physics) **65** (18), 184106-184107 (2002).
[41] Binquan Luan and Mark O. Robbins, Nature **435** (7044), 929-932 (2005).
[42] E. J. Thoreson, J. Martin, and N. A. Burnham, submitted to Nature (2005).
[43] H. Hertz, J. Reine Angew. Math. **92**, 156-171 (1881).
[44] K. L. Johnson, K. Kendall, and A. D. Roberts, Proc. R. Soc. Lond. A. **324** (1558), 301-313 (1971).
[45] B. V. Derjaguin, V. M. Muller, and Y. P. Toporov, Progress in Surface Science **45** (1-4), 131-143 (1994).
[46] D. Maugis, Langmuir **11** (2), 679-682 (1995).
[47] K.L. Johnson, *Contact Mechanics*. (Cambridge University Press, 1987).
[48] D. Maugis, Journal of Colloid and Interface Science **150** (1), 243-269 (1992).
[49] D. Tabor, Journal of Colloid and Interface Science **58** (1), 2-13 (1977).
[50] E. J. Thoreson, J. Martin, and N. A. Burnham, presented at the Proceedings of the 30th International Symposium for Testing and Failure Analysis, Worcester, MA, 2004 (unpublished).
[51] N. A. Burnham, R. J. Colton, and H. M. Pollock, Nanotechnology (2), 64-80 (1993).
[52] D.E. Packham, Int. J. Adhesion and Adhesives **16**, 121-128 (1996).
[53] R. Maboudian and R. T. Howe, J. Vac. Sci. Technol. B **1** (15), 1-20 (1997).
[54] G.V. Dedkov, physica status solidi (a) **179** (1), 3 - 75 (2000).
[55] Y. P. Zhao, L. S. Wang, and T. U. YU, J. Adhesion Sci. Technol. **17** (4), 519-546 (2003).
[56] Richard J. Colton, Journal of Vacuum Science & Technology B: Microelectronics and Nanometer Structures **22** (4), 1609-1635 (2004).
[57] Jaroslaw Drelich, Garth W. Tormoen, and Elvin R. Beach, Journal of Colloid and Interface Science **280** (2), 484-497 (2004).
[58] V. S. J. Craig, Coll. Surf. A **129-130**, 75-94 (1997).

[59] Hugo K. Christenson and Per M. Claesson, Advances in Colloid and Interface Science **91** (3), 391-436 (2001).
[60] G. G. Adams and M. Nosonovsky, Tribology International **33** (5-6), 431-442 (2000).
[61] Roya Maboudian, Surface Science Reports **30** (6-8), 207-269 (1998).
[62] Niels Tas, Tonny Sonnenberg, Henri Jansen et al., Journal of Micromechanics and Microengineering (4), 385-397 (1996).
[63] M. P. de Boer and T. A. Michalske, J. Appl. Phys. **86** (2), 817-827 (1999).
[64] J. S. Villarrubia, in *Applied scanning probe methods* (Springer, Berlin ; New York, 2004), pp. 147-167.
[65] Sung-Chang Lee and Andreas A. Polycarpou, Journal of Tribology **126** (2), 334-341 (2004).
[66] Roya Maboudian and Carlo Carraro, Annual Review of Physical Chemistry **55** (1), 35-54 (2004).
[67] Grit Hüttl, Volker Klemm, Roswitha Popp et al., Surf. Interface Anal. **33** (2), 50-53 (2002).
[68] S. Dongmo, J. S. Villarrubia, S. N. Jones et al., presented at the The 1998 international conference on characterization and metrology for ULSI technology, Gaithersburg, Maryland (USA), 1998 (unpublished).
[69] E. J. Thoreson, J. Martin, and N. A. Burnham, submitted J. Colloid Interface Sci. (2005).
[70] Andrew N. Cleland, *Foundations of nanomechanics : from solid-state theory to device applications.* (Springer, Berlin ; New York, 2003), pp.xii, 436 p.
[71] H. J. Butt and M. Jaschke, Nanotechnology **6**, 1-7 (1995).
[72] F. Atamny and A. Baiker, Surface Science **3** (323), L314-L318 (1995).
[73] I. L. Singer and H. M. Pollock, *Fundamentals of friction: macroscopic and microscopic processes.* (Kluwer Academic Publishers, Boston, 1992).
[74] M. Stolz, R. Raiteri, A. U. Daniels et al., Biophysical Journal **86**, 3269-3283 (204).
[75] P. Patel-Predd, in *Nature* (2005).
[76] G. C. Brown, (Ph.D. Dissertation, WPI, WPI, 1999).
[77] C. Furlong, (Ph.D. Dissertation, WPI, WPI, 1999).

Appendix M. Related presentations and publications

M.1 Presentations

1) ADI (Analog Devices, Inc.) June 2003. Title: The effect of humidity on the work of adhesion and oxide layer growth.

2) WPI GPSO (Graduate Physics Student Organization) Talk October 2003. Title: Stiction measurements made with an atomic force microscope on test structures mounted with various die-attach materials.

3) AVS (American Vacuum Society) Poster Session Baltimore, MD November 2003. Title: Stiction measurements made with an atomic force microscope on test structures mounted with various die-attach materials.

4) Thoreson, E. J., N. A. Burnham, and J. Martin, "Quantifying the Work of Adhesion Between an AFM Cantilever Tip and MEMS Test Structures After Packaging," ISFTA, Worcester, MA, Nov. 17, 2004.

5) Thoreson, E. J., Martin, and N. A. Burnham, "Work of Adhesion Between AFM Cantilever Tips and Unpatterned Silicon Die," MRS Fall Meeting, Boston, MA, Dec. 1, 2004.

6) Thoreson, E. J., J. Martin, and N. A. Burnham, "Challenges of Using the AFM for an In-fab Stiction Monitor for MEMS devices," International Microelectronics and Packaging Symposium, Boxborough, MA, May 17, 2005.

7) Thoreson, E. J., N. A. Burnham, and J. Martin, "AFM Measurements of Stiction on MEMS Test Structures after Packaging," presented at Analog Devices, Inc., Cambridge, MA, June 2, 2004.

8) Thoreson, E. J., J. Martin, and N. A. Burnham, "Calibrated AFM Measurements to Detect Changes in Die Surfaces after Packaging," presented at Graduate Student Colloquium, WPI, Oct. 6, 2004.

9) Thoreson, E. J., J. Martin, and N. A. Burnham, "Calibrating an AFM to Measure the Works of Adhesion Between an AFM Tip and MEMS Test Structures After Packaging," presented at the National Institute of Standards and Technology, Nov. 3, 2004.

10) Thoreson, E. J., N. A. Burnham, and J. Martin, "Quantifying the Work of Adhesion Between an AFM Cantilever Tip and MEMS Test Structures After Packaging," presented at the ISFTA, Worcester, MA, Nov. 17, 2004.

M.2 Publications

1) Thoreson, E. J., and N. A. Burnham, "Standard- Deviation Minimization for Calibrating the Radii of Spheres Attached to AFM Cantilevers, " Review of Scientific Instruments 75, 1359-1362, 2004.

2) Thoreson, E. J., N. A. Burnham, and J. Martin "Quantifying the Work of Adhesion Between an AFM Cantilever Tip and MEMS Test Structures After Packaging," in proceedings of the 30th International Symposium for Testing and Failure Analysis, ASM International, Worcester, MA 216-20, 2004.

3) Thoreson, E. J., N. A. Burnham, and J. Martin "The role of few-asperity contacts in adhesion," Journal of Colloid and Interface Science, submitted, 2005.

4) Thoreson, E. J., N. A. Burnham, and J. Martin "Experimental evidence that continuum mechanics works," Nature, submitted, 2005.

5) Thoreson, E. J., N. A. Burnham, and J. Martin "Recommendations for the use of an AFM as an in-Fab stiction monitor," Journal of Microelectromechanical Systems, submitted, 2005.

M.3 Major techniques developed and new contributions summary

1) Wrote HP VEE program to read in the A-B signal as a function of time, Fourier transform the signal, build a power spectrum and average all data windows.

2) Wrote Mathcad worksheet that performs a non-linear least squares regression of the data output from the HP VEE program to calculate the spring constant of the cantilever.

3) Adapted the procedural method of the NIST loading method for our AFM.

4) Developed new technique to measure the radius of larger AFM tips.

5) Developed method to attach silicon dioxide beads to tipless AFM cantilevers.

6) Adapted technique to make larger tips using the heat-treating method.

7) Developed technique to measure the surface roughness of the AFM tips.

8) Provided insight into the physical nature of contact using continuum mechanics.

9) Developed a technique to use the AFM as an in-Fab stiction monitor.